2013

High Resolution Regional Reanalysis For Improving Representation Of Mesoscale Wind Climatology In The Chukchi-Beaufort Seas And Arctic Slope

Fuhong Liu
North Carolina Agricultural and Technical State University

High Resolution Regional Reanalysis for Improving Representation of Mesoscale Wind Climatology in the Chukchi-Beaufort Seas and Arctic Slope

Fuhong Liu

North Carolina A&T State University

A dissertation submitted to the graduate faculty

in partial fulfillment of the requirements for the degree of

DOCTOR OF PHILOSOPHY

Department: Energy and Environmental Systems

Major: Atmospheric Sciences

Major Professor: Dr. Jing Zhang

Greensboro, North Carolina

2013

School of Graduate Studies
North Carolina Agricultural and Technical State University
This is to certify the Doctoral Dissertation of

Fuhong Liu

has met the dissertation requirements of
North Carolina Agricultural and Technical State University

Greensboro, North Carolina
2013

Approved by:

Dr. Jing Zhang Major Professor	Dr. Yuh-Lang Lin Committee Member
Dr. Yevgenii Rastigejev Committee Member	Dr. Jianjun Xu Committee Member
Dr. John Roop Committee Member	Dr. Keith A. Schimmel Department Chair

Dr. Sanjiv Sarin
Dean, The Graduate School

Biographical Sketch

Fuhong Liu was born on June 6, 1985, in Huanxian, Gansu, China. He received the Bachelor of Science degree in Atmospheric Sciences from Nanjing University in 2006, a Master of Science degree in Meteorology from Nanjing University in 2009. He is a Ph.D. candidate in Energy and Environmental Systems with a concentration in Atmospheric Sciences.

Acknowledgements

I would never have been able to finish my dissertation without the guidance of my committee members, help from friends, and support from my family and wife.

Foremost, I would like to express my sincere gratitude to my advisor Dr. Jing Zhang for the continuous support of my Ph.D study and research, for her kind advice and patience, and for her excellent guidance and immense knowledge. She patiently provided the vision, encouragement and advice necessary for me to proceed through the doctoral program and complete my dissertation.

Special thanks go to my committee, Dr. Yuh-Lang Lin, Dr. John Paul Roop, Dr. Jianjun Xu, and Dr. Yevgenii Rastigejev for their valuable comments on my research and the draft of the dissertation. My sincere thanks also go to Dr. Xiangdong Zhang for his advice on my research project. Special thanks also go to Jeremy Krieger for his support and help. I would like to thank Dr. Keith Schimmel for providing support in the department.

Last, but not the least, I would like to thank my family and wife. They were always supporting me and encouraging me with their best wishes.

Funding support for this thesis research is from the Bureau of Ocean Energy Management (BOEM) of the US Department of the Interior under project M06PC00018. Computing resources were provided by the Arctic Region Supercomputing Center at the University of Alaska Fairbanks.

Table of Contents

List of Figures

List of Tables

List of Symbols and Nomenclature

ARW	Advanced Research WRF
CAI	cyclone activity index
CAM	Community Atmosphere Model
COSMIC	Constellation Observing System for Meteorology, Ionosphere, and Climate
ECMWF	European Centre for Medium-Range Weather Forecasts
ERA-40	Europe Centre for Medium-Range Weather Forecasts 40-Year Reanalysis
ERA-I	European Centre for Medium-Range Weather Forecasts Interim Reanalysis
GCM	General Circulation Model
GFS	Global Forecast System
JRA-25	Japanese 25-Year Reanalysis
LSM	land surface model
MODIS	Moderate Resolution Imaging Spectroradiometer
MPS	mountain-plains solenoidal
NARR	North America Regional Reanalysis
NCAR	National Center for Atmospheric Research
NCDC	National Climatic Data Center
NCEP	National Centers for Environmental Prediction
NMC	National Meteorological Center
NMM	Nonhydrostatic Mesoscale Model
OMA	observation-minus-analysis
OMB	observation-minus-background
PBL	planetary boundary layer

QC	quality control
QuikSCAT	Quick Scatterometer
RAWS	Remote Automated Weather Stations
RMSE	root-mean-square error
SIC	sea ice concentration
SLP	sea level pressure
T	temperature
VEC	wind vector
WRF	Weather Research and Forecast model
WRFDA	WRF Data Assimilation package

Abstract

The Weather Research and Forecasting model and its variational Data Assimilation system WRFDA has been applied to the Arctic marginal ice zone along the Chukchi-Beaufort Seas for High-resolution Atmospheric Reanalysis (CBHAR) study. To ensure the best reanalysis quality, WRFDA is optimized for the study area through a set of assimilation sensitivity experiments. The sensitivity of WRFDA to model background errors (BE), and the assimilation of various observational datasets, including both in situ observations and satellite retrievals is examined. It's found that a customized BE is necessary in order to achieve positive impacts with WRFDA. A careful selection of data to be assimilated is also essential. To improve our understanding of temporal and spatial structures of the area's surface wind, an important parameter linking dynamical processes among different components of the environmental system, the newly developed CBHAR reanalysis is used to analyze the area's mesoscale wind climatology for the data period of 1979 to 2009. In the study area, sea breezes, up/downslope winds, and mountain barrier effects are clearly captured by CHBAR. Upslope winds occur from March to September. Sea breeze begins in May, reaches its maximum in July. Mountain barrier effects are profound along the Chukotka Mountains and in the Chukchi Sea during cold seasons. The impacts of synoptic weather patterns including Arctic storm and Beaufort High on the area's mesoscale circulations are analyzed. Strong storm activity reduces the strength of sea breeze and eastward location of Beaufort High weakens the mountain barrier effect in the Chukchi Sea.

CHAPTER 1

Introduction and Literature Review

The Chukchi-Beaufort Sea region along the northern Alaskan coast (Figure 1.1) is currently undergoing significant environmental changes, including the fastest rate of decline and maximum observed interannual variance of sea ice anywhere in the Arctic (Stroeve et al. 2007; Comiso et al. 2008), as well as increased surface winds over recent decades as the sea ice retreats (Stegall and Zhang 2012). In addition to natural environmental changes, offshore energy development is ongoing along the Chukchi and Beaufort coast. Prudhoe Bay, located on Alaska's Beaufort Sea coast, is one of the largest oil fields in the world. New development opportunities also exist along the Beaufort Sea coast and in the Chukchi Sea, as evidenced by the 2008 Oil and Gas lease sale that generated more than $2.6 billion in revenue to the U.S. However, with oil extraction comes the threat of oil spills, which can have serious environmental consequences, leading to increased attention from the government, scientific community, and general public (e.g., Picou et al. 2009; Webler and Lord 2010). In particular, the coastal areas of the Chukchi and Beaufort Seas represent a vulnerable and fragile region, with an ecosystem and environment that are sensitive to human impacts (Ford and Pearce 2010; Doney et al. 2012). It is therefore of critical importance to be able to accurately predict the dispersal and movement of oil spills, and to assess the potential environmental impacts should a spill occur. Doing so requires a good understanding of surface wind, a crucial parameter for assessing and predicting oil spill transport (Reed et al. 1999).

Surface wind is a crucial parameter for assessing and predicting oil spill transport (Reed et al. 1999), driving ocean circulation modeling, and predicting sea ice drifting; it's primarily determined by the interaction of prevailing synoptic weather patterns and prominent underlying

geographic features (Schwerdtfeger 1974; Kozo 1979, 1980; Bromwich 1989). With the significant environmental changes happened in the Chukchi-Beaufort Seas region along the northern Alaska coast, surface winds also increased in recent decades (Stegall and Zhang 2012).

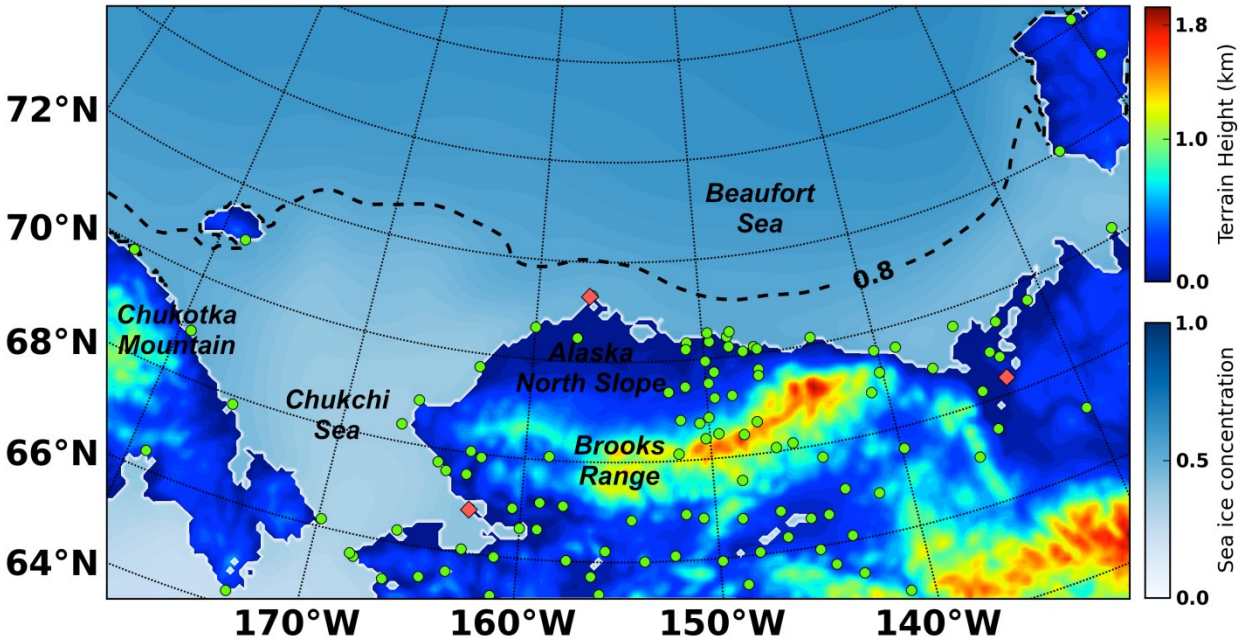

Figure 1.1. Modeling domain and distribution of in situ observation stations. Dots represent stations; diamonds are radiosonde stations. Shading over the ocean represents average sea ice concentration, with the value 0.8 highlighted by the dashed line. Shading over land represents terrain height in meters.

Accurate numerical modeling of the area's meteorology and associated surface winds poses a great challenge, due to the complexity of its predominant weather and climate systems. Significant modeling and data analysis efforts have been made with the use of the state-of-art Weather Research and Forecast (WRF) model (Skamarock et al. 2008), in order to improve the performance of modeling the Arctic atmosphere. The WRF performance was evaluated over a large pan-Arctic model domain (Cassano et al. 2011; Porter et al. 2011). The model's Arctic

land-surface processes and representations of sea ice have also been improved by the development of Polar WRF (Hines and Bromwich 2008; Bromwich et al. 2009; Hines et al. 2011). However, most of the previous studies focused on the Arctic as a whole, rather than the more regional interest of the current study. In order to better understand how the prevailing weather system interacts with local finer-scale processes, and how these in turn impact the surface wind field over the Chukchi–Beaufort Seas region, the WRF model and its data assimilation system WRFDA (Huang et al. 2009; Barker et al. 2012) have thus been utilized for the study area to generate a long-term, high-resolution regional reanalysis. The result of this effort is the 31-year Chukchi–Beaufort High-Resolution Atmospheric Reanalysis (CBHAR).

CBHAR covers the area that encompasses the Chukchi and Beaufort Seas, the entire Arctic Slope of Alaska and adjacent Brooks Range, along with portions of the Canadian Yukon and the eastern tip of Siberia (Figure 1.1), and provides high resolution reanalysis with horizontal grid spacing of 10 km at hourly frequency. Following previous study (Zhang et al. 2013) of developing a physically optimized modeling system, the WRFDA has to be optimized first to ensure reanalysis quality. In order to implement this, sensitivity experiment is a useful tool to thoroughly evaluate its performance. WRFDA is a flexible, state-of-the-art atmospheric data assimilation system and generates improved reanalysis by combining observation and background forecast through the iterative minimization of the cost function. Therefore the performance of WRFDA can be affected by factors including model's background error, the sources of observational data, and the estimated errors of observations. As thus we design a series of sensitivity experiments to thoroughly evaluate the impacts of model background errors and various observations and satellite retrievals to be assimilated.

With the generation of CBHAR reanalysis, the detailed mesoscale features of surface winds in the study area can be thoroughly investigated. Surface winds are determined by both prevailing synoptic weather pattern and prominent underlying geography (Schwerdtfeger 1974; Kozo 1979, 1980; Clark and Peltier 1984; Smith 1985; Bell and Bosart 1988; Bromwich 1989; Olsson and Harrington 2000; Parish and Cassano 2003; Lin 2007; Liu et al. 2008; Moore and Pickart 2012). In the study area, the dominant synoptic-scale weather patterns are the Beaufort High and Aleutian Low (Shulski and Wendler 2007; Overland 2009; Moore 2012), the intensity and location of which provide background flow that interacts with local geography (Lynch et al. 2004; Stegall and Zhang 2012). Prevailing synoptic circulations further interact with local geographic features, generating mesoscale circulations (e.g., Dickey 1961; Lynch et al. 2001; Moore and Pickart 2012).

The geography in the area is characterized by seasonally ice-covered ocean, along with the Brooks Range in northern Alaska and the Chukotka Mountains in eastern Siberia. The local geography affects surface winds through both thermodynamic and dynamic processes (Kozo 1979, 1980; Liu and Olsson 2008; Parish and Bromwich 1987). Sea breezes and mountain/valley breezes are caused by thermodynamic effects; and the mountain-plains solenoidal (MPS) circulation is mainly due to the interactions between orographic and thermal forcing (Orville 1964, 1968; Raymond 1972; Smith and Lin 1982; Tripoli and Cotton 1989; Banta 1990; Wolyn and McKee 1994; Lin 2007), which is usually accompanied with valley breezes. Land and ocean response to incoming solar irradiance differently, generating horizontal temperature contrast, which drives air flowing from cool area to warm area at surface and reverse at upper level (Lyons and Olsson 1972; Kozo 1979). Land/sea breezes thus characterize surface winds in coastal area during warm seasons. Similar mechanism also exists in the mountain area where

mountain slope is more easily heated than the adjacent air, which causes upslope winds during daytime. Sea breezes have been extensively studied for several decades in the tropics and midlatitudes for they are more frequent and intense; however, in higher latitudes, the studies are relatively rare due to high- and low-pressure systems making the phenomenon less noticeable (Lin 2007). Our preliminary study shows that sea breeze may still play important roles in determining the diurnal variation of surface winds in coastal region. Depending on the relative importance of buoyancy and horizontal advection, the orographic forcing plays quite different roles on surface winds, which may introduce accelerated downslope winds over the lee slope and cold-air damming (Bell and Bosart 1988; Lin 2007). During cold seasons, the air near topography surface is cooled faster than adjacent air through outgoing longwave radiation, resulting denser surface air over terrain and downslope motion of air (also referred as gravity drainage or density current) (Thorpe et al. 1980; Parish 1987, 1991, 2003; Bromwish 1989; Lin 2007). The effective dynamic process in the study area is mountain barrier effect. When an air mass with low Froude Number (U/NH) flows toward a mountain barrier, since the air mass has insufficient kinetic energy to surpass the mountain, it will be blocked when approaching. The accumulated air mass alters the distribution of pressure so that the flow is deflected to the left and finally turns to be parallel to the mountain range (Schwerdtfeger 1974; Kozo 1980).

The high resolution reanalysis CBHAR makes it possible to resolve the above mentioned mesoscale processes related to local geography, enabling systematic study of mesoscale climatology of surface winds in the area of northern Alaska coast. The features of surface winds caused by aforementioned processes are carefully studied. Instead of the in situ surface station observations and radiosonde profiles used in previous study (Kozo 1979), the high-resolution 3-dimensional CBHAR reanalysis used in this study can quantitatively represent the spatial

structures of the mesoscale processes, including the climatology of sea breezes, up/down-slope winds and mountain barrier effect: the spatial distribution, the vertical and horizontal extents, and the variability, as well as their development with time.

This study is organized as follows. The numerical model used in this study is introduced in Chapter 2. Chapter 3 details the efforts of optimizing WRFDA through a series of sensitivity experiments, as well as the thoroughly validation of the CBHAR. The mesoscale climatology and variability of topography introduced processes are analyzed in Chapter 4. The conclusions and discussions are in Chapter 5.

CHAPTER 2

Physically Optimized Weather Research and Forecast Model (WRF)

2.1 Introduction

Through the process of generating reanalysis data, the numerical model output can be combined with the observational data, improving the simulation in the model domain. Great efforts have been made to generate reanalysis dataset to represent the status of atmosphere either globally or regionally, including the Europe Centre for Medium-Range Weather Forecasts (ECMWF) 40-Year Re-analysis (ERA-40) (Uppala et al. 2005) and Interim Reanalysis (ERA-I) (Dee et al. 2011), the Japanese 25-Year Reanalysis (JRA-25) (Onogi et al. 2007), the National Centers for Environmental Prediction (NCEP)/National Center for Atmospheric Research (NCAR) Reanalysis (Kalnay et al. 1996) and North America Regional Reanalysis (NARR) (Mesinger et al. 2006). The ERA-40, ERA-I, JRA-25, and NCEP reanalysis are comprised of global data at relatively coarse resolution, making them difficult to apply in mesoscale studies. NARR is a regional reanalysis with 32-km grid spacing. However, the domain for the current study lies in the far northwest corner of the NARR domain, causing concerns regarding potential boundary effect in the data. It is thus of great necessity to generate a regional reanalysis with high resolution specifically for the study domain, which is capable of capturing the finer-scale processes of the surface wind field than was possible in previously existing products. Therefore, in order to better understand the finely detailed surface winds in the Chukchi-Beaufort Seas regions, the Weather Research and Forecast model (WRF) and its data assimilation system WRFDA have been utilized to generate a long-term, high-resolution reanalysis over the study domain.

The WRF model (version 3.2) (Skamarock et al. 2008) is our vehicle to generate the high-resolution reanalysis. The model is a widely used mesoscale model developed through a community collaboration effort and managed by the National Center for Atmospheric Research (NCAR). It is designed for a broad span of research and operational applications across scales ranging from large-eddy to global simulations. The WRF model has two distinct dynamical cores available: the Advanced Research WRF (ARW), which was developed and is maintained by NCAR, and the Nonhydrostatic Mesoscale Model (NMM), which was developed by NCEP with support from the Development Testbed Center. In this study, the ARW dynamical core was used due to the extensive testing and improvements that were previously made for its use in simulating the Arctic atmosphere (Hines and Bromwich 2008; Bromwich et al. 2009; Hines et al. 2011).

The ARW dynamics solver solves fully compressible Euler nonhydrostatic governing equations on the Arakawa C-grid staggered horizontal grid and terrain-following hydrostatic-pressure vertical coordinate. The prognostic variables include velocity components u and v in Cartesian coordinate, vertical velocity w, perturbation potential temperature, perturbation geopotential, and perturbation surface pressure of dry air. It utilizes 2nd- or 3rd-order Runge-Kutta time-split integration. The spatial discretization of 2nd- to 6th-order advection options is available in horizontal and vertical. The grid (analysis) and observation nudging capabilities are also available.

WRF has a bevy of physical parameterization options that simulate microphysical, convective, radiative, planetary boundary layer (PBL), surface layer, and land-surface processes. Different options or combination of options may produce simulation of different quality. Thus, choosing the most suitable combination of physical parameterization schemes is critical for

generating high-quality model output. The fact that parameterization schemes were developed for and primarily tested in the tropics and mid-latitudes further complicates the process of choosing suitable schemes in our study area, due to the unique modeling challenges in the Arctic. Therefore, the model configuration of physical parameterization has to be optimized before any further study over the Chukchi-Beaufort Seas and North Slope. In this study, we follow previous study of extensive model sensitivity simulations for optimizing the configuration of physical parameterizations (Zhang et al. 2013). The utilized physical parameterization configuration and improvements to model physical parameterizations are introduced in the following sections.

2.2 Optimization of Model Physical Parameterization Configuration

In order to thoroughly evaluate different physical parameterization schemes, a series of sensitivity experiments were designed and conducted (Zhang et al. 2013). The time period of experiments were selected to contain both ice-free and ice-covered ocean, as well as bare and snow-covered land, and also to include the transitional period between the two states, in order to reduce the potential bias caused by sea ice and snow cover that play significant roles in driving near-surface circulation patterns. A control experiment was first run as the benchmark for the following sensitivity experiments. The model physical parameterizations in the control simulation include Kain-Fritsch cumulus scheme (Kain 2004), WRF single-Moment 6-class microphysics scheme (Hong and Lim 2006), Community Atmosphere Model (CAM) longwave and shortwave radiation (Collins et al. 2004), Yonsei University PBL scheme (Hong et al. 2006) and Noah land-surface model (LSM) (Chen and Dudhia 2001). In total, 21 physical parameterization schemes were evaluated (Zhang et al. 2013), including 8 microphysics schemes, 3 longwave radiation schemes, 4 shortwave radiation schemes, and 6 PBL schemes. Based

around the configuration of the control experiment, one or two of the physical parameterizations were changed in each sensitivity experiment.

The results of sensitivity experiments show that the combination of physical parameterization schemes, including Morrison microphysics, RRTMG (RRTM for General Circulation Models (GCMs)) longwave and shortwave radiations (Iacono et al. 2008), Grell 3D cumulus scheme (Grell and Devenyi 2002), Mellor-Yamada-Janjic (Mellor and Yamada 1982; Janjic 2002), and Noah land-surface model, gives the optimized simulation in our study domain (Zhang et al. 2013).

2.3 Improvements to Model Physical Parameterizations

In addition to optimize the model physical parameterization configuration, more advanced physical parameterizations were also utilized, including the coupling of a thermodynamic sea ice model (Zhang and Zhang 2001) and adoption of some improvements to WRF, termed Polar WRF, made by the Polar Meteorology Group at the Ohio State University (OSU).

The coupling of thermodynamic sea ice model was designed to improve the treatment in Noah land-surface model (Zhang and Zhang 2001). The Noah land-surface model has native deficiency in sea ice processes. For example, a constant value is used as the albedo of sea ice, and sea ice has snow cover all year long. These simplifications are not consistent with reality, where sea ice albedo varies dramatically throughout the year, as well as snow over sea ice. The default scheme in Noah land-surface model could thus lead to major bias due to improper thermodynamic calculations. The coupling sea ice model was demonstrated to be able to

significantly improve the thermodynamic treatment of sea ice in the model and in turn the modeling of near-surface meteorology (Zhang et al. 2013).

Several improvements on the Noah land-surface model from Polar WRF were also utilized (Zhang et al. 2013; Hines and Bromwich 2008; Bromwich et al. 2009; Hines et al. 2011). Polar WRF represents a package of code change based on WRF, intended to improve the overall performance of WRF for the polar regions. The package is available to the public since late 2009. The utilized improvements from Polar WRF include incorporating variable sea ice thickness data rather than the constant 3-m thickness value set in by default in the model, and setting the bottom temperature of sea ice to -1.8°C instead of the default -2.0°C. These modifications were tested and confirmed to be capable of improving the simulation of heat transfer between the atmosphere and the liquid ocean beneath the ice, which in turn improves the simulation of both surface air temperature and sea ice skin temperature.

2.4 Summary

An improved WRF model (Zhang et al. 2013) was used in this study. Different model physical parameterization schemes and their combinations were extensively evaluated in our study domain covering the Chukchi-Beaufort Seas and North Slope. The optimized physical configuration was demonstrated to be able to provide better simulation than the others. The utilized parameterization schemes include Morrison microphysics, RRTMG longwave and shortwave radiations, Grell 3D cumulus scheme, Mellor-Yamada-Janjic, and Noah land-surface model. In addition, a coupling thermodynamic sea ice model and improvements from Polar WRF were also utilized to improve the treatment of sea ice in the Noah land-surface model.

CHAPTER 3

Generation of the Chukchi-Beaufort High-Resolution Atmospheric Reanalysis (CBHAR) via the WRFDA Data Assimilation System

3.1 Introduction

The Chukchi-Beaufort Sea region along the northern Alaskan coast is currently undergoing significant environmental changes, including the fastest rate of decline and maximum observed interannual variance of sea ice anywhere in the Arctic (Stroeve et al. 2007; Comiso et al. 2008), as well as increased 10-m wind speeds over recent decades as the sea ice retreats (Stegall and Zhang 2012). In addition, the potential for further oil industry development exists along the Chukchi and Beaufort coast. With oil extraction comes the threat of oil spills, which can have serious environmental consequences, leading to increased attention from the government, scientific community, and general public (e.g., Picou et al. 2009; Webler and Lord 2010). In particular, the coastal areas of the Chukchi and Beaufort Seas represent a vulnerable and fragile region, with an ecosystem and environment that are sensitive to human impacts (Ford and Pearce 2010; Doney et al. 2012). It is therefore of critical importance to be able to accurately predict the dispersal and movement of oil spills and to assess the potential environmental impacts should a spill occur. Doing so requires a good understanding of surface wind, a crucial parameter for assessing and predicting oil spill transport (Reed et al. 1999).

Surface wind is primarily determined by the interaction of prevailing synoptic weather patterns with prominent underlying geographic features (e.g., Schwerdtfeger 1974; Kozo 1979, 1980; Bromwich 1989; Olsson and Harrington 2000; Parish and Cassano 2003; Liu et al. 2008; Moore and Pickart 2012). In the Chukchi-Beaufort Sea region, the Beaufort High and Aleutian Low are the two dominant synoptic-scale weather patterns that most directly influence surface

winds (Shulski and Wendler 2007; Overland 2009; Moore 2012); when the intensity and location of these systems change, the surface winds over the study area vary in response (Lynch et al. 2004; Stegall and Zhang 2012). Prevailing synoptic circulations further interact with local geographic features, generating mesoscale circulations (e.g., Dickey 1961; Lynch et al. 2001; Moore and Pickart 2012). The geography in the study area is characterized by seasonally ice-covered ocean, along with the Brooks Range in northern Alaska and the Chukotka Mountains in eastern Siberia. During the winter months, the surface can become extremely cold and temperature inversions are very common in the area. Each of these local geographic features interacts with prevailing synoptic weather systems to generate characteristic mesoscale atmospheric circulations that correspondingly influence the associated surface winds in the region (Schwerdtfeger 1974; Kozo 1980).

Due to the complexity of the weather and climate systems in the study area, accurate numerical modeling is challenging. To improve the performance in modeling the Arctic atmosphere, significant efforts have been made using the state-of-the-art regional Weather Research and Forecasting (WRF) model. Among these were the thorough evaluation of WRF performance over a large pan-Arctic model domain (Cassano et al. 2011; Porter et al. 2011) and the development of Polar WRF (Bromwich et al. 2009; Hines et al. 2011), in which the model's Arctic land-surface processes and representation of sea ice were improved. The application of Polar WRF for the Arctic System Reanalysis (Bromwich et al. 2010; Wilson et al. 2011, 2012) indicated that the surface temperature produced by Polar WRF agreed well spatially with the forcing global reanalysis, while including additional spatial details, particularly in regions of higher elevation. Wilson et al. (2011) suggested that the surface wind speed could be improved further if higher spatial resolution is used, smooth terrain of coarse grid spacing resulting in

overestimated 10-m wind speed. This factor encourages us to choose relatively high-resolution grid spacing for this study. In addition, mesoscale modeling of the Alaskan interior with WRF by Mölders (2008) suggested that biases can exist in such simulations due to inaccurate initial and boundary conditions. With the development of various satellite retrievals, as well as improvements in the in situ observational network, the accuracy of model initial conditions and forecast performance can be improved through the application of data assimilation techniques. Various reanalysis projects are taking advantage of such improved model initial conditions to generate high quality data. We adopted the same approach and are applying the WRF model (version 3.2.1) and its variational data assimilation system WRFDA (version 3.2.1) to the study area to generate the long-term Chukchi-Beaufort High-Resolution Atmospheric Reanalysis (CBHAR). The CBHAR reanalysis will provide a unique opportunity for better understanding how the changing climate interacts with local fine-scale processes, and how these in turn impact the mesoscale meteorology of the surface wind field along the Chukchi-Beaufort Sea region. To achieve this goal, an optimized WRFDA will be configured for the study area through a set of assimilation sensitivity experiments, in which the sensitivity of WRFDA to model background errors (BE) and the assimilation of various observational datasets will be analyzed. With this customized data assimilation system in place, the high-resolution atmospheric reanalysis CBHAR can be generated, toward the goal of more accurately capturing the fine-scale processes of the region's surface wind field than has been possible in existing reanalysis products.

The remainder of this paper is structured as follows: Section 2 provides a brief description of the model and data used in this study; the efforts toward optimizing the configuration of the WRFDA assimilation system, through generating model domain- and configuration-dependent model BE and selectively assimilating various in situ and satellite

observations, are introduced in Section 3; a one-year experimental reanalysis produced with the optimized assimilation configuration is presented in Section 4; and a summary of this study is given in Section 5.

3.2 Model and Data for Constructing CBHAR

The Advanced Research WRF (ARW) model (Skamarock et al. 2008) is our vehicle to generate the high-resolution reanalysis CBHAR. ARW is a community mesoscale model developed through a community collaboration effort and managed by the National Center for Atmospheric Research (NCAR). ARW has various dynamical and physical options and includes its own data assimilation system WRFDA (Huang et al. 2009; Barker et al. 2012). WRFDA has been designed to be a flexible atmospheric data assimilation system, which includes options for both three-dimensional (3DVAR) and four-dimensional (4DVAR) variational data assimilation. In this study, the 3DVAR assimilation technique has been adopted to improve the model's initial conditions and generate the final high-resolution analysis. 4DVAR was not considered due to its relatively high computational cost (Barker et al. 2004, 2012), making it impractical for our ultimate goal of producing a long-term (31 year) reanalysis. In WRFDA, the analysis field is generated by merging observations and background forecasts through iterative minimization of the cost function (Barker et al. 2004, 2012). The background forecasts in this study are generated by the WRF simulations, and the observations are quality controlled before being assimilated by WRFDA. The modeling domain for this study (Figure 1.1) is configured to encompass the Chukchi and Beaufort Seas, the entire Arctic Slope of Alaska and adjacent Brooks Range, along with portions of the Canadian Yukon and the eastern tip of Siberia. The domain has a grid spacing of 10 km with 49 vertical levels and a model top of 25 hPa. A summary of the model configuration parameters and physical schemes used is given in Table 3.1.

Table 3.1

WRF model configuration

	Options	Configuration
Physics	Microphysics	Morrison 2-moment (Morrison et al. 2009)
	Longwave radiation	Rapid Radiative Transfer Model for GCMs (RRTMG) (Iacono et al. 2008)
	Shortwave radiation	RRTMG (Iacono et al. 2008)
	Planetary boundary layer	Mellor-Yamada-Janjic (Eta) (Hong et al. 2006)
	Surface layer	Monin-Obukhov (Janjic Eta) (Janjic 1994, 1996, 2002)
	Land-surface model	Noah land-surface model (Chen and Dudhia 2001)
	Cumulus	Kain-Fritsch (Kain 2004)
Grid	Horizontal grid spacing	10 km
	Vertical levels	49 levels with top at 25 hPa
WRFDA	Surface assimilation option	2

The European Centre for Medium-Range Weather Forecasts (ECMWF) Interim Reanalysis (ERA-I) (Dee et al. 2011) is used to provide atmospheric forcing and initial conditions for soil moisture and temperature, as well as sea surface temperature. The lateral and lower boundary conditions are also provided by ERA-I. The daily NASA Bootstrap SIC (Comiso 1999, 2012) as acquired from the National Snow and Ice Data Center is used. The ERA-I reanalysis has been widely used in Arctic WRF simulations (Bromwich et al. 2013), and has also proved to help WRF generate more accurate simulations in our study domain (Zhang et al. 2013).

The in situ observational data used for assimilation and model verification in this study include surface observations from 122 stations distributed throughout the model domain, along with three radiosonde stations, as indicated in Figure 1.1. These in situ observations have been collected from different data sources including the National Climatic Data Center (NCDC), the interagency network of Remote Automated Weather Stations (RAWS), and others. All of these collected data have been quality controlled with three separate quality-control (QC) procedures, which check for observations that fall outside of a normal range (threshold test), consecutive values that differ too greatly (step change test), and instances of excessively high or low variability (persistence test) (You et al. 2011). Criteria for the quality control were defined based on each station's climatology. The satellite retrievals assimilated by WRFDA include Quick Scatterometer (QuikSCAT) ocean-surface winds, as well as temperature and moisture profiles from both the Moderate Resolution Imaging Spectroradiometer (MODIS) and Constellation Observing System for Meteorology, Ionosphere, and Climate (COSMIC) platforms.

The in situ surface observations contain hourly 2-meter temperature and humidity, 10-meter wind, and pressure. The radiosonde profiles include 12-hourly temperature, vapor pressure, relative humidity, and wind at vertical levels extending from the surface up to about 10 hPa. The QuikSCAT surface winds are available over open water at a resolution of 12.5 km and cover the period from 1999 to 2009 (Long and Mendel 1990). The MODIS-retrieved moisture and temperature profiles (King et al. 2003) include 20 vertical levels from 1000 to 5 hPa at a horizontal resolution of 5 km, and are available since 2000. The COSMIC retrievals (Anthes et al 2008), available from 2006, include temperature and moisture profiles, usually thinned at 26 vertical levels from 1000 to 10 hPa.

3.3 Optimization of Data Assimilation Configuration within WRFDA

Though data assimilation is a useful technique for constraining the model solution and reducing model forecast errors, assimilating an extra dataset into the model does not necessarily improve the quality of the subsequent simulation for all variables due to accuracy issues in both the assimilated data and error information (Barker et al. 2004, 2012). The variational assimilation system WRFDA determines the optimal analysis through the use of information that includes model background error (BE) and observation data error. The assimilation scheme within WRFDA then combines the dynamic model results with the observations using weights inversely related to each of their errors (Barker et al. 2004, 2012). Each observation data type is characterized by its own error distribution, dependent on the accuracy of the individual observation system, but model errors can be affected by the choice of model domain and configuration. In order to best optimize the WRFDA assimilation system for the production of CBHAR, we conduct two sets of sensitivity experiments as described in the following two sections: Section 3.1 describes tests for the evaluation of model BE sensitivity, and Section 3.2 details those for evaluating the potential observation data types to be assimilated.

The selected simulation periods include January 2009 for representing winter conditions and July 2009 for summer conditions. The oceanic portion of the domain experiences high variability throughout the year in its sea-ice coverage and surface temperature, and the land similarly varies in its snow cover and thermal profile. This high level of variability provides a good opportunity for investigating the performance of WRFDA by examining the two extreme months of January and July.

In all of the sensitivity simulations, the model is re-initialized every 2 days, still using ERA-I forcing data to provide initial, lateral and lower boundary conditions, and run for 2 days

and 6 hours (Figure 3.1). The reason to conduct re-initialization is because the forecast errors in a continuously run keep increasing with time even the data is assimilated every 6 hours. Our experiments show that in the study domain, when the model is continuously run with data assimilated every 6 hours, the forecast errors increase to be equivalent to the non-assimilation run after about two days. The two-day re-initialization is thus chose. The available observational data are assimilated every 6 hours (including at the initial hour). Only data within ±1.5 hours of the assimilation hour are used. The results from the first 6 hours of each run are used as model spin up and removed from consideration, with the remaining 2-day periods pieced together to form a continuous time series. In addition to the assimilation runs, a control simulation (CTRL), in which no data is assimilated through WRFDA but which is otherwise identical to the assimilation runs, including the stop-restart cycle every 6 hours, is also conducted for the purposes of comparing and evaluating the sensitivity results.

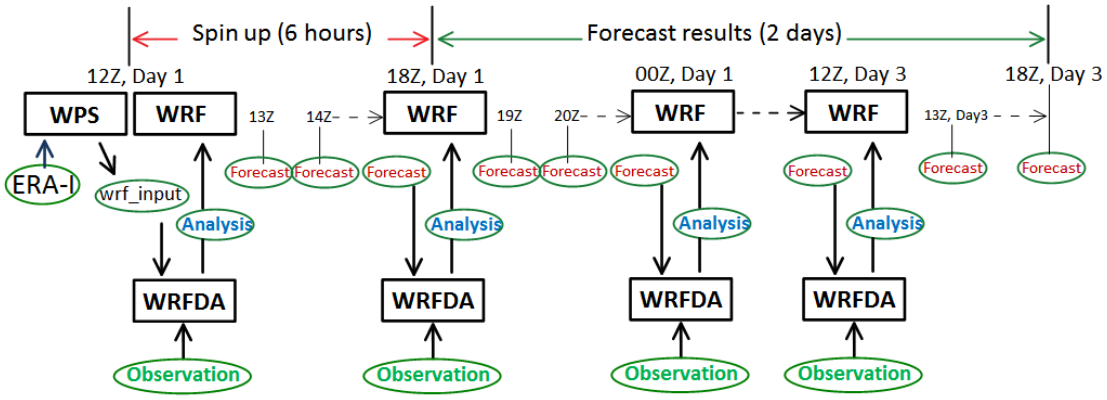

Figure 3.1. Cycling scheme for the assimilation experiments. A cold-start run is initialized from ERA-Interim at 1200 UTC and run for two days and six hours, with observational data assimilated every six hours.

The simulation results are evaluated by analyzing the root-mean-square errors (RMSE) as verified against non-assimilated observations and satellite retrievals, including the in situ surface observations, QuikSCAT winds, and radiosonde profiles. To maintain independence between observations used for assimilation and verification, only model results at the forecast (non-assimilation) hours of each assimilation cycle (Figure 3.1) are included in the RMSE calculation. For verification against radiosondes, however, due to the fact that only two profiles are normally produced each day, both at assimilation times, the model results one hour before the sounding times are compared with the observations. Verified variables include sea-level pressure (SLP), 2-meter temperature (T), 10-meter wind vector (VEC), and upper-level temperature and wind vector. The RMSE of VEC is defined as the sum of RMSEs of zonal (U) and meridional (V) components, so that it can represent the errors of both wind speed and direction. For each simulation experiment, the RMSEs are first calculated at each observation station, and then averaged among all the stations within the model domain. The Student's *t*-test is used to assess the statistical significance of the RMSE differences between the sensitivity and CTRL simulations. An improved sensitivity simulation is defined to be one with reduced RMSE, and with the difference from the CTRL simulation statistically significant at the 95% level.

3.3.1 Analysis of WRFDA sensitivity to model background error. WRFDA offers the option to use either built-in global model BE (BE-GFS) or user-customized model BE in its data assimilation process. The built-in BE is generated from Global Forecast System (GFS) forecasts, produced by NCAR with a horizontal grid spacing of about 80 km, and can be used for any domain due to its global coverage (Barker et al. 2004). The customized BE is calculated following the National Meteorological Center (NMC) method (Parrish and Derber 1992), in which the differences between 12- and 24-hour model forecasts valid at the same time are first

calculated, with the model BE estimated after averaging all forecast differences over a period of time and the error covariances calculated. In this study, the 12- and 24-hour forecasts for the entire year of 2009 are first generated with the model configuration listed in Table 3.1. The differences between the 12- and 24-hour forecasts are then averaged, both over the entire year and for each month individually, in order to produce both a yearly-averaged BE (BE-1yr) and monthly-averaged BE (BE-Jan, BE-Jul), respectively.

Table 3.2

Experiments for evaluating model Background Error (BE) ('BE' field describes the BE used in each experiment)

Experiments	**Data assimilated**	**BE**	**Simulation Period**
CTRL	**No data assimilated through WRFDA**		January and July 2009
BE-GFS	In situ surface observations	Built-in global BE	January and July 2009
BE-1yr	In situ surface observations	Customized BE from 1-year (2009) simulation	January and July 2009
BE-Jul	In situ surface observations	Customized BE from 1-month (July 2009) simulation	July 2009
BE-Jan	In situ surface observations	Customized BE from 1-month (January 2009) simulation	January 2009

Table 3.3

Verification of model BE experiments against different observational sources for temperature (T), sea level pressure (SLP), and wind vector (VEC) in January and July 2009 (RMSEs are calculated against non-assimilated surface observations and QuikSCAT. When verified against surface observations, coastal and inland stations are verified separately. RMSEs calculated against radiosondes are averaged over all sounding levels. Improved or degraded RMSEs (compard to CTRL) that are statistically significant at the 95% level are shown in bold)

		RMSE								
Exp.		Surface observation						Radiosonde		QuikSCAT
		T		SLP		VEC		T	VEC	VEC
		Coast	Inland	Coast	Inland	Coast	Inland			
Jul	CTRL	2.69	3.77	1.15	1.69	3.18	3.28	1.08	2.93	3.42
	BE-GFS	**2.75**	**4.34**	**1.27**	**1.96**	**3.34**	**3.56**	**1.97**	**4.26**	**3.74**
	BE-1yr	**2.44**	**3.79**	**1.05**	1.68	**3.01**	**3.13**	1.08	2.89	**3.32**
	BE-Jul	**2.44**	**3.77**	**1.02**	**1.65**	**3.00**	**3.10**	1.09	2.94	**3.32**
Jan	CTRL	5.64	6.15	1.54	4.54	3.80	3.93	2.03	4.32	No QuikSCAT data in ice-covered season
	BE-GFS	**6.92**	**7.54**	1.69	5.00	**4.22**	**4.10**	**4.18**	**6.34**	
	BE-1yr	**5.94**	**6.03**	**1.33**	4.54	**3.66**	**3.79**	2.09	4.30	
	BE-Jan	**6.10**	**6.04**	**1.35**	4.60	**3.67**	**3.78**	2.13	4.33	

A total of five control and sensitivity simulations (Table 3.2) are conducted in order to evaluate the sensitivity of WRFDA to model BE in the assimilation of in situ surface observations. In addition to the built-in model BE-GFS, customized model BEs, including the yearly-averaged BE-1yr and monthly-averaged BE for January (BE-Jan) and July (BE-Jul), are independently tested in the sensitivity experiments BE-GFS, BE-1yr, BE-Jan, and BE-Jul. The default values of tuning parameters for variance and length scale are used in all experiments in order to avoid any inconsistent comparison. The simulation periods include both January and July 2009 for most simulation experiments, with the exceptions that BE-Jan is only used for January 2009 and BE-Jul only for July 2009.

The impacts of the model BEs on assimilation performance are analyzed with the RMSE of the model outputs relative to surface observations, radiosondes, QuikSCAT winds (Table 3.3). When verifying against surface observations, the stations are divided into two groups—coastal and inland stations—in order to distinguish the performance of the assimilation between complex terrain and flat, coastal areas. Surface stations located within 30 km of the shoreline are designated as coastal stations, with those farther from shore designated as inland stations. Using this criterion, there are a total of 56 coastal stations and 66 inland stations available within the model domain.

Comparisons of RMSEs among the control and sensitivity simulations as verified against all three types of observations for both the January and July cases (Table 3.3) demonstrate that the built-in model BE (BE-GFS) significantly degrades the model performance in our study area, generating much greater errors than the control simulation in which no data is assimilated through WRFDA. This comparison suggests that in order to achieve positive impacts from data assimilation via WRFDA, usage of the built-in model BE should be avoided. On the other hand,

the customized model BEs, both yearly- and monthly-averaged, generally serve to enhance the model performance, reducing the errors for most of the examined variables. A close look at the comparison further demonstrates that the improvements in SLP and the 10-m wind field by the customized BEs are seen continually throughout both the cold and warm months. For temperature, however, a slight negative effect is present in the January case, even with the use of customized BEs. This indicates that accurately modeling the strong surface temperature inversions characteristic of Arctic winter remains a challenge for the WRF model. Accordingly, the estimated model BEs might not fully represent the actual model performance in such conditions, resulting in a degradation of the data assimilation performance. The performance of the monthly- and yearly-averaged BEs is similar, indicating that including seasonal variability in the customized BEs is insignificant in this study.

Assimilation of in situ surface observations generates differing impacts in coastal and inland areas. In the BE-GFS experiment, simulation of the 2-m temperature is degraded by 2% (23%) in the coastal areas, and by 15% (23%) inland when compared to the CTRL simulation in July (January), while the RMSEs for the 10-m wind vector are 5% (11%) and 9% (4%) larger in July (January) for the coastal and inland stations, respectively (Table 3.3). This indicates that the built-in model BE generated by the coarse-resolution GFS simulation (~80 km) is more problematic during winter and over complex terrain. Greater overall improvements can be achieved in the coastal region relative to inland areas through the use of customized model BEs. During summer, 2-m temperature and SLP in the coastal areas are improved by 9% and 9–11%, respectively, while the impacts are very small inland. For the 10-m wind field, improvements are similar for the coastal and inland areas, with 5% (4%) improvement at the coastal stations and 5% (4%) inland during July (January). Similar to the difficulty that the model has in simulating

inversions, the fact that the inland area is characterized by complex topography, presents a challenge for WRF in accurately capturing many terrain-induced fine-scale details. Because model BE does not represent the actual model error relative to observations, but rather the average difference between one forecast time and another, BE can be underestimated in situations where the model performs inherently poorly. Thus, the performance of the assimilation can be hampered due to a less accurate estimation of model BE.

To further investigate the reason why assimilation using BE-GFS degrades the results relative to CTRL, the observation-minus-analysis (OMA) and observation-minus-background (OMB) at each assimilation time are compared. It is noted that benefits are always achieved in the analysis relative to the background no matter which model BE is used. However, the forecast errors tend to grow faster when using BE-GFS. Therefore, during the free 5 forecast hours (Figure 3.1), the errors are gradually accumulated, even though assimilation serves to reduce them every 6 hours. This demonstrates that model BE not only determines the immediate assimilation effects, but also impacts the forecast evolution.

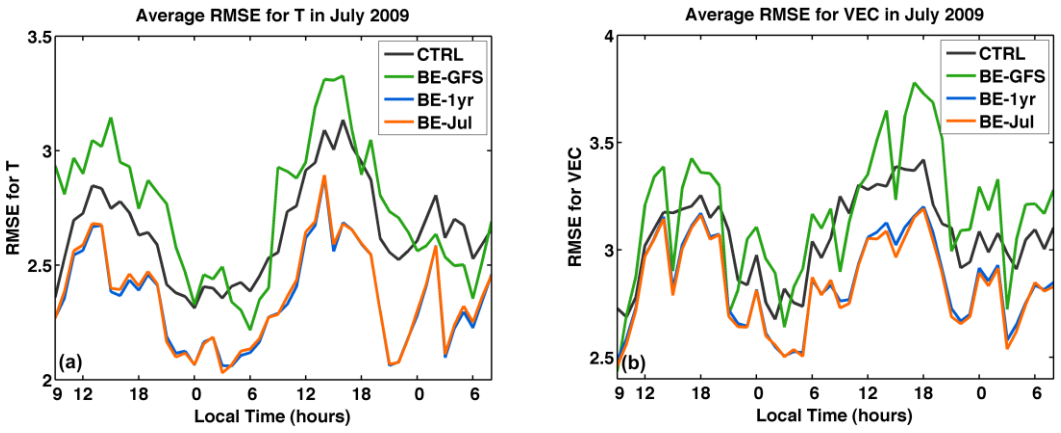

Figure 3.2. Averaged RMSE of (a) temperature and (b) surface wind vector for BE experiments in July 2009. RMSEs are averaged over 56 coastal stations and displayed over the average 48-hour cold-start model cycle.

Since the coastal area receives a greater benefit from assimilation, the averaged 48-hour simulation cycle of the temperature and wind vector RMSEs, as averaged over 56 coastal stations, is compared for the month of July 2009 over all simulation tests (Figure 3.2). During the averaged simulation cycle, both monthly- and yearly-averaged customized model BEs perform very similarly in improving the model results throughout the entire diurnal cycle. On the other hand, the built-in model BE (BE-GFS) degrades the model results, particularly for 2-m temperature during the day.

The spatial distribution of the assimilation impacts can be further revealed by the analysis increments generated by WRFDA. The increments are calculated by subtracting the model background fields from the resultant analysis fields. Comparisons of temperature and wind field (divided into zonal (U) and meridional (V) components) increments at the lowest model level between the sensitivity experiments BE-GFS and BE-1yr demonstrate that the increments generated using customized BE differ from those using the built-in BE in many respects, such as spatial scale and distribution, as well as the magnitudes of adjustment (Figure 3.3). The increments produced by BE-GFS display a larger-scale distribution, as exemplified by the positive temperature increment centered on central Alaska that extends northeastward all the way to Banks Island and westward to the Chukotka Mountains (Figure 3.3). In contrast, the increments in BE-1yr are essentially constrained within the land areas of the domain and characterized by several smaller mesoscale centers. Model BE can determine how the assimilated information is spread out. BE-GFS, generated from the GFS model at a resolution of 80 km, has a larger spatial impact, which can propagate the effects of assimilated observations over a wider area. The increments in the customized BE experiment seem to show a reasonable range of assimilation effects. The magnitudes of adjustment in the experiment BE-GFS are also

generally greater relative to those in BE-1yr. The maximum temperature increase is about 2.8°C in BE-GFS, while only about 1.8°C in BE-1yr. Temperature increases are greater than 1°C over roughly half of the model domain in BE-GFS, while the same area sees increases of only 0.4°C or greater in BE-1yr. Similarly, the wind field adjustments are as high as 0.9 m s^{-1} in BE-GFS, but only 0.4 m s^{-1} in BE-1yr. Since the data assimilated here come primarily from land areas, it's expected that the most significant increments will occur over land as well. However, significant increments in the experiment BE-GFS also occur over ocean areas, where few observational data are available. This further implies that the built-in model BE cannot accurately represent the true model performance within the study area and will likely degrade the performance of assimilation if used.

From the comparison of RMSEs calculated against radiosondes (Table 3.3), we see that even though only in situ surface observations were assimilated by the WRFDA system, the upper atmosphere can also be impacted nontrivially when the built-in model BE is used; the impacts from customized model BEs are very small, however. The built-in BE increases the RMSEs by more than 40–100% relative to the control simulation. Comparisons of the RMSE profiles among all the simulations for July 2009 show that the errors introduced by use of the built-in model BE gradually decrease with height, and are equivalent to values of the other simulations at or above 300 hPa (Figure 3.4), indicating that the negative effect is three-dimensional even though only two-dimensional data were assimilated.

As again shown in Table 3.3, improvements in wind speed and direction, as verified against QuikSCAT winds, can also be achieved by the use of customized model BEs even though no QuikSCAT data have been assimilated. The built-in model BE, however, degrades the performance of WRFDA, worsening both wind speed and direction. The improvements seen

with the customized BEs are most likely due to improved 10-m winds along the coastal areas where coastal station observations were assimilated.

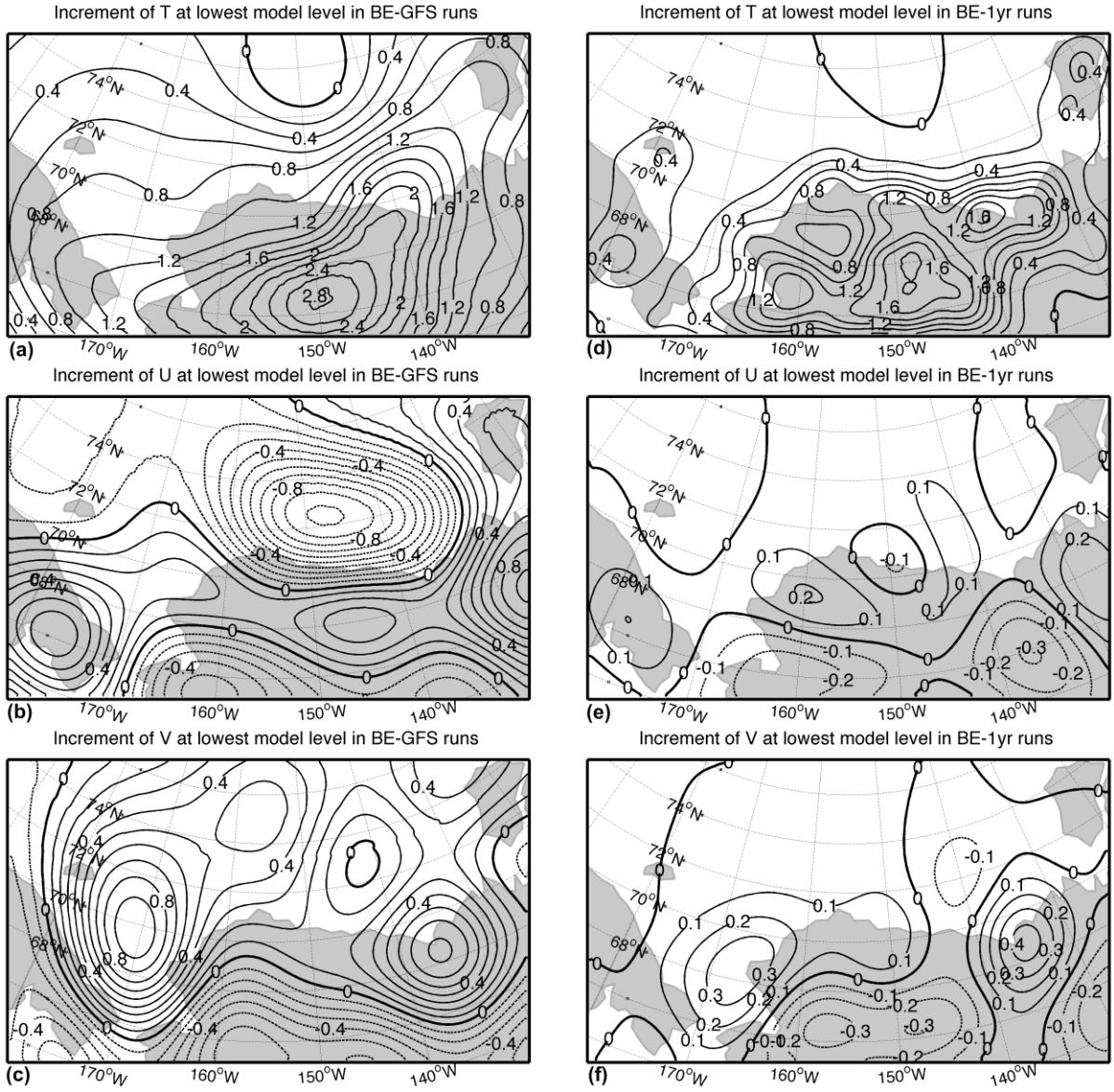

Figure 3.3. Monthly-averaged analysis increments for temperature (T) and wind components U and V as introduced by WRFDA when using BE-GFS (a, b, c) and BE-1yr (d, e, f) for July 2009. The increments are calculated by subtracting background fields from the analysis fields. Positive values are denoted by solid lines and negative values by dashed lines.

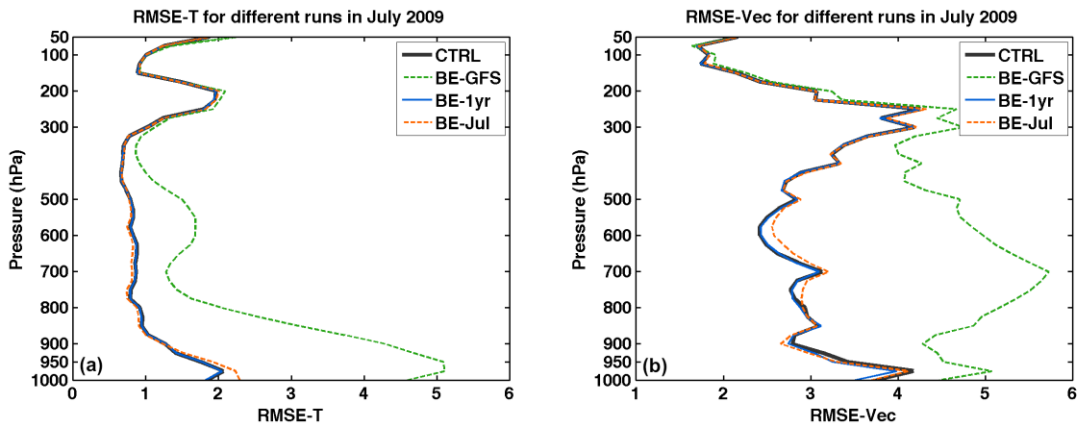

Figure 3.4. The monthly-averaged profiles of RMSE, averaged over all radiosonde stations for (a) temperature and (b) wind vector in July 2009 for the BE experiments. The RMSEs of different runs as verified against radiosonde data are calculated at various vertical levels and then averaged over the three available radiosonde stations for the entire month.

3.3.2 Performance analysis of WRFDA assimilation of multiple datasets. For a study area with a paucity of observational data coverage, multiple datasets, including both in situ observations and satellite retrievals from all available sources, have to be taken into consideration for use in the WRFDA assimilation system in order to produce a high quality regional reanalysis. As described in Section 2, we have collected and quality controlled data from a total of three radiosonde locations and 122 in situ surface stations from different data networks. Satellite retrievals, including QuikSCAT ocean-surface winds and MODIS and COSMIC retrieved profiles, have also been acquired. Will assimilation of all these data via WRFDA enhance the model's performance? To answer this question, a thorough evaluation is conducted through a series of data assimilation sensitivity experiments for July 2009 (Tables 3.4 and 3.7). All sensitivity experiments herein use the customized model BE from sensitivity experiment BE-1yr (Table 3.2). Simulation results, including 2-m temperature, SLP, and 10-m wind speed and direction, are verified against in situ surface and radiosonde observations, as well

as QuikSCAT surface winds, and the RMSEs calculated. The relative success achieved through assimilating each type of data is analyzed by comparing the RMSEs among the control and sensitivity simulations (Tables 3.5, 3.8, and 3.9). These will be detailed in the following subsections a–d.

3.3.2.1 Assimilation of in situ surface observations. Sensitivity experiment SFC (Table 3.4), in which the model BE from BE-1yr was used for the assimilation of surface station observations, is equivalent to the sensitivity experiment BE-1yr in Table 3.2 for the July case. As discussed in Section 3.1, assimilation of in situ surface observations generates improvements in most of the validated variables, particularly 10-m wind. Greater improvements are seen in the coastal region, where 2-m temperature is improved by 9% and 10-m wind by 5%, while the impact inland is relatively small. When the model results are verified against QuikSCAT winds, improvements are also seen. Therefore, the assimilation of in situ surface observations does help to improve the model performance in simulating most near-surface variables, particularly 10-m winds.

Table 3.4

Experiments to evaluate different observational sources

Experiments	**Data Assimilated**
CTRL	(No data assimilated through WRFDA)
SFC	In situ surface observations
SONDE	Radiosonde profiles
QSCAT	QuikSCAT ocean-surface winds
COSMIC	COSMIC profiles

Table 3.5

Same as Table 3, but for experiments assimilating different observational sources and for July 2009 only (In each experiment, only one observational source is assimilated, as denoted by the experiment name.)

Exp.	**RMSE**								
	Surface observation						Radiosonde		QuikSCAT
	T		SLP		VEC		T	VEC	VEC
	Coast	Inland	Coast	Inland	Coast	Inland			
CTRL	2.69	3.77	1.15	1.69	3.18	3.28	1.08	2.93	3.42
SFC	**2.44**	**3.79**	**1.05**	1.68	**3.01**	**3.13**	1.08	2.93	**3.32**
SONDE	**2.64**	3.77	**1.11**	1.68	3.16	3.27	1.06	2.91	**3.39**
QSCAT	2.68	3.78	1.15	1.66	3.18	**3.25**	1.07	2.93	**3.06**

***3.3.2.2 Assimilation of radiosonde measurements*.** Radiosondes provide in situ measurements of atmospheric temperature, moisture, and wind at vertical levels ranging from 1000 hPa to about 10 hPa twice per day. In our study area, a total of three sounding stations (Barrow, Inuvik, and Kotzebue) made measurements during the study period of July 2009; two soundings per day from each station are assimilated in the assimilation experiment SONDE (Table 3.4). The comparison of RMSEs between the CTRL and SONDE simulations (Table 3.5) indicates that the assimilation of radiosonde measurements not only improves the model's simulation of upper-air variables (where model output one hour prior to the assimilation times is used for verification in order to maintain independence from the observations), but also affects the simulation of surface variables as verified against surface in situ observations and QuikSCAT winds. Due to the very limited number of soundings available in the study area, the RMSEs of

upper-air temperatures and winds are only slightly reduced in this experiment, by about 1–2%. At the surface, 2-m temperature and SLP are improved by about 2% and 3%, respectively, in the coastal region. The 10-m wind over the ocean has also been slightly improved, as verified against QuikSCAT. Overall, this experiment indicates that a consistently positive impact can be achieved through the assimilation of radiosonde measurements.

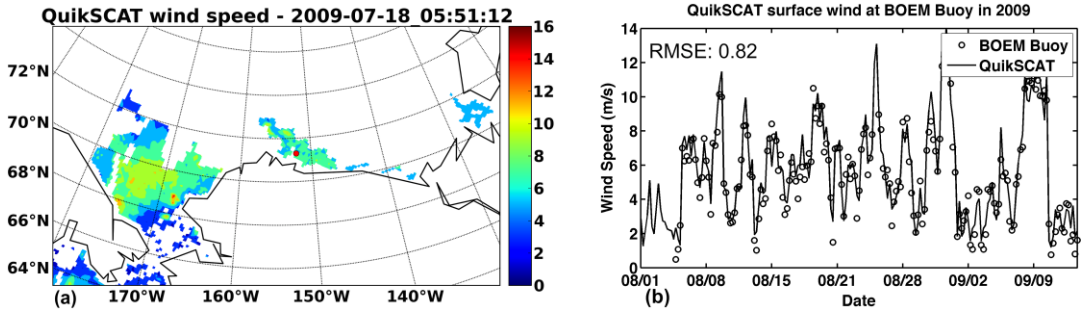

Figure 3.5. (a) Snapshot of QuikSCAT surface wind coverage in the model domain at 0551 UTC 18 July 2009; (b) QuikSCAT surface wind speed versus BOEM buoy (71.29°N, 152.14°W)-observed wind speed in August–September 2009 (b). Colors signify wind speed. Red dot in (a) represents the location of the BOEM buoy.

3.3.2.3 Assimilation of QuikSCAT surface winds. The consistently positive impact produced by WRFDA in assimilating in situ measurements gives us confidence to further extend our efforts in this study by assimilating satellite retrievals. Assimilation of QuikSCAT surface winds is evaluated with the assimilation experiment QSCAT (Table 3.4). QuikSCAT ocean-surface winds provide measurements of surface wind vectors over open water in the absence of sea ice (Figure 3.5). During the study period of July 2009, a meteorological buoy sponsored by the Bureau of Ocean Energy Management (BOEM) was deployed along the Beaufort Sea coast near Barrow, Alaska, where it collected a month-long offshore meteorological dataset of 10-m winds, among other variables (http://knik.iarc.uaf.edu/buoy09). In order to better understand the

accuracy of QuikSCAT winds in the study region, the wind speeds measured by the BOEM buoy are compared with QuikSCAT retrievals (Figure 3.5b). The correlation between the buoy measurements and QuikSCAT surface winds, calculated following Crosby's definition (Crosby et al. 1993), for the period of 5 August to 15 September 2009 is 0.83, with an RMSE of just 0.82 m s^{-1}, indicating that the quality of QuikSCAT winds in the study area is satisfactory.

During the open water season, e.g. July 2009, when there are QuikSCAT winds available in the study area, assimilation of QuikSCAT surface winds demonstrates a positive influence on the simulation of the offshore surface wind field. As before, model output from experiment QSCAT is verified against both in situ measurements and QuikSCAT winds at non-assimilation hours and the RMSE calculated (Table 3.5). From this, it's shown that assimilating QuikSCAT winds can significantly reduce the RMSE of surface wind vectors over open water as verified against unassimilated QuikSCAT winds. Wind vectors are improved by 11% relative to the control run.

The spatial distribution of the impacts of assimilating QuikSCAT surface winds can be depicted by the near-surface analysis increments, calculated by subtracting the model background field from the analysis field at the lowest model level. The increments of the wind components U and V, averaged over the simulation period (Figure 3.6), demonstrate that the zonal wind (U) is increased over the Chukchi Sea by roughly 0.2 m s^{-1}, and by 0.1–0.5 m s^{-1} in the Beaufort Sea coastal areas. Positive increments of the meridional wind (V) exhibit an adjustment of 0.1–0.3 m s^{-1}, centered on the Alaskan Chukchi Sea coast and extending eastward along the coast. The increments also demonstrate how winds oriented parallel to the coast are improved. Larger increments for such winds are due to that the surface wind regime in the coastal region is dominated by coast-parallel winds. Comparing the wind field increments

introduced by assimilating QuikSCAT surface winds with in situ surface observations (Figure 3.6 and Figure 3.3e–f) demonstrates that the areas where data are assimilated always receive greater impacts. The distribution of the 10-m wind field increments caused by the assimilation of QuikSCAT winds agrees well with the QuikSCAT data coverage (Figure 3.5a) over the Chukchi Sea and Beaufort Sea coastal area. Thus, improved offshore 10-m winds are achieved in a region where few offshore in situ measurements are available via the assimilation of QuikSCAT surface winds.

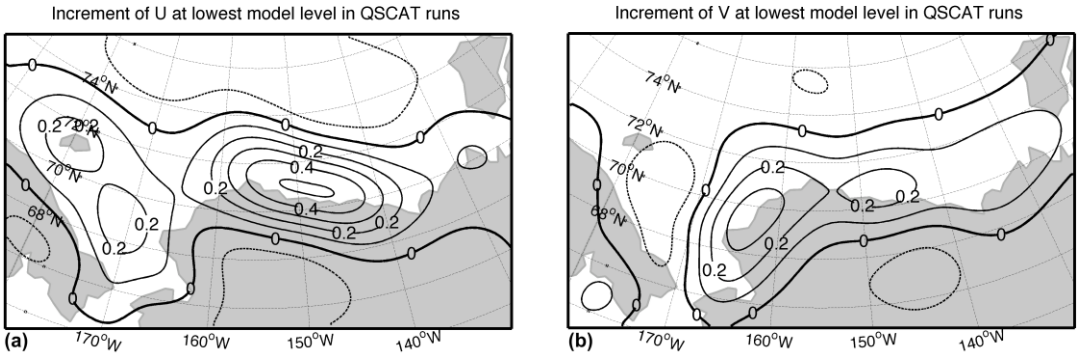

Figure 3.6. Monthly-averaged analysis increments for the wind components (a) U and (b) V introduced by assimilating QuikSCAT data in July 2009. The increment is calculated by subtracting background fields from the analysis fields. Positive values are denoted by solid lines and negative values by dashed lines.

3.3.2.4 Assimilation of satellite-retrieved profiles. An extreme lack of radiosonde observations in the study area motivates us to include as many satellite-retrieved profiles as possible via the WRFDA assimilation system for the production of the CBHAR reanalysis. Assimilating satellite retrievals and/or radiance data has demonstrated the ability to improve in model simulations (Pu et al. 2002; Fan and Tilley 2005; Huang et al. 2005). Directly assimilating radiance data is recommended in order to avoid potential negative impacts as a result of retrieved profiles providing insufficient accuracy and/or vertical resolution. However, assimilation of

satellite-retrieved profiles also displays the ability to improve the model results particularly in remote and data-sparse areas, in some case, even outperforms the performance of directly assimilating radiance data (Singh et al. 2012). MODIS-retrieved temperature and humidity profiles, when assimilated by a forecast model, have been shown to improve the forecast (Xavier et al. 2006; Zhang et al. 2007). Assimilation of COSMIC profiles has also demonstrated improvements to model simulations through the reduction of model bias (Cucurull and Derber 2008). Thus, the satellite-retrieved temperature and moisture profiles from the MODIS and COSMIC instruments are targeted for use in this study.

MODIS profiles have much higher spatial and temporal resolution than do radiosonde measurements, with 2–3 satellite passes per day occurring over some part of the study domain and the data available at a horizontal resolution of about 5 km. After the data is thinned to a spacing of approximately 120 km in order to prevent oversaturation, which can cause diminished results (e.g., Liu and Rabier 2002), there remain approximately 1900 MODIS profiles per day across the model domain available to be assimilated by WRFDA.

Table 3.6

MODIS retrieval QC flags

Flag	**Interpretation Key**
Cloud Mask (CM)	0 = Confidently Cloudy
	1 = Probably Cloudy
	2 = Probably Clear
	3 = Confidently Clear
Snow/Ice Background (SI)	0 = Yes
	1 = No

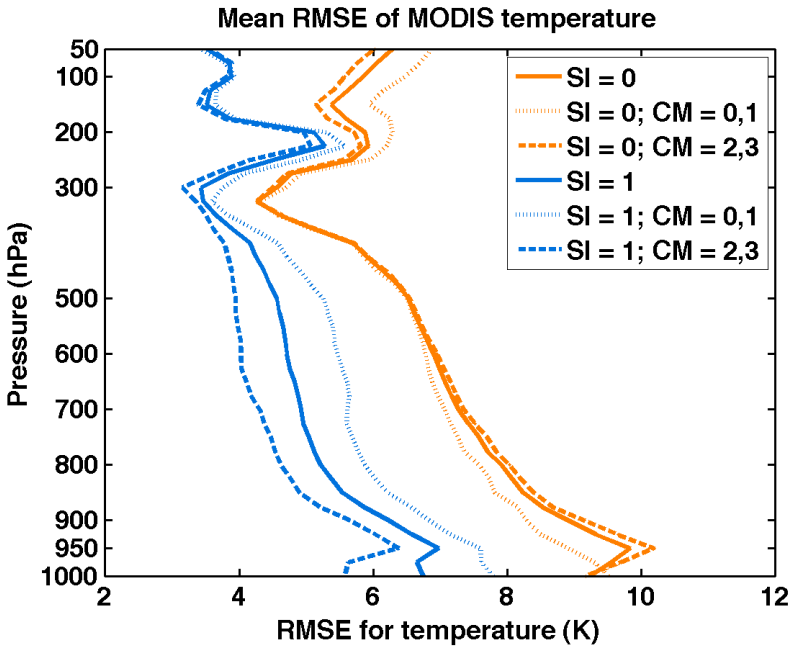

Figure 3.7. Average RMSE profiles for temperature in 2009 over all radiosonde stations with the use of different quality-control flags. MODIS profiles are categorized into six groups according to their SI and CM flags as shown in the legend and compared with radiosonde profiles observed within a 1-hour time window.

Table 3.7

MODIS assimilation experiments

Experiments	Snow/Ice background (SI)	Cloud mask (CM)	Vertical levels
MODIS	All backgrounds SI=0, 1	All conditions CM=0, 1, 2, 3	All levels
MODIS-MID	All backgrounds (0, 1) SI=0,1	All conditions CM=0, 1, 2, 3	850–300 hPa
MODIS-QA	Snow/ice-free background SI=1	Clear sky CM=2, 3	All levels

In the retrieval product, each MODIS profile is given flags that indicate the quality of the profile and the conditions under which it was collected. Two examples include the cloud mask flag (CM), which indicates the presence of clouds, and the snow/ice background flag (SI), which indicates if the background was covered by snow or sea ice (Table 3.6). By taking note of these flags, users can assess how the profile accuracy varies under different conditions. To characterize the quality of data marked by these flags in the study area, the MODIS profiles for 2009 are first divided into six groups according to their CM and SI flags (snow/ice background under all sky (SI=0); snow/ice background under cloudy sky (SI=0, CM=0,1); snow/ice background under clear sky (SI=0, CM=2,3); snow/ice-free under all sky (SI=1); snow/ice-free under cloudy sky (SI=1, CM=0,1); and snow/ice-free under clear sky (SI=1, CM=2,3)) and then verified against radiosonde observations at the three sounding stations within the model domain. The MODIS profiles within each flag category are calibrated by calculating RMSE against the radiosonde profiles measured at approximately the same time (within a 1-hour window). A comparison of temperature RMSE profiles among the six flag categories (Figure 3.7) shows that the profiles retrieved under a snow or ice background (SI=0) contain errors that are 30–50% larger than those without (SI=1). A similar contrast is present between profiles retrieved under cloudy conditions (CM=0,1) and under clear sky (CM=2,3). In addition, the data errors are highly variable with height. The RMSE at 1000 hPa is up to two times larger than at upper levels (850 to 300 hPa).

Considering the variations in MODIS profile quality, as exhibited in Figure 3.7, a series of sensitivity experiments (Table 3.7) in which MODIS profiles are screened by the CM and SI flags and data errors examined in Figure 3.7, have been conducted in order to determine the optimal configuration for assimilating MODIS profiles via WRFDA. In these experiments, MODIS data are either assimilated at all levels (MODIS) or between 850 and 300 hPa (MODIS-

MID). The sensitivity simulations are evaluated in the same way as before, with the model results (SLP, T, and VEC) verified against radiosondes, surface observations, and QuikSCAT winds. Comparisons of the results from the sensitivity experiments MODIS, MODIS-MID, and CTRL (Table 3.8) demonstrate that assimilation of unfiltered MODIS retrievals (experiment 'MODIS') makes the results worse relative to the CTRL simulation for almost all examined variables. The experiment 'MODIS' produces 10-m wind (VEC) RMSE more than 2% larger than CTRL over land, and more than 7% larger over the ocean. Perhaps surprisingly, the experiment MODIS-MID, in which the retrieval levels are selectively assimilated, doesn't produce any improvement over the degraded performance of the 'MODIS' experiment. The results from MODIS-MID are also worse than CTRL, with RMSEs about 3% larger for 10-m wind and 1% larger for 2-m temperature in the coastal region.

Table 3.8

Same as Table 3.3, but for experiments assimilating MODIS profiles and for July 2009 only

Exp.	**RMSE**								
	Surface observation						Radiosonde		QuikSCAT
	T		SLP		VEC		T	VEC	VEC
	Coast	Inland	Coast	Inland	Coast	Inland			
CTRL	2.69	3.77	1.15	1.69	3.18	3.28	1.08	2.93	3.42
MODIS	**2.74**	3.77	**1.11**	1.66	**3.30**	**3.36**	**1.16**	**3.19**	**3.69**
MODIS-MID	**2.73**	3.79	**1.12**	1.66	**3.27**	**3.38**	**1.14**	**3.09**	**3.60**

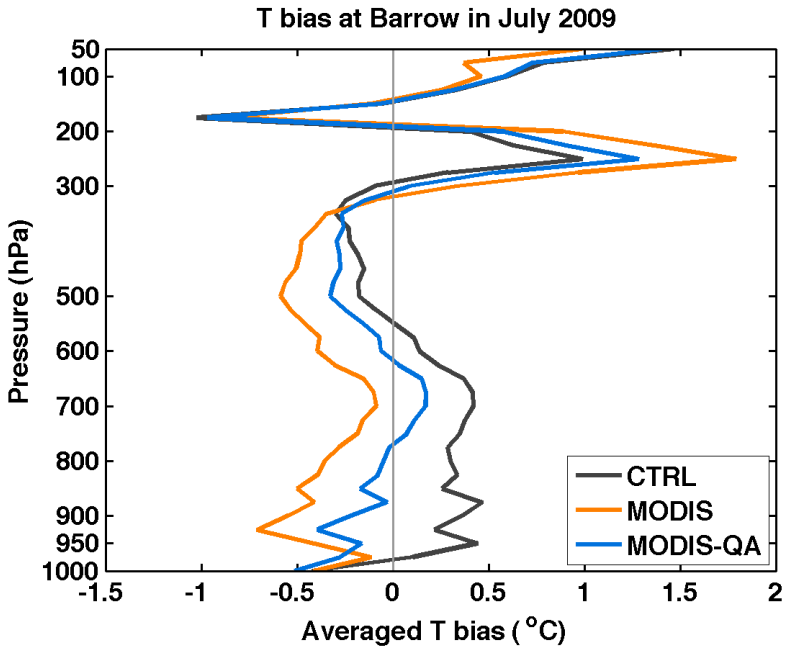

Figure 3.8. Monthly-averaged profiles of temperature bias at Barrow in July 2009 for experiments CTRL, MODIS, and MODIS-QA, as verified against radiosonde data at various vertical levels.

In addition to the selective experiment MODIS-MID, the MODIS profiles can also be screened through the use of the CM and SI flags. An additional experiment, MODIS-QA, is conducted to examine the performance when assimilating only MODIS profiles that have a snow/ice-free background (SI=1) and were retrieved under either probably clear (CM=2) or confidently clear sky (CM=3) conditions. In order to understand the vertical effects of assimilating MODIS retrievals, model-simulated temperature profiles from the experiments CTRL, 'MODIS', and MODIS-QA are compared at all levels and averaged over the entire simulation period of July 2009 at Barrow (Figure 3.8). Comparisons of the monthly-averaged bias profiles among all the sensitivity tests show that the unfiltered experiment 'MODIS' overcorrects the warm bias generated by the CTRL experiment in the middle and lower atmosphere (below ~500 hPa), producing a cold bias of up to 0.5 °C. When the MODIS profiles

are selectively assimilated on the basis of quality assurance flags (experiment MODIS-QA), an improvement is seen in temperature for almost all levels, reducing both the cold bias in the middle and lower atmosphere (below ~300 hPa) and the warm bias in the upper atmosphere (above ~300 hPa). Selectively assimilating MODIS profiles via the WRFDA system through the use of quality assurance flags, such as those indicating snow/ice-free background and/or clear sky conditions, is therefore essential for avoiding degradation of assimilation performance. This further confirms the results of previous studies that, before using satellite-retrieved products, the data should be filtered in order to diminish the possible negative impacts from poor-quality retrievals (Key et al. 2003; Powers 2007).

COSMIC-retrieved profiles have about 20 profiles per day in the study domain. The profiles originally have 400 vertical levels, but are thinned to 26 vertical levels to prevent oversaturation. When evaluating the effect of assimilating COSMIC profiles, the filtering procedure used in the MODIS experiments is not applied. COSMIC products are not accompanied by QC-flag information, suggesting that third-party sources are required in order to conduct a filtering procedure, which may cause some inconsistencies. In addition, the radio occultation technique used by COSMIC is known to be minimally affected by clouds (Anthes 2000). The experimental results (COSMIC) are verified separately against surface station (coastal and interior stations separately), radiosonde, and QuikSCAT observations for temperature, SLP, and wind (Table 3.9). Despite the lack of quality assurance, the assimilation of COSMIC profiles doesn't produce negative impact for both surface and upper-air variables, which encourages us to consider including the COSMIC profiles in the WRFDA assimilation system for ultimately generating the CBHAR reanalysis.

Table 3.9

Same as Table 3.3, but for the experiment assimilating COSMIC profiles and for July 2009 only

Exp.	**RMSE**								
	Surface observation						Radiosonde		QuikSCAT
	T		SLP		VEC		T	VEC	VEC
	Coast	Inland	Coast	Inland	Coast	Inland			
CTRL	2.69	3.77	1.15	1.69	3.18	3.27	1.08	2.93	3.42
COSMIC	2.71	3.76	**1.10**	1.67	3.18	3.26	1.07	2.92	3.42

3.4 One-year Experiment Reanalysis

Synthesizing the results achieved in the previous sensitivity experiments, a one-year experimental reanalysis is generated in order to ensure that the selected observation types function as expected when they are combined within a single assimilation system. The experimental reanalysis is generated for 2009, using the modeling configuration listed in Table 3.1. The one-year experiment uses the same cycling scheme as the previous experiments (Figure 3.1). In addition, spectral nudging to the forcing dataset (ERA-I), is also employed in the experimental reanalysis in order to maintain consistency between this modeling configuration and the one ultimately used to generate the final CBHAR reanalysis. The spectral nudging is configured to use wave-number 3 and nudging is performed at all vertical levels and for all variables.

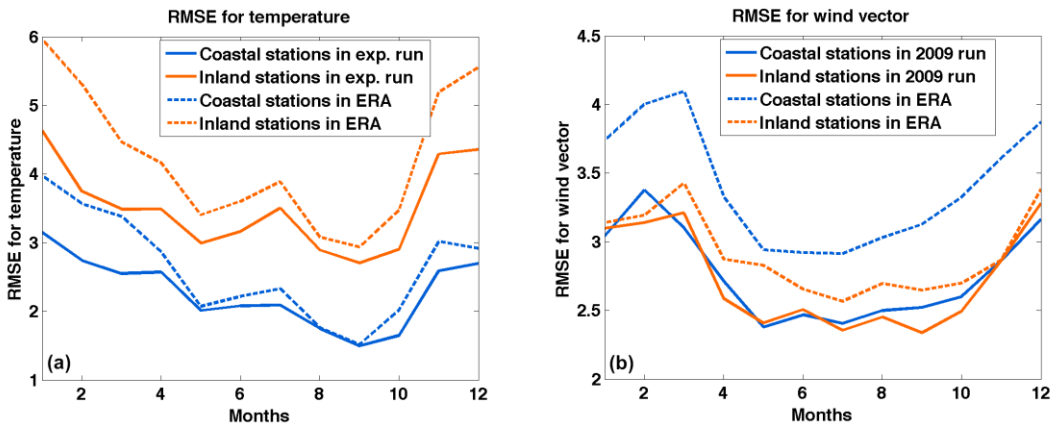

Figure 3.9. Seasonal variations of RMSE, averaged over coastal stations (blue lines) and inland stations (orange lines) for (a) temperature and (b) surface wind vector in the one-year experimental reanalysis (solid) and ERA-Interim (dashed).

The results are here again analyzed using RMSE of the simulation output as calculated against observations. In this section, the near-surface variables 2-m temperature (T) and 10-m wind vectors (VEC) are solely verified at in situ surface stations, since these provide the most accurate observations throughout the entire year (Figure 3.9). The RMSEs of T and VEC are separately averaged over coastal stations, defined as those located within 30 km of the coastline, and inland stations, comprising the remainder. RMSEs of the same fields from ERA-I are also calculated in the same manner for purposes of comparison. Relative to ERA-I, the experimental reanalysis demonstrates consistent improvements for all variables examined. The temperature is improved to a larger degree in colder months than in the warm season. In contrast, improvements to the 10-m wind field do not exhibit a significant seasonal variation. The results demonstrate that errors are generally lower in the warmer months, when variability in atmospheric conditions is at a minimum, and greatly increase during the winter. During May to October, the RMSE of VEC is 17% less than in the cold season from November to April. The differences between coastal stations and inland stations are not significant. For temperature, similar seasonal

variations are observed, with the minimum RMSE occurring in September. The model performs differently for inland and coastal areas, with 26–45% smaller RMSE in coastal areas throughout the year. This differential performance in inland versus coastal regions is consistent with the results shown in previous sections. In addition to the effects of higher atmospheric variability, the larger errors seen in winter can also be attributed to the model's relatively poor performance in simulating strong, shallow surface-based inversions.

Accurate surface wind field is one of the greatest concerns to the oil spill and ocean current modeling. How well does the experimental reanalysis capture the detailed mesoscale processes in the surface winds? To answer this, monthly 10-m wind rose between observation, experimental reanalysis, and ERA-I are compared along three coastal stations as shown in Figure 3.10. Stations Mys Shmidta and Barter Island are two stations close to the Chukotka Mountain range and the Brooks Range, respectively; and the wind rose from them during the cold month can be used to demonstrate the mountain barrier effect. Station Kivalina is a station along the Chukchi Coast, receiving less topographic impact from the distant Brooks Range, and wind rose at this location during a warm month can be used to show the sea breeze effect. Overall the one-year experiment tends to have better agreement with the observation, producing more accurate distribution of certain wind directions comparing to ERA-I. At Mys Shmidta in April, the dominant observed 10-m wind regime, oriented parallel to the Chukotka Mountain range due to the mountain barrier effect turning synoptic northeast winds to northwest (Stegall and Zhang 2012), is well captured in the one-year experiment, while ERA-I includes a greater cross-range 10-m wind component. At Barter Island in March, the high frequency of westerly wind, again due to the mountain barrier effect, which turns synoptic north winds to west (Stegall and Zhang 2012), is also missing in ERA-I. At Kivalina, during the period from June 16-21, a weak

synoptic condition (not shown) favors the generation of westerly sea breeze along the coast. This feature of sea breeze is well captured by the one-year experimental reanalysis. This comparison demonstrates the ability of one-year experimental reanalysis to provide added information to surface wind field particularly for the areas of highly variable topography, and how the simulation of such winds can benefit from higher modeled spatial resolution.

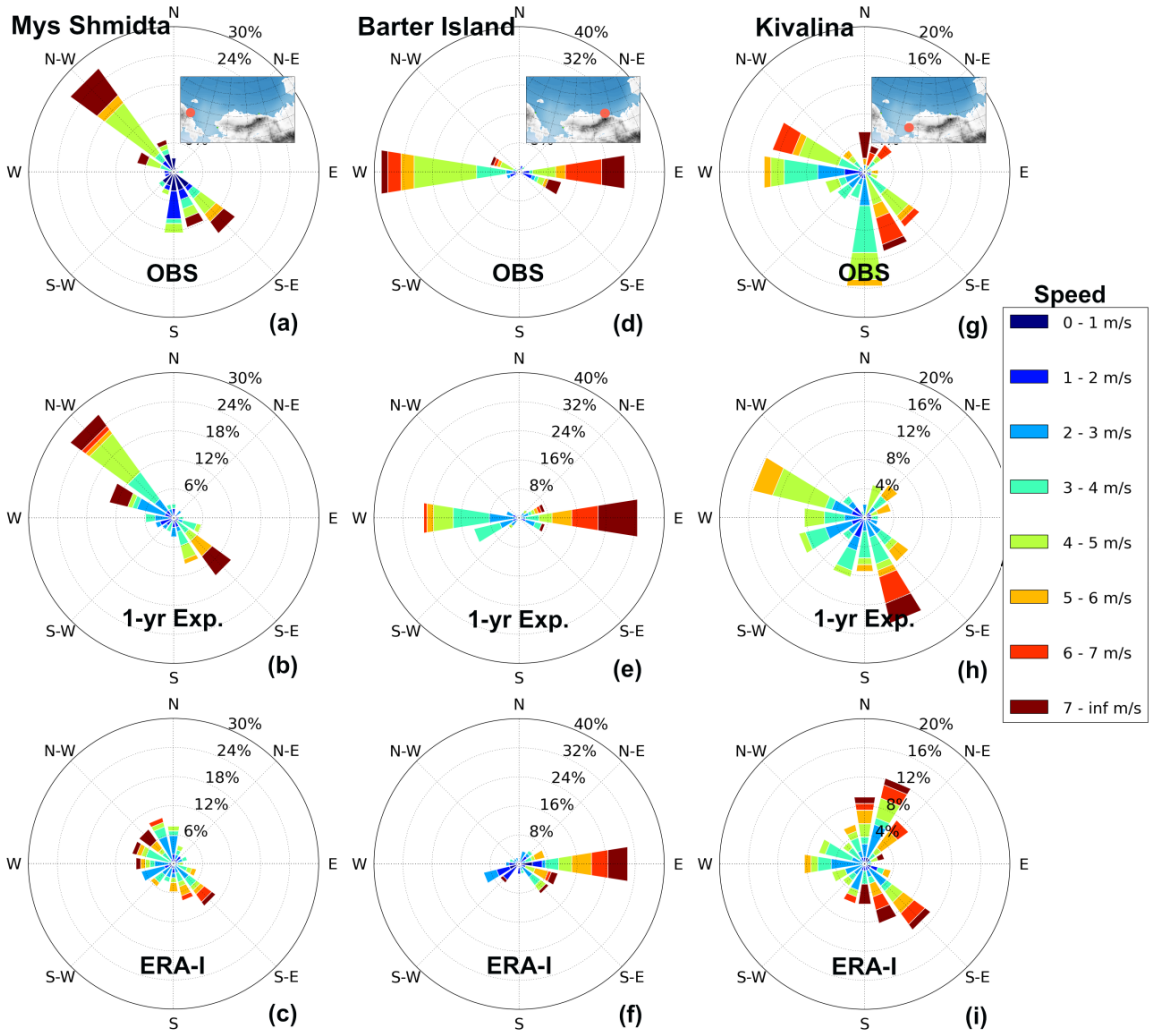

Figure 3.10. Comparison of 10-m wind roses between the one-year experimental reanalysis (1-yr Exp.), ERA-Interim (ERA-I), and observations (OBS) at Mys Shmidta (April, a, b and c), Barter Island (March, d, e, and f), and Kivalina (June, g, h and i) in 2009 (station location marked with red dot in the embodied domain map).

3.5 Summary

The WRFDA is optimized for investigating the 10-m wind field along the Chukchi and Beaufort Seas and Arctic Slope of Alaska. A series of assimilation sensitivity experiments, in which different BEs are used or different observational data are assimilated, are conducted and analyzed by comparing the resultant RMSEs as calculated against unassimilated observations with those from a control experiment (CTRL).

The experiments evaluating model BE suggest that the usage of the built-in global BE (BE-GFS) included in the WRFDA package should be avoided in this study, as its use contributes to significantly degraded simulations in both winter and summer, and for all examined variables checked, relative to CTRL. In contrast, the usage of customized BEs (BE-1yr and BE-Jul) serves to improve the simulations. On average, the customized model BE can improve the 10-m wind and 2-m temperature in coastal areas throughout the diurnal cycle, while usage of BE-GFS degrades the results, particularly for daytime 2-m temperatures. The analysis increments generated by using the built-in BE exhibit larger spatial-scale features, as well as unrealistic adjustments over the ocean. The degraded performance of BE-GFS can be attributed to its presumably inaccurate representation of errors for the regional model used here, generated as it was from global GFS simulations with a horizontal grid spacing about 80 km, compared to the 10 km used by WRF in this study.

Assimilating in situ surface observations and radiosonde measurements produces highly responsive results. The verified surface variables are significantly improved, particularly in coastal areas during the summer, through the assimilation of in situ surface observations. Assimilating radiosonde profiles improves the simulation of upper-air variables, and slightly improves ocean-surface winds.

QuikSCAT data provide distinctive coverage of surface wind fields over open water, and when assimilated contribute to significant improvements in the simulation of sea-surface winds, with a reduction in error of as much as 11%. Assimilating QuikSCAT data enhances the zonal winds over the Chukchi Sea and the coastal areas of the Beaufort Sea. The meridional winds are enhanced along the Chukchi and Beaufort coasts of Alaska. The spatial pattern of the analysis increments is co-located with the QuikSCAT data coverage.

Experiments assimilating MODIS data reveal the need for the careful selection of the particular profiles to be assimilated in order to avoid the negative impacts that use of the entire dataset otherwise introduces. Assimilating all MODIS data, regardless of quality, makes most examined variables worse than in the CTRL experiment. When the profiles are screened through use of the cloud mask and snow/ice background flags, the negative impacts are mostly dispelled and the cold bias in the middle and lower atmosphere (below ~300 hPa) and warm bias in the upper atmosphere (above ~300 hPa) are significantly improved.

In order to ensure that the performance of the combination of selected model background error and observation types is consistent with the individual sensitivity tests, a one-year experimental reanalysis for 2009 is generated. The experimental reanalysis further confirms that consistent improvements are achieved for all examined variables. Relative to ERA-Interim, larger improvements in temperature are demonstrated in colder months than in the warm season. The errors in the experimental reanalysis exhibit significant seasonal variation, with lower values in the warmer months while greatly increasing in the winter. Mesoscale processes including mountain barrier and sea breeze effects are also well captured in the surface wind field reanalysis.

CHAPTER 4

Mesoscale Climatology of Surface Winds in the Chukchi-Beaufort High-Resolution Atmospheric Reanalysis (CBHAR)

4.1 Introduction

Strong potential of further offshore energy development in the Chukchi-Beaufort Seas has caused increasing attention from the government, scientific community, and general public to the threat of oil spill (e.g., Gundlach and Hayes 1978; Picou et al. 2009; Webler and Lord 2010). In order to be able to accurately predict the dispersal and movement of oil spills, and to assess the potential environmental impacts should a spill occur, a good understanding of detailed surface wind climatology and changes in the Chukchi-Beaufort Sea region is imperative.

Both prevailing synoptic weather patterns and prominent underlying geographic features play roles in determining the surface wind climate (e.g., Schwerdtfeger 1974; Kozo 1980; Moore and Pickart 2012). In the Chukchi–Beaufort Seas region, surface winds vary in response to the intensity and location of the Beaufort High and Aleutian Low, which are the dominant synoptic-scale weather patterns in the area (Shulski and Wendler 2007; Overland 2009; Moore 2012; Zhang et al. 2013). Surface winds are further modulated by local geographic features through both thermodynamic and dynamic processes (Kozo 1979, 1980; Liu et al. 2008). Land and ocean respond differently to incoming solar radiation, generating horizontal temperature gradients, which in turn cause land/sea breezes (Lyons and Olsson 1972; Kozo 1979, 1980; Liu and Olsson 2008). The same mechanism also exists in the mountainous areas, where mountain slopes are more readily heated than the horizontally adjacent air, causing upslope valley breezes. When solar radiation is weak or not present, the air near the terrain surface is cooled faster than the adjacent air through the loss of outgoing longwave radiation, resulting in denser surface air over

the terrain and a resultant downslope wind (also referred to as gravity drainage) (Thorpe et al. 1980; Parish 1987, 1991, 2003; Bromwish 1989; Lin 2007). Topography can also impact the surface wind dynamically. For example, when an air mass characterized by a low Froude number (U/NH, where U is the speed of the basic current, N is the Brunt–Väisälä frequency, and H is the mountain height) flows toward a mountain barrier, its approach will be blocked due to having insufficient kinetic energy to flow over the mountain. The accumulated air mass alters the distribution of pressure so that the flow is deflected to the left and finally turns, becoming parallel to the mountain range. This effect is known as mountain barrier effect or cold air damming (Schwerdtfeger 1974; Kozo 1980; Bell and Bosart 1988; Xu et al. 1996; Lin 2007).

Understanding climatology and changes of mesoscale features of surface wind field in the Chukchi-Beaufort Seas region is also challenging due to the harsh and complex Arctic environment and significant changes during recent decades. The study area is located in the marginal ice zone of Arctic, which is experiencing the fastest rate of sea ice decline and maximum observed interannual variance of sea ice anywhere in the Arctic (Stroeve et al. 2007; Comiso et al. 2008), as well as enhanced surface winds as sea ice retreats (Stegall and Zhang 2012). In addition, meteorological observations in the harsh Arctic region are also sparse, which hindered any detailed analysis of mesocale wind field features in the study area. The newly developed 31-year, 10-km resolution Chukchi-Beaufort High Resolution Atmospheric Reanalysis (CBHAR) (Zhang et al. 2013; Liu, et al. 2013) thus provides a unique opportunity for conducting mesoscale climatology analysis of the surface wind field in the Chukchi-Beaufort Seas region.

This chapter is organized as follows. Section 2 breifly describes the CBHAR data used in this study, as well as a briefly description of the study domain. Section 3 presents the overall

climatological features of mesoscale winds in the study area. Mesoscale winds including sea breeze, up/down-slope winds, and cold air damming are detailed in Sections 4-6. The variability of the sea breezes and mountain barrier effect are discussed in Section 7. A summary of this study is given in Section 8.

4.2 CBHAR Data and Domain

The newly generated regional high-resolution reanalysis CBHAR (Zhang et al. 2013; Liu et al. 2013) is utilized to detail mesoscale climatology and changes of surface wind field in the Chukchi-Beaufort Seas. CBHAR was generated to provide a long-term high-resolution atmospheric reanalysis covering the Chukchi-Beaufort Seas region for the period from 1979 - 2009. The data has high spatial resolution, with a grid spacing of 10 km, and a temporal resolution of 1 hour, making it able to resolve fine-scale mesoscale processes. The Weather Research and Forecasting (WRF) model (Skamarock et al. 2008) and its Data Assimilation system WRFDA (Huang et al. 2009; Barker et al. 2012) are the vehicle generating CBHAR. Following a series of sensitivity simulation experiments, the WRF and WRFDA are optimized for the study area and the model configuration parameters are listed in Table 4.1.

Table 4.1

WRF and WRFDA configurations for CBHAR

	Options	**Configuration**
Physics	Microphysics	Morrison 2-moment (Morrison et al. 2009)
	Longwave radiation	Rapid Radiative Transfer Model for GCMs (RRTMG) (Iacono et al. 2008)
	Shortwave radiation	RRTMG (Iacono et al. 2008)
	Planetary boundary layer	Mellor-Yamada-Janjic (Eta) (Hong et al. 2006)

Table 4.1

Cont.

	Surface layer	Monin-Obukhov (Janjic Eta) (Janjic 1994, 1996, 2002)
	Land-surface model	Noah land-surface model (Chen and Dudhia 2001)
	Cumulus	Grell 3D (Grell and Devenyi 2002)
	Forcing data	ERA-I
Grid	Horizontal grid spacing	10 km
	Vertical levels	49 levels with top at 10 hPa
WRFDA	Method	3DVar (Barker et al. 2004)
	Surface assimilation option	2
	Background error	Customized BE using NMC method (Parrish and Derber 1992) based on 1-year simulation of 2009
	Time interval	Hourly
	Data assimilated	Surface observation
		Radisondes
		QuikSCAT ocean-surface winds
		Selected MODIS profiles
		MODIS and AVHRR polar winds

The CBHAR reanalysis, particularly surface winds, are also verified against in-situ surface observations collected mainly from NCDC, which comprise over 100 stations across the entire CBHAR domain. CBHAR winds are interpolated to the station locations using a standard bilinear interpolation, and the statistical measures of root-mean-square error (RMSE) are

calculated for each month of the year and each hour of the day, in order to depict the seasonal and diurnal evolution of the performance of CBFAR winds. To provide a baseline against which CBHAR data could be compared, the ERA-I reanalysis data that were used as initial and boundary conditions for CBHAR are verified in the same manner.

The statistics of surface wind vector, as shown in Figures 4.1-2, suggests that wind vector RMSE is largest in the winter months, when the variability of weather conditions is high, and declines during the summer, when the variability is at its minimum. Comparing to the 6-hourly ERA-I reanalysis, error reductions in CBHAR wind vector are seen for every season of the year and all four hours of the day. These results demonstrate the consistently improved quality of the reanalyzed surface winds in CBHAR and give us confidence to utilize this dataset for mesoscale climatology analysis of the surface wind field in the Chukchi-Beaufort Seas region.

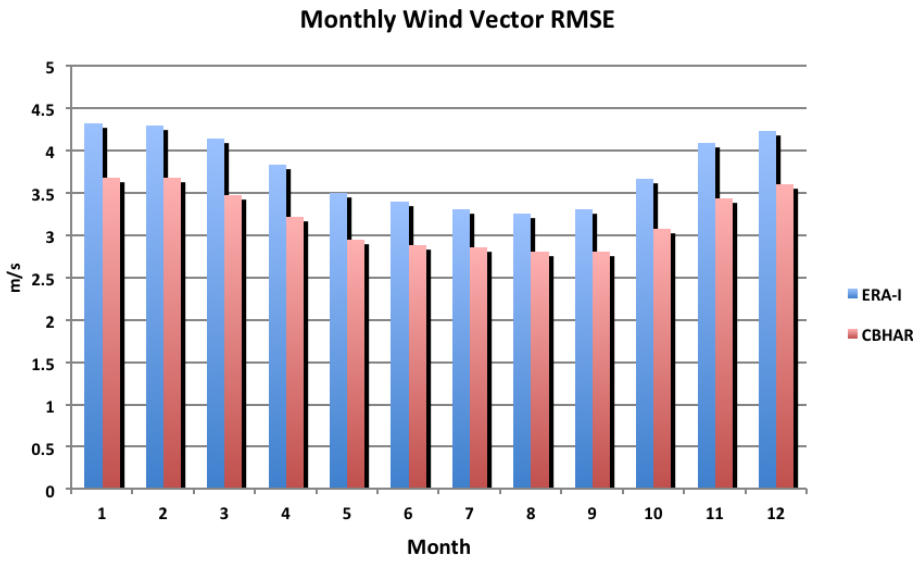

Figure 4.1. Monthly-averaged RMSE of wind vector (m s^{-1}) in CBHAR (red) and ERA-Interim (blue), as verified against surface observations.

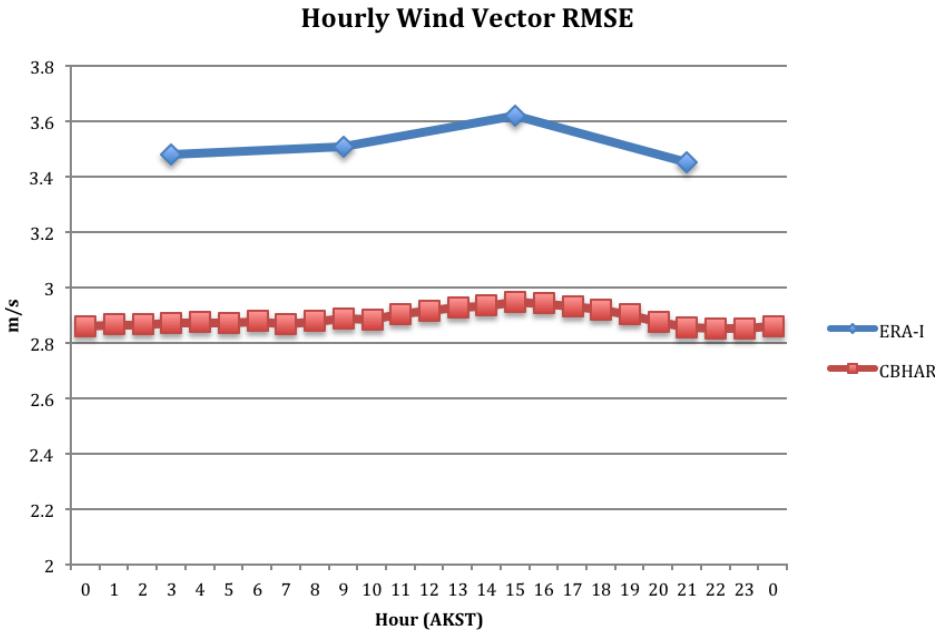

Figure 4.2. Hourly-averaged RMSE of wind vector (m s^{-1}) in CBHAR (red) and ERA-Interim (blue), as verified against surface observations.

To facilitate analysis and discussion presented in this chapter, the CBHAR data domain is shown in Figure 4.3, with superimposed sea ice and geographic features, along with the vertical cross-sections and surface sections used in various mesoscale wind field analysis. The CBHAR domain encompasses the Chukchi and Beaufort Seas, the entire Arctic Slope of Alaska and adjacent Brooks Range, along with portions of the Canadian Yukon and the eastern tip of Siberia. In order to reduce biases potentially caused by the use of a single section, a series of cross-shoreline/mountain profiles (P1-P4 in Figure 4.3) are chosen in the areas of interest and the wind fields averaged across these profiles are analyzed. A total of four cross-section profiles are selected for the examination of vertical wind structures, including inland areas of the Chukotka Mountains (P1) and two coastal areas (P2, P3), as well as the Brooks Range (P4). Along the vertical profiles, the horizontal winds were transformed in order to define components perpendicular and parallel to the vertical section, i.e., wind components were oriented relative to

the shoreline or the orientation of the mountain ranges. The climatology of the wind along the vertical sections was constructed at each hour of the day for different months. The shoreline-parallel sections (A, B, C, and D lines in Figure 4.3) are selected and the wind fields averaged along these sections at each hour of the day for different months are utilitzed to analyze the variations of sea breeze as impacted by the relative distances to the shoreline.

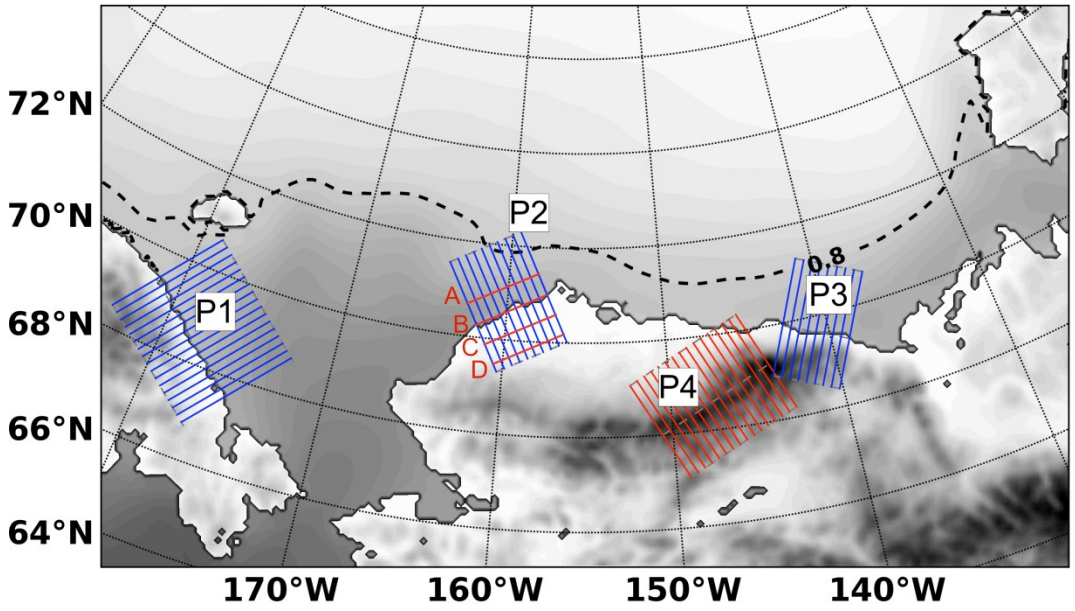

Figure 4.3. CBHAR data domain with vertical cross-section pofiles (P1-P4) chosen for various meoscale wind field analysis and shoreline-parallel sections A, B, C, and D for sea breeze variation analysis. Gray shading over ocean represents climatology sea ice concentration over the entire CBHAR period (lighter colors signify higher SIC), with the 0.8 value highlighted by the dashed line. Gray shading over land represents topography with lighter colors for low elevations.

4.3 Mesoscale Climatology of Surface Winds in CBHAR

4.3.1 Diurnal variation. Mesoscale winds with strong diurnal variation include sea breezes and up/downslope winds, which are both generated by horizontal thermal contrasts due

to different thermodynamic characteristics of different geographic surfaces. For example, water has a much larger heat capacity than soil. Land is thus heated faster during the day than adjacent ocean or lake areas in the summer. For the same reason, radiative cooling also cools the land faster at night. As a result, horizontal temperature contrasts may exist during both the daytime and nighttime, driving the motion of air currents in coastal areas (Lyons and Olsson 1972; Kozo 1979, 1980; Dailey and Fovell 1999; Liu and Olsson 2008). A similar process occurs in the vicinity of mountain valleys, where the air over the mountain and valley surfaces experiences differential heating. Air over the warmer surface experiences more heating and tends to ascend to upper levels. The pressure near the surface is thus decreased and correspondingly increased at higher levels, resulting in a horizontal pressure gradient both near the surface and at upper levels. This then causes cool air to flow towards the warmer surface at lower levels and warmer air to flow in the opposite direction at higher levels, resulting in an up/downslope circulation pattern (Orville 1964,1968; Raymond 1972; Smith and Lin 1982; Tripoli and Cotton 1989; Banta 1990; Wolyn and McKee 1994).

Diurnal cycle of solar radiative heating produces time-varying horizontal temperature contrasts and associated thermodynamically driven flows throughout the day. Based on this fact, climatological sea breezes and up/downslope winds can be identified through the following calculations. The surface wind field is first averaged over the 31-year record at each hour of the day, separated by month, such as July, in order to obtain the monthly climatological diurnal surface wind. The sea breezes and up/downslope winds are then identified by subtracting the climatological mean at a given reference time when the local thermodynamic effects are minimal. In this study, 0600 AKST during July was chosen as the reference time, based on the fact that

diurnal variation in surface winds is the strongest in July for the study area and the areal averaged solar radiative forcing is the weakest at 0600 AKST.

The diurnal variations of surface winds in July mainly occur over the mountainous and coastal areas (Figure 4.4), confirming that sea breezes and up/down-slope winds are the major contributors to the diurnal variation of surface winds in the area. In July, the area's regional scale winds are dominated by an anti-cyclonic flow centered in the Beaufort Sea under the influence of the Beaufort High, and several cyclonic flows due to thermal lows over land and warm water (Figure 4.4a). Due to the fact that there is polar day in the study area during July and ice-covered ocean offshore, land surface is always warmer throughout the entire diurnal cycle. Thus even at 06:00AKST, surface winds along some coastal areas are enhanced due to the coupling between regional scale winds and sea breezes. The constant land-sea temperature contrast suggests that sea breezes occur during the entire daily cycle along the shoreline, though the strength varies temporally (Figure 4.4b-h), with weak onshore flow in the early morning and stronger onshore flow in the afternoon. The maximum sea breeze occurs in the late afternoon at around 1500 AKST, with maximum wind anomalies of 1 to 2 m s^{-1}, though varies in different areas. Along the Chukchi Sea coastline, the sea breeze can reach 3 m s^{-1} in July, whereas the Beaufort coast experiences a relatively weak sea breeze of about 2 m s^{-1}.

Mountain up/down-slope winds occur over the mountainous areas. Along the Brooks Range, upslope winds are developed when the underlying surface is heated. The maximum upslope wind occurs in late afternoon around 1500 AKST, with maximum wind speeds of up to 2–3 m s^{-1} in the eastern Brooks Range. Downslope winds happen around the hours 00:00 to 06:00 AKST. Along the Chukotka Mountains, sea breezes are coupled with upslope winds due to

the immediate uplift of terrain close to coastline. Similar process occurs in the eastern tip of the Brooks Range, where terrain and coastline are located close to each other.

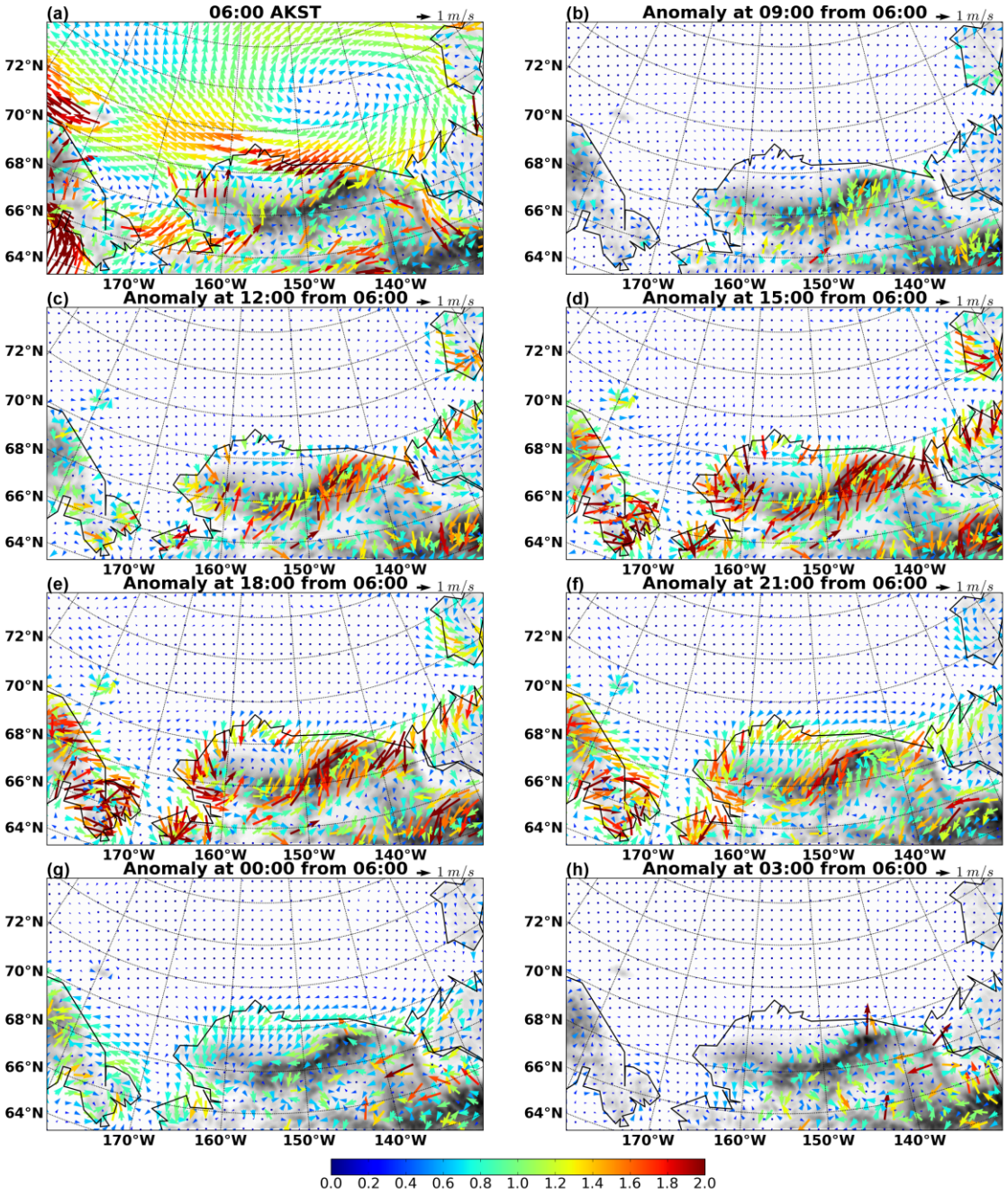

Figure 4.4. Climatological CBHAR surface winds (m s^{-1}) at 0600 AKST (a) and diurnal anomalies (m s^{-1}) from 0600 AKST at a 3-hourly interval (b-h) for July of 1979-2009.

4.3.2 Seasonal variation. With the 31-year CBHAR reanalysis, seasonal variation of surface winds is also analyzed by averaging the surface winds from 1979-2009 for different seasons (Figure 4.5). Overall, surface winds display strong seasonality in the study area. Surface wind speed is stronger in cold seasons than in warm seasons, mostly contributed by the seasonal variations of the location and intense of the Beaufort High and Aleutian Low.

Surface winds are strongest in winter with maximum wind speed about 4 m s^{-1} over the Chukchi Sea, the northwest Bering Sea, and south slope of the Chukotka Mountains (Figure 4.5a). Along the Brooks Range, local topography plays determinate role on surface winds, resulting intense downslope gravity drainage of cold air with speed of greater than 4 m s^{-1}. Surface wind maximum in the south slope of the Chukotka Mountains is probably attributed to both synoptic scale flow and downslope gravity drainage. In the area of the north slope of the Chukotka Mountains, the mountain barrier effect turns the northeasterly synoptic flow towards the mountain range to northwesterly winds that are parallel to the mountain range with enhanced surface wind speed about 4 m s^{-1}.

In spring and fall (Figure 4.5b,d), downslope winds still play role in affecting surface winds in the mountain areas, however, with reduced wind speed compared to winter. The downslope winds along the Brooks Range are characterized by wind speed of about 2 m s^{-1} in spring and 3 m s^{-1} in fall. The mountain barrier effect can be also identified in fall along the north slope of the Chukotka Mountains.

In summer (Figure 4.5c), surface winds are much weaker compared with the other seasons. Sea breezes are active along the Beaufort Sea coastal area, resulting averaged northeasterly winds of about 2 m s^{-1}.

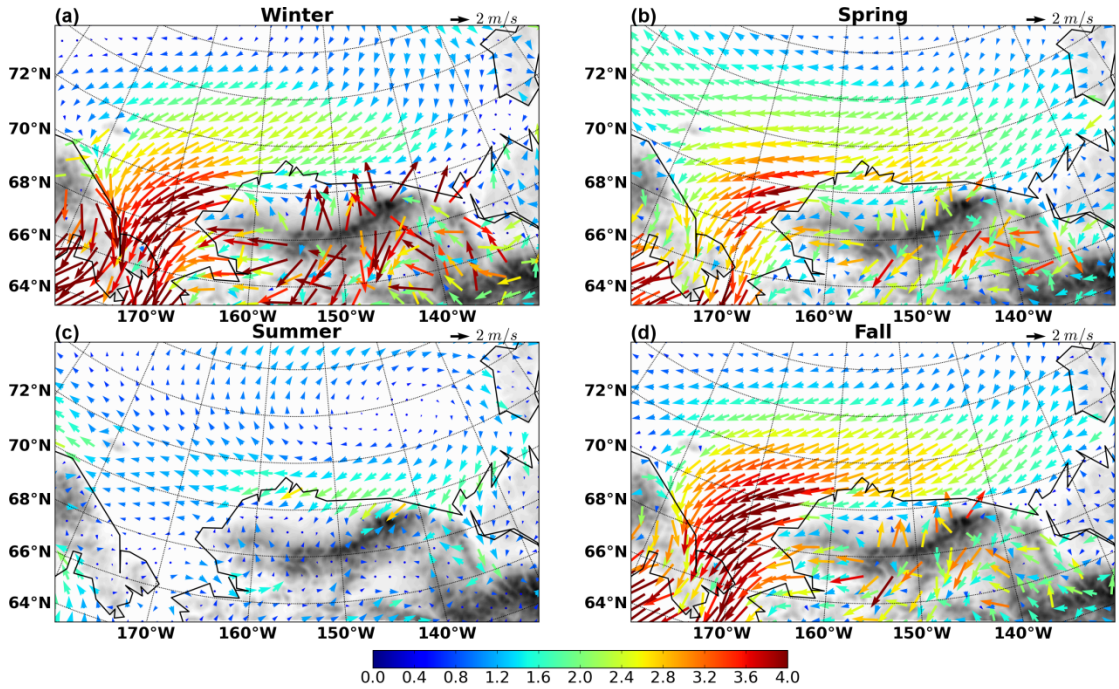

Figure 4.5. Climatological surface wind (m s^{-1}) in (a) winter (DJF), (b) spring (MAM), (c) summer (JJA), and (d) fall (SON) in CBHAR.

4.4 Sea Breezes

To examine the geographic dependence of the sea breeze winds, four particular shoreline-parallel sections are chosen as shown in Figure 4.3 (sections A-D). Section A represents an offshore location about 50 km away from the shoreline, where weak diurnal wind variation could be expected and most likely the sole impact on diurnal wind variation is from the sea breeze. Section B is located directly on the shoreline, experiencing the most pronounced diurnal variation in horizontal temperature contrast and probably a vigorous sea breeze. The surface winds at the inland section C are expected to show relatively weak impacts from sea breeze, due to its location about 50km away from both the shoreline. The further inland section D, meanwhile, is located about 100 km from the shoreline. By comparing the perpendicular

component of the surface winds relative to the shoreline at sections A, B, C, and D, the impacts of the sea breezes can thus be isolated.

As indicated by Figure 4.4, along the shoreline of sections A-D, offshore winds are present at the 0600 AKST, which are probably the combined results of anti-cyclonic flows in the north and cyclonic flows in the south. However the offshore winds can be weaken or turned to on-shore winds with enhanced solar heating during the day due to sea breeze (Figure 4.6). July averaged on/off-shore wind components along sections A-D display a clear diurnal variation. Along section A, representing the offshore location, surface winds are always toward the offshore direction, but weaker during the day and stronger during nighttime. Along section B, exactly at the shoreline location, the offshore wind reaches its maximum 0.5 m s^{-1} and starts to reduce the speed at around 0600 AKST. At around 1000 AKST, the surface wind turns its direction from offshore to onshore, representing the start of sea breeze. The sea breeze reaches its maximum at afternoon around 1500 AKST with a speed ~1.25 m s^{-1}. The on/offshore wind along section B varies in a range of about 1.75 m s^{-1}, which is about 0.5–0.75 m s^{-1} at the other locations. This implies that the diurnal variation is most vigorous at the shoreline. Along the inland sections C and D, the diurnal variations are very similar, the offshore winds are reduced to minimum and turn to onshore direction around 2200 AKST, which lags behind the maximum onshore wind at the shoreline by about 6 hours. The lag is very likely caused by the propagation of sea breeze from the shoreline to inland.

The vertical structure of the sea breeze can be revealed by examining the vertical motion and on/offshore wind component along the selected cross-section profiles (P1-P3 in Figure 4.3). Given that thermodynamically forced sea breezes are most active in July, the climatological diurnal variations of wind in July are examined, as displayed along the vertical profiles P1-P3 in

Figure 4.3. The diurnal evolution of the sea breeze circulation at different geography locations is depicted in Figures 4.7-9 for profile P2 along the Chukchi Sea coast, P3 along the eastern Beaufort Sea coast, and P1 along the Chukotka Mountain. These three profiles were chosen to represent different scenarios where sea breeze solely plays roles or both sea breeze and upslope wind are coupled together. The sea breeze and upslope circulation is isolated by subtracting the wind field at 0600 profile local time from the wind field at each hour of the day.

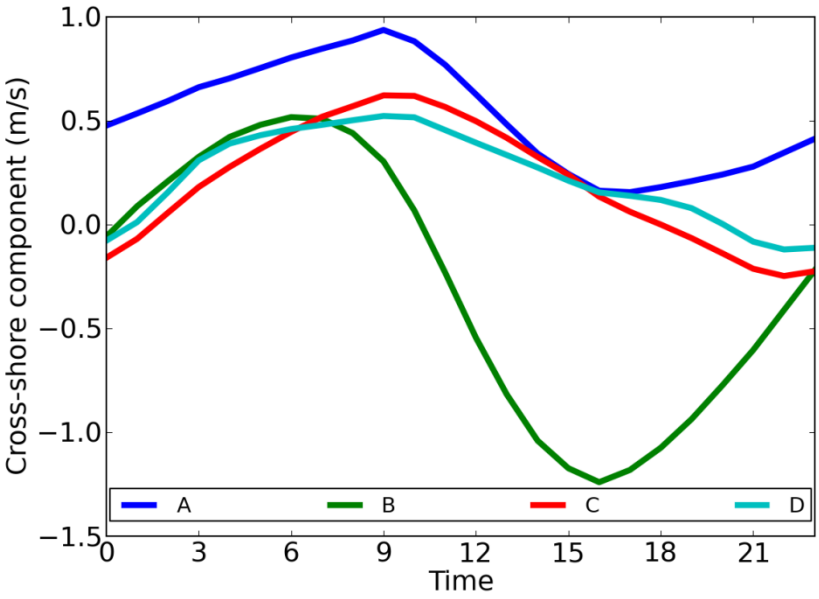

Figure 4.6. Climatological diurnal variation of the on/offshore surface wind components (m s^{-1}) in July along sections A, B, C, and D as shown in Figure 4.3. Positive values represent offshore-directed wind, and negative values onshore wind. Times are given in AKST.

Diurnal evolution of sea breeze circulation (Figures 4.7) shows that as land surface warms up, upward motion is gradually developed from inland, and at noon, sea breeze circulation is initially formed, with onshore winds across an expanse of less than 100 km in terms of wind speed anomalies greater than 1 m s^{-1}. Over the area where maximum upward

motion occurs, the upper-air motion is oriented toward the offshore direction at about 0.5-1 km above ground, and the downward motion develops offshore within 50 km of the shoreline. The sea breeze circulation is strengthened further in the following hours due to continuing warming over land. It should be noted that the offshore surface temperatures don't change much throughout the entire diurnal cycle. So the thermal contrast between land and sea enhances with land warming up and weakens with land cooling down, but always land surface is warmer than the sea surface during the entire diurnal cycle. The strongest sea breeze circulation occurs in the afternoon at about 1500 local profile time, with maximum onshore wind anomalies ~2 m s^{-1}, located around the shoreline near the surface, and a maximum return flow of about 0.5 ~ 1 m s^{-1}, located about 1 km above ground. After 1500 the sea breeze circulation gradually weakens in the next 12 hours.

Comparison of the development of onshore winds along profiles P2 (Figure 4.7), P3 (Figure 4.8) and P1 (Figure 4.9) can reveal how the topography plays roles in terms of affecting the intense and horizontal extent of onshore winds near surface, the intense and location of upward motion, and the location and intense of returning flow at upper level. In order to characterize the horizontal extension of sea breeze, the areas with wind speed anomalies greater than 1 m s^{-1} are identified as significant sea breezes. Along profile P2 over the Chukchi Sea coast where the terrain is flat, significant onshore winds can penetrate inland by about 90-100 km from shoreline during afternoon hours 1500-1800 UTC, meanwhile the offshore extent of significant onshore winds is around 50 km from shoreline (Figure 4.7c-d). As a comparison, the maximum extent of onshore winds can reach about 70 km inland from shoreline along profiles P3 and P1, where mountain slopes are present (Figures 4.8-9). The Chukotka Mountains and the eastern Brooks Range reduce the horizontal penetration of onshore winds toward inland by about

20-30 km, due to mountain blocking. On the other hand, when the mountain slop is very steep (profile P3), the offshore extent of onshore winds is also reduced by about 20-30 km (Figure 4.8).

The intense of upward motion and the location of strong onshore wind center also vary when different mountain slopes are present. During summer, mountain slope receives more heat than ambient air, which in turn produces surface temperature gradients and generates upslope winds. As a result, the slope located near the shoreline enhances the onshore winds by coupling sea breeze and upslope wind together. Enhanced onshore winds plus mountain dynamic uplifting further cause strong upward motion along the profiles P3 and P1 (Figures 4.8-9). When the slope is flat (profile P2), the location of the strongest onshore winds is centered at the shoreline (Figure 4.7). When the slope increases, the center of strong onshore winds and the entire circulation move towards the slope (Figures 4.8-9).

As the intense of upward motion and the location of entire breeze circulation vary with mountain slope, the intense and location of returning flow at the upper level vary in response. When the slope is flat as in profile P2, the returning flow is located at ~1 km above the ground near shoreline with maximum wind speed anomalies around 0.7 m s^{-1} (Figure 4.7). When the sea breeze circulation move towards inland as the slope increases, stronger returning flows occur, with maximum wind speed anomalies greater than 1 m s^{-1} along profiles P3 and P1 (Figure 4.8-9). Following the maximum upward motion, the horizontal location of maximum returning flow moves to about 50 km inland along P3, and about 30 km along P1, instead of within 10 km from the shoreline along P2.

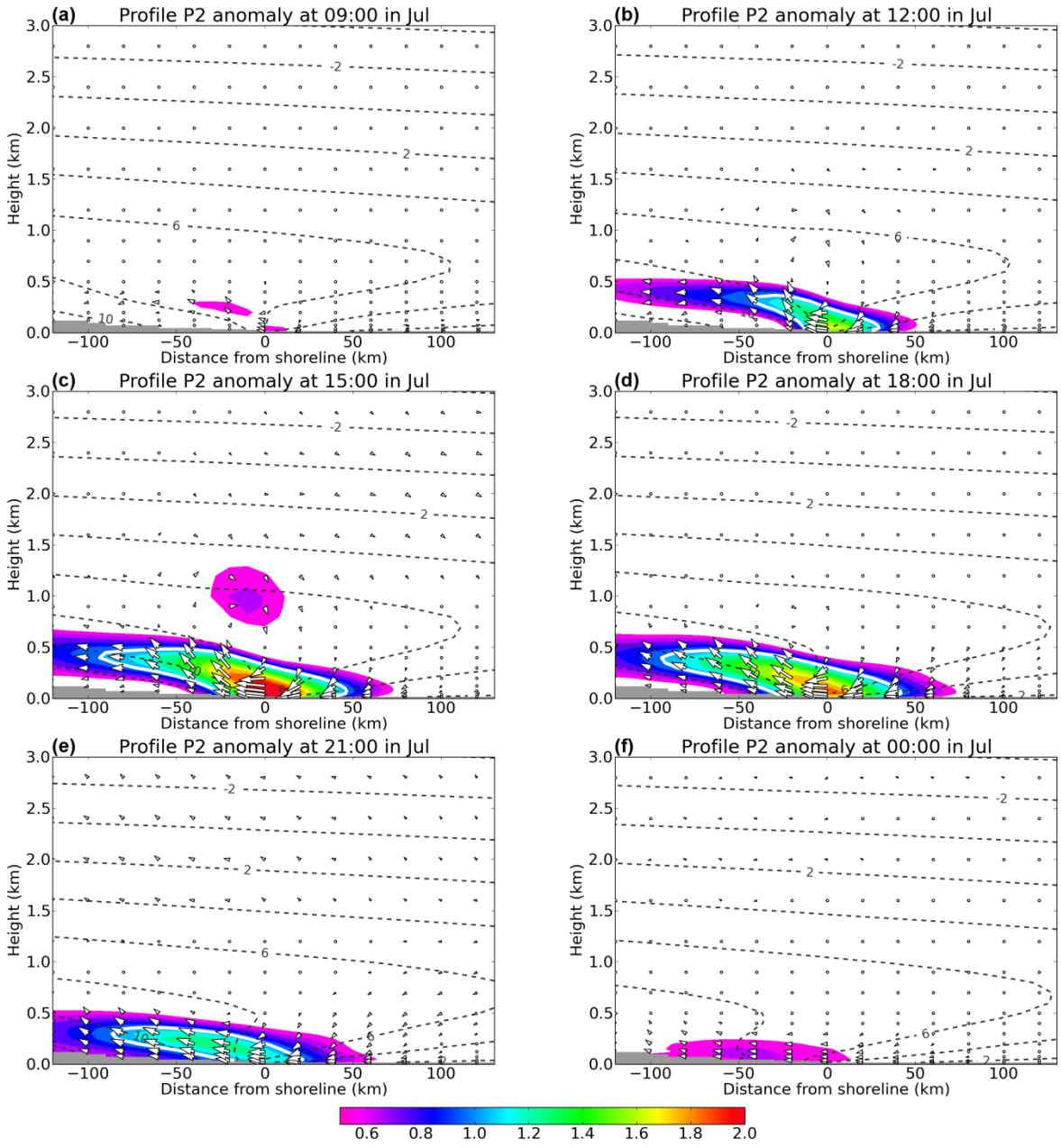

Figure 4.7. Wind anomalies from 0600 local time in July at 0900(a), 1200(b), 1500(c), 1800(d), 2100(e), and 0000 (f) along the vertical cross-section profile P2. Wind vectors include both the horizontal wind component, oriented perpendicular to the shoreline, and the vertical component. Wind speed along profile (m s^{-1}) is indicated by colors. Soild contours in white present wind speed anomaly of 1.0 m s^{-1}. Dashed contours are for temperature (°C). The shoreline is located at 0 km.

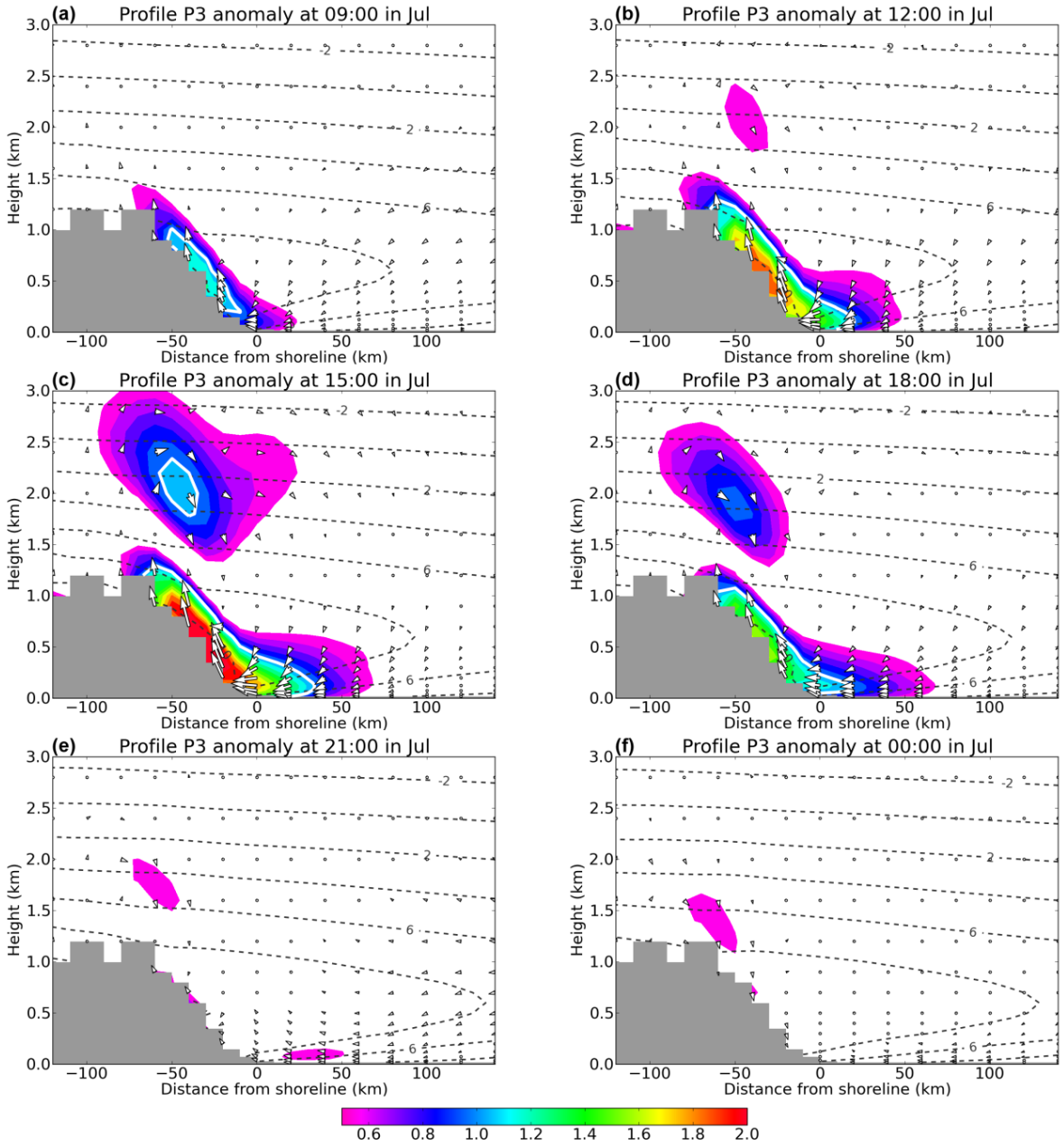

Figure 4.8. Wind anomalies from 0600 local time in July at 0900(a), 1200(b), 1500(c), 1800(d), 2100(e), and 0000(f) along the vertical cross-section profile P3. Wind vectors include both the horizontal wind component, oriented perpendicular to the shoreline, and the vertical component. Wind speed along profile (m s^{-1}) is indicated by colors. Solid contours in white present wind speed anomaly of 1.0 m s^{-1}. Dashed contours are fore temperature (°C). The shoreline is located at 0 km.

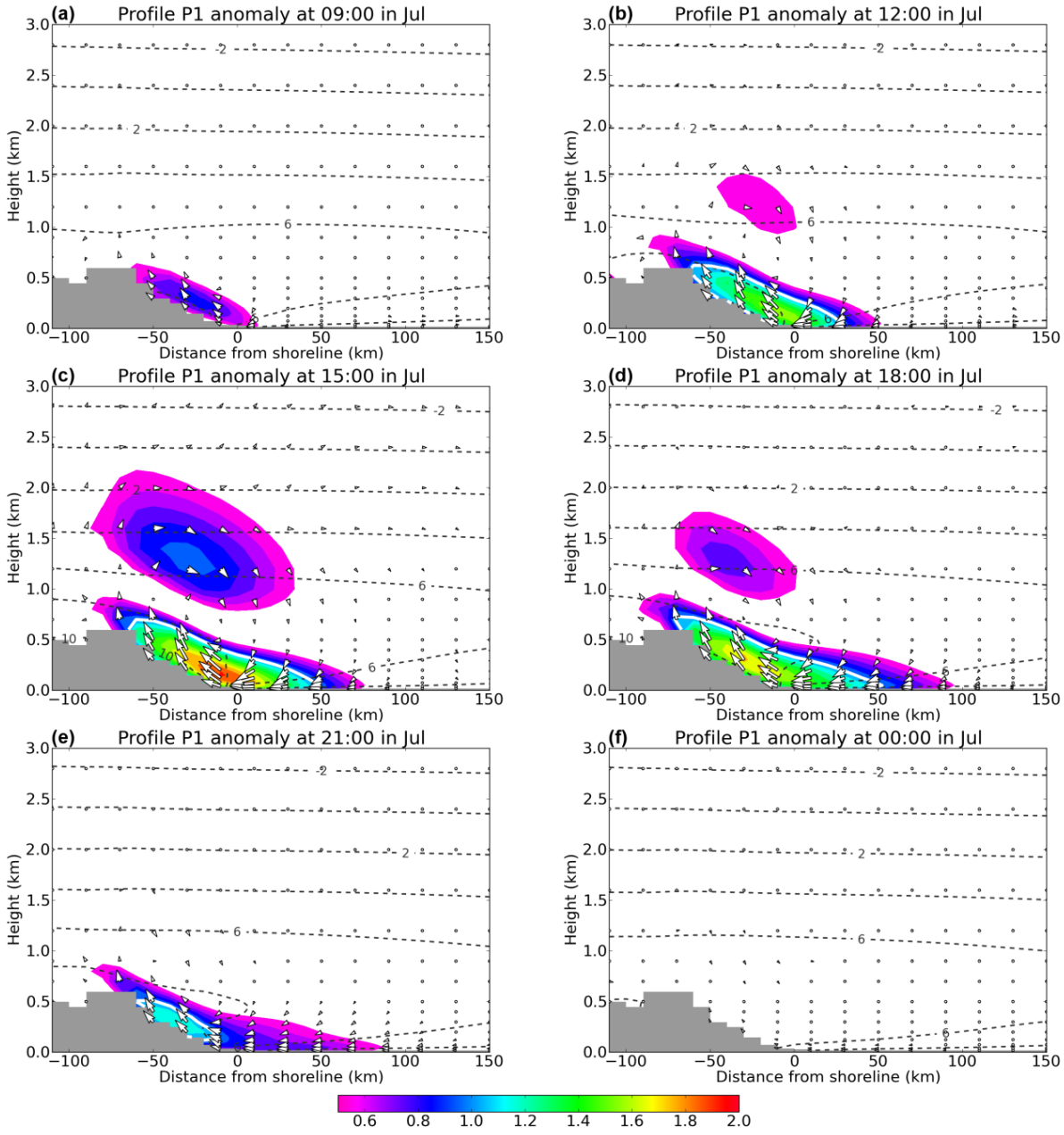

Figure 4.9. Wind anomalies from 0600 local time in July at 0900(a), 1200(b), 1500(c), 1800(d), 2100(d), and 0000(f) along the vertical cross-section profile P1. Wind vectors include both the horizontal wind component, oriented perpendicular to the shoreline, and the vertical component. Wind speed along profile (m s^{-1}) is indicated by colors. Solid contours in white present wind speed anomaly of 1.0 m s^{-1}. Dashed contours are for temperature (°C). The shoreline is located at 0 km.

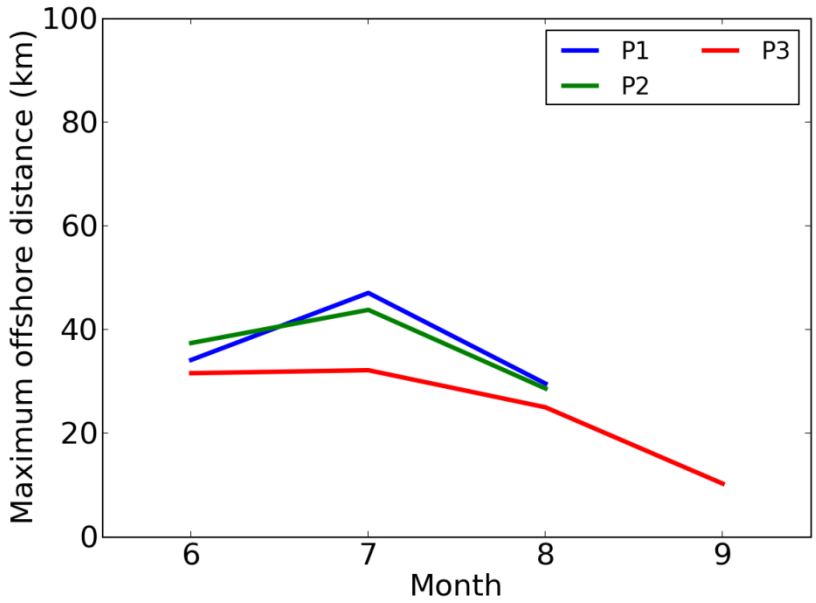

Figure 4.10. Monthly offshore extension (km) of the sea breeze along profiles P1-P3. The extension is defined by climatology diurnal variation of the cross-shore wind component greater than 1 m s^{-1}.

The horizontal spatial extent of sea breeze circulation is impacted by the mountain slope and also varies with season. For the offshore extent, the distance out to which sea breezes may affect offshore is measured through the use of a criterion specifying that the climatological diurnal wind variation of the cross-shore wind component be greater than 1 m s^{-1}; exceeding this threshold was defined to indicate the presence of a sea breeze. The results show that the largest distance that the sea breeze extends offshore appears over the Chukchi Sea west of Alaska and north of the Chukotka Mountains (P1 and P2 in Figure 4.10). In the eastern Beaufort Sea, the circulation is more active in vertical direction, which tends to reduce the stability of atmosphere at lower level and hence limits the horizontal extent. There is seasonal dependence of the sea breeze, which emerges in June with a spatial extent out to 30–40 km offshore. Along the three

profiles, sea breezes affect the most extensive areas in July. The affected distance decreases to about 30 km in August and further to about 10 km in September.

4.5 Up/Downslope Winds

While the dense cold-air flow over the Antarctic ice sheet has been extensively studied (e.g., Parish and Cassano 2003), there have been few such studies on the Arctic Slope. Following the method used in section 3.4, the vertical structure of the up/downslope winds is analyzed by examining the vertical motion and horizontal wind component along the selected cross-section profile.

The mountains' thermodynamic effects leave different footprints on the surface winds from month to month. Over the mountain profile (P4 in Figure 4.3) at the eastern Brooks Range, seasonal variation of the mountains' thermodynamic effects is clearly shown by the strength of drainage flows (Figure 4.11). The gravity drainage of cold air starts at the mountain top in September, and gradually increases the intensity and extent downward to the slope in the following cold months as the surface temperature decreases. Strong cooling starts at the mountain top and gradually plunges down to the slope, resulting in the accumulation of dense cold air along the mountain surface. The strongest downslope wind occurs during the coldest months of the year, from November to February, with a downslope wind component greater than 2 m s^{-1}. During this cold season, there is no diurnal variation of surface wind due to the lack of solar irradiance. The downslope winds can be observed until in April with significantly reduced spatial extents. In May and August, the monthly averaged wind profiles display very weak wind near surface, due to the cancellation of upslope winds and downslope winds caused by diurnal variation of incoming solar radiation. In June and July, the monthly averaged wind profiles show weak upslope winds.

The spatial extents of downslope winds also vary with season. In the starting month of September, the downslope winds can be observed at the top of mountains (Figure 4.11i) within limited area of about 50 km. The drainage flow pushes downward along the slope and occupies the entire slope from November to February (Figure 4.11k,l,a,b). After February, the downslope winds shrink toward the top of mountains again (Figure 4.11c,d). Vertically, the gravity drainage of cold air is trapped in a thin layer less than 300 meters near surface, due to the fact that extremely cold surface increases the stability of atmosphere, usually accompanied with inversion in the Arctic area, inhibiting vertical convection.

During the cold months, it's also noticed that the downslope winds are missing over the Chukotka Mountains (not shown), and south slope of the eastern Brooks Range (Figure 4.11), which is due to the approaching background flow in the areas. When background flow approaches mountains, it is the mountain barrier effect that plays more important role by redirecting and enhancing the surface wind. This is will be discussed in section 3.6.

In the summer months, the upslope winds are dominating. Along the mountain profile P4 over the eastern Brooks Range, the wind profile shows a well-defined mountain slope circulation varying with the hours of day (Figure 4.12). The upslope winds start to build up around 0900 local time. From noon to late afternoon, the upslope wind anomalies are greater than 1 m s^{-1} along the entire slope. The returning flow is located at about 1000 meters above the ground over the mountain top with a maximum wind anomalies great than 1 m s^{-1} at 1500 profile local time. The upslope winds continue until 2100 local time.

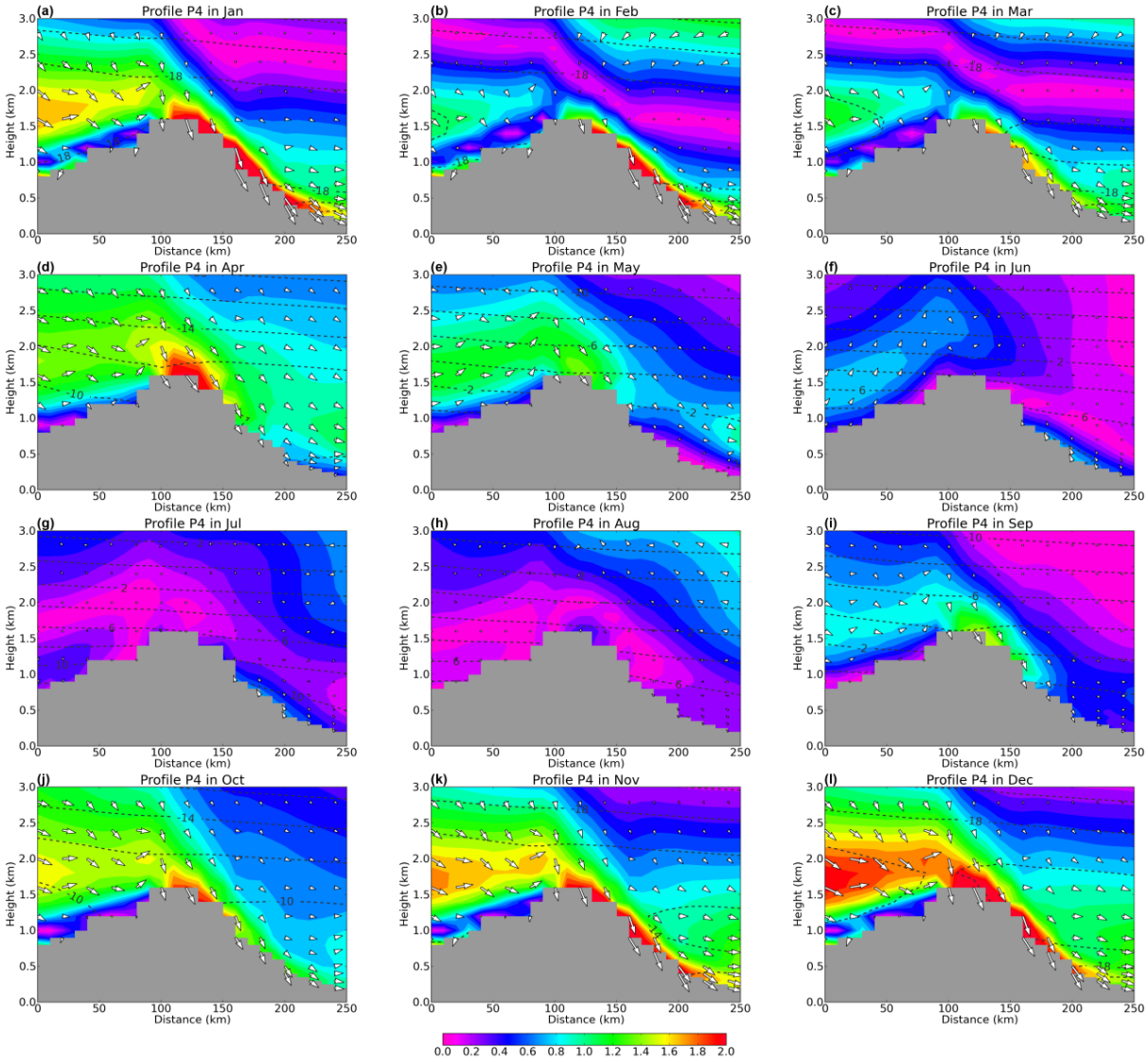

Figure 4.11. Monthly mean wind profiles along the profile P4 (as shown in Figure 4.3). Wind vectors compose of a horizontal component oriented parallel to the profile and the vertical component. Wind speeds along profile (m s^{-1}) are indicated by colors. Dashed contours are temperature (°C).

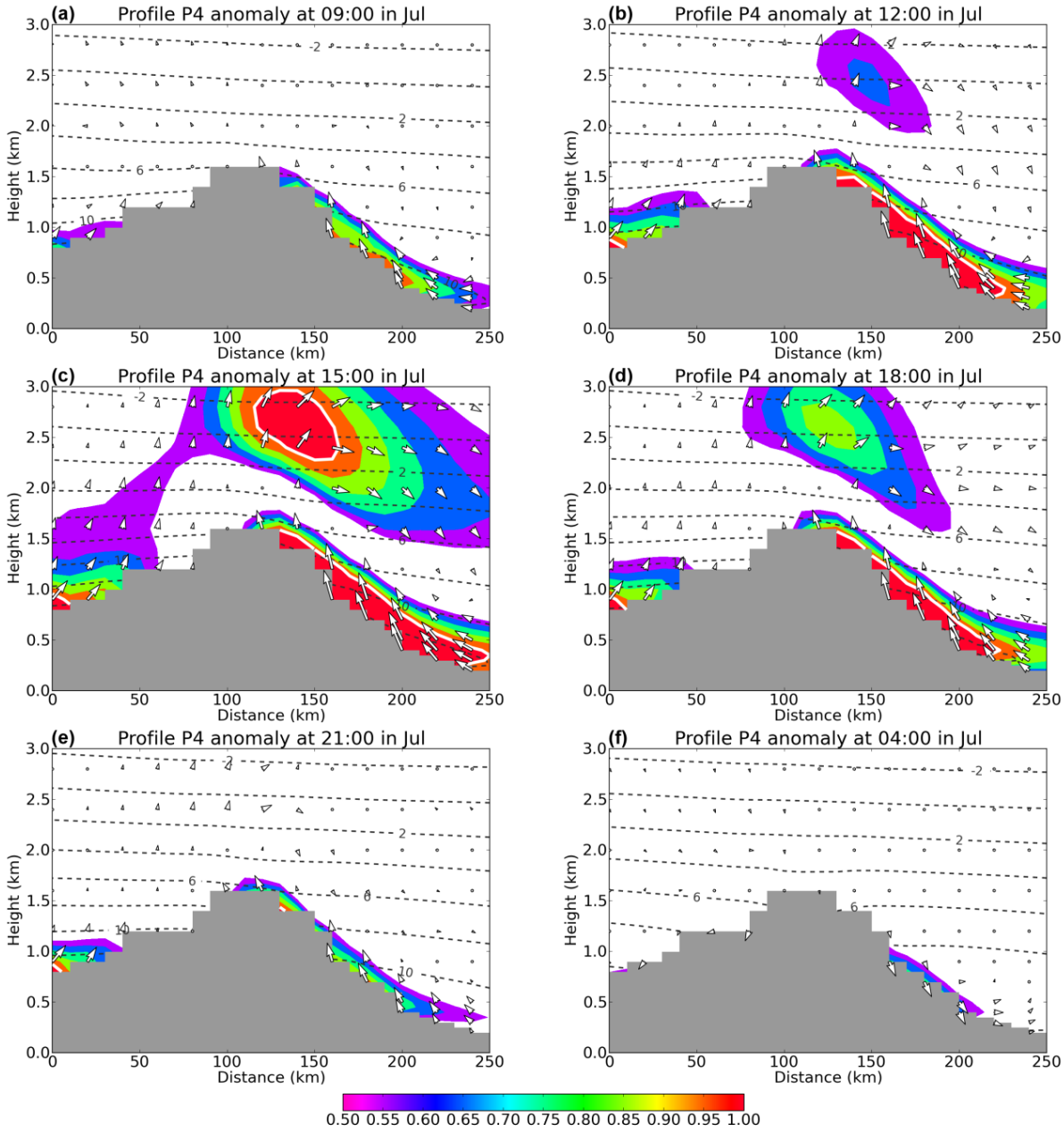

Figure 4.12. Wind anomalies from 0600 local time in July at 0900(a), 1200(b), 1500(c), 1800(d), 2100(e), and 0000(f) along the vertical cross-section profile P4. Wind vectors include both the horizontal wind component, oriented perpendicular to the shoreline, and the vertical component. Wind speed along profile (m s^{-1}) is indicated by colors. Solid contours in white present wind speed anomaly of 1.0 m s^{-1}. Dashed contours are for temperature (°C).

4.6 Mountain Barrier Effect

Mountain barrier effect is another mesoscale process through which topography can affect the surface wind fields in the study area (Schwerdtfeger 1974; Kozo 1980). When air flow approaches a mountain, the air is forced to either ascend over the mountain or be blocked, depending on the properties of both the air layer and the topography as measured by a series of parameters, including the horizontal scale and slope of the mountain, the direction and speed of the large-scale flow, and the stability of the atmosphere, among others. When the Froude number is low ($U/NH<1$; where U is the speed of the general flow, N is the Brunt–Väisälä frequency, and H is the mountain height), the kinetic energy of the low-level flow is insufficient for the air to pass completely over the mountain. The flow is thus blocked and decelerates as it approaches the barrier. Decelerated flow results in a decreased Coriolis force, breaking the geostrophic balance of the large-scale wind. The flow is thus deflected to the left and a mass of air accumulates near the base of the mountain, which in so doing generates a mesoscale pressure ridge. Eventually, a new balance between the large-scale pressure gradient, mesoscale pressure gradient, Coriolis force, and friction is reached. Accordingly, a low-level wind maximum (mountain barrier jet) is formed parallel to the mountain barrier. In the study domain, the occurrence of low Froude number flow is common, due to the orientation of the mountain ranges and the stable low-level atmosphere. Mountain barrier effect is therefore expected to be one of the important mesocale processes affecting the surface wind field.

Seasonal variation of surface winds over the 31-year period in CBHAR (Figure 4.5) can help to gain an overall understanding of the occurrence of mountain barrier effect across the entire study domain. A noticeable strong wind occurs over the Chukchi Sea during the cold months, which is attributed to the mountain barrier effect. Under the influence of intense

Beaufort High centered over the northern Chukchi Sea, strong northeasterly synoptic-scale winds blow toward the Chukotka Mountains, which are then deflected to flow parallel to the mountain range with enhanced speeds (barrier jet) due to the mountain barrier effect. The similar deflected surface winds also occur in the south slope of the eastern Brooks Range. Thus the vertical wind structures along profile P1 at the Chukotka Mountains (Figure 4.13) and profile P4 at the eastern Brooks Range (Figure 4.14) are analyzed for each month of year. Monthly averaged wind vectors along the profile and wind speed perpendicular to the profile demonstrate that a flow toward the mountains during the cold months from January through April and from September through December, favors the occurrence of barrier jet, strong winds to the left of the flow toward the mountain occur. During the warm season (June–August), there is no such strong wind along the mountain ranges (f-h in Figures 4.13-14).

The mountain barrier jets along the Chukotka Mountains are strongest in December and January, when the Beaufort High is strong and located over the northern Chukchi Sea, causing strong northeasterly winds directly blow to the Chukotka Mountains. The jet's maximum winds are about 6 m s^{-1} in the area 40 km inland from the shoreline, where the topography begins to rise dramatically. The maximum winds associated with the barrier jet also extend offshore to a fairly large distance. At the offshore location 50 km away from the shoreline, the wind components parallel to the mountain range are greater than 4 m s^{-1} in January and December (Figure 4.13a,l). From January to April, the jets become weaker, winds decreasing from around 6 m s^{-1} to 3.5 m s^{-1}, and reducing its extent to within 50 km of both sides of the shoreline. From September to December, the barrier jets recover its strength, following almost a reversal of the process that occurs from January to April.

Barrier jets over the south slope of eastern Brooks Range are relatively strong from November to March with wind speed around 5–6 m s^{-1}, which is slightly weaker than the barrier jets along the Chukotka Mountains. Obviously that is due to relatively weaker winds blowing toward the south slope of Brooks Range comparing that blowing toward the Chukotka Mountains.

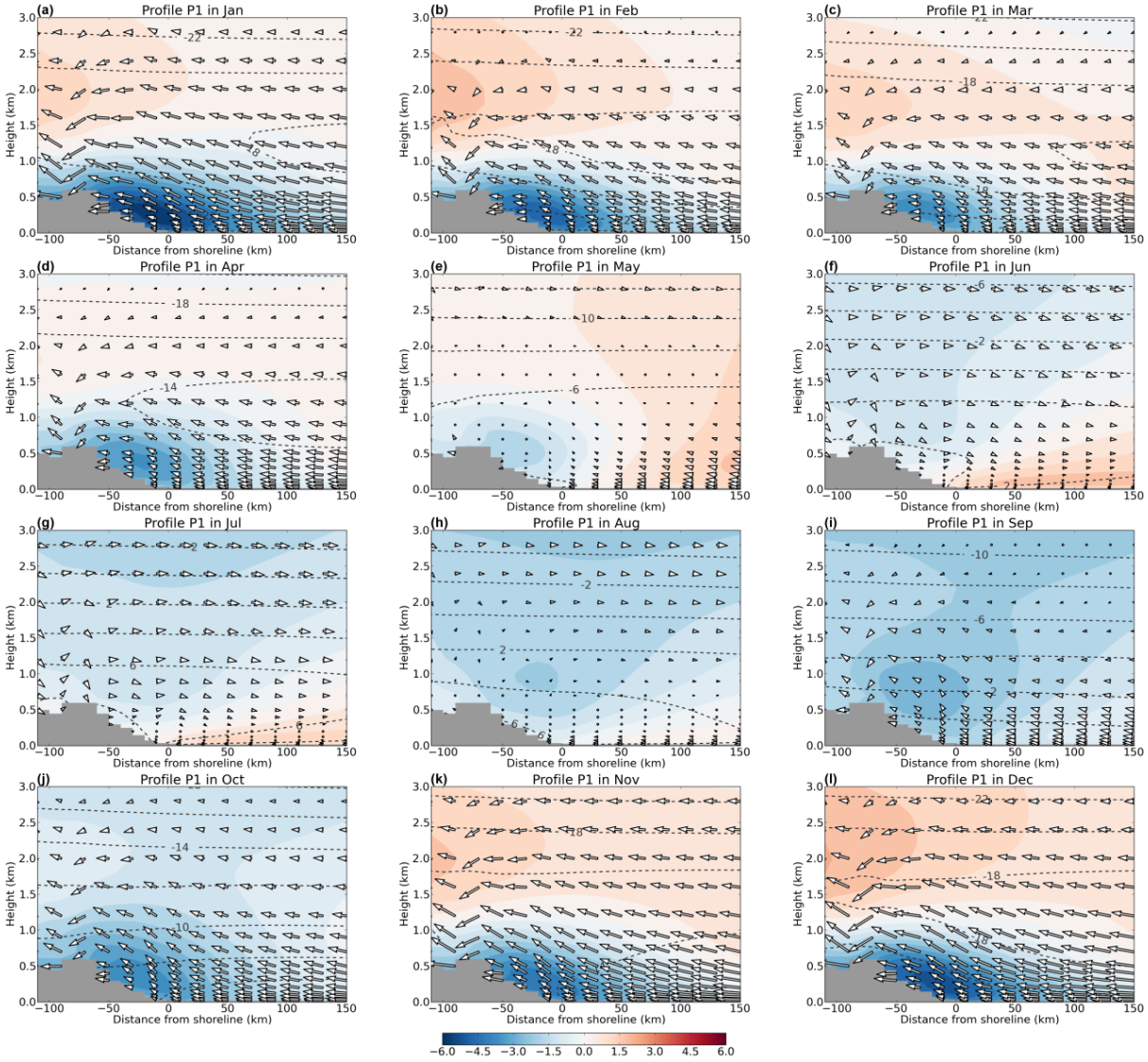

Figure 4.13. Monthly mean wind vectors (m s^{-1}) along profile P1 (as shown in Figure 4.3) and wind speed (m s^{-1}) perpendicular to the profile (negative wind speeds in blue represent flow toward the reader and positive in red away from the reader). The shoreline is located at 0 km.

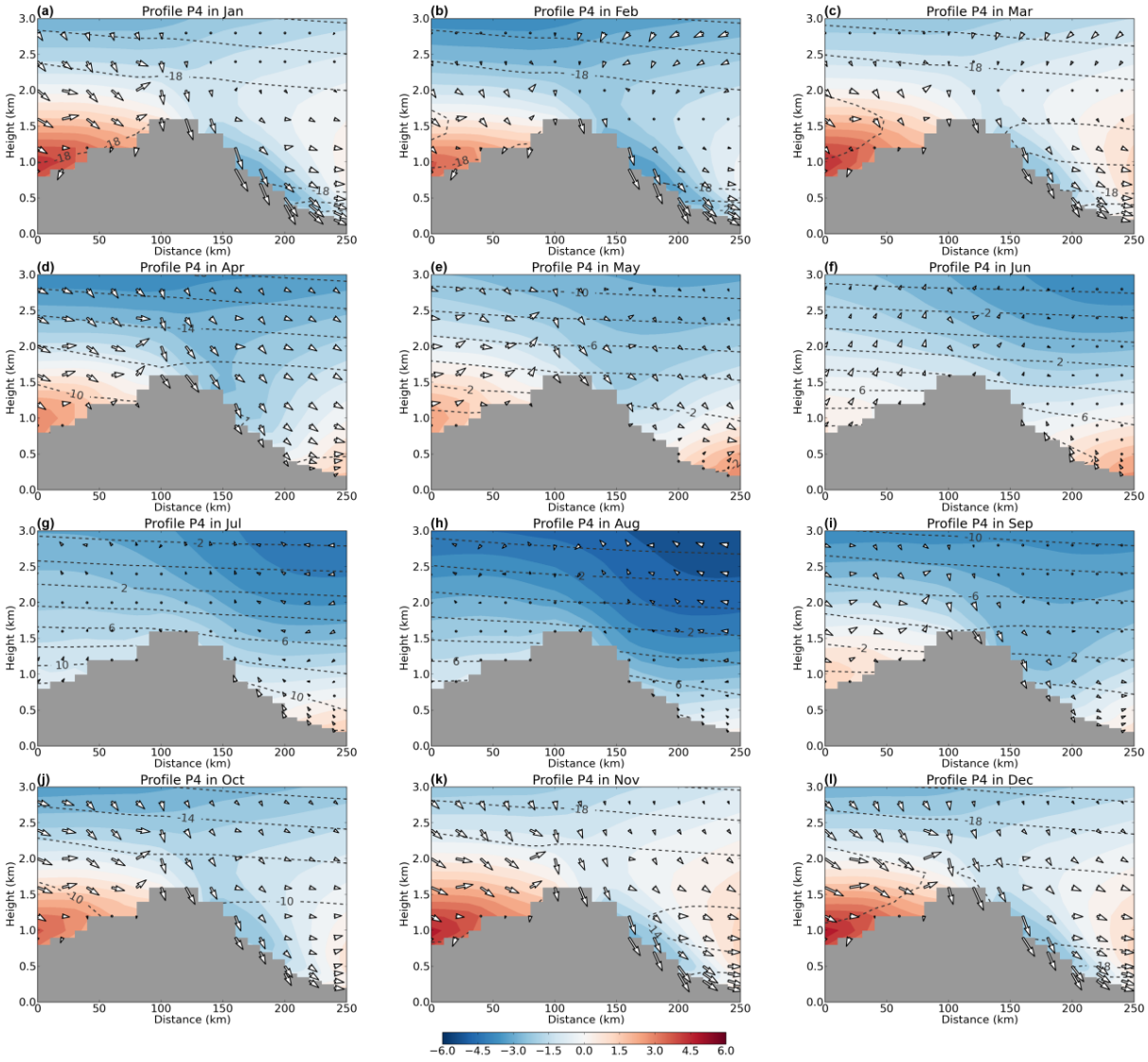

Figure 4.14. Monthly mean wind vectors (m s^{-1}) along profile P4 (as shown in Figure 4.3) and wind speed (m s^{-1}) perpendicular to the profile (negative wind speeds in blue represent flow toward the reader and positive in red away from the reader).

Comparisons between observations and CBHAR in capturing the mountain barrier effect are also made to demonstrate how CBHAR captures the mountain barrier effect process in the study area. For example, the observed climatological distribution of wind speed and direction at station Mys Shmidta, located on the shoreline near the Chukotka Mountain, shows that the

surface is solely dominated by strong northwesterly winds (barrier jets) in January (Figure 4.15a), with a maximum wind speed of greater than 7 m s^{-1}. CBHAR agrees very well with the observations (Figure 4.15b). In July, the dominant surface winds flow from the east-southeast, with far fewer occurrences of high wind-speed events (Figure 4.15c,d).

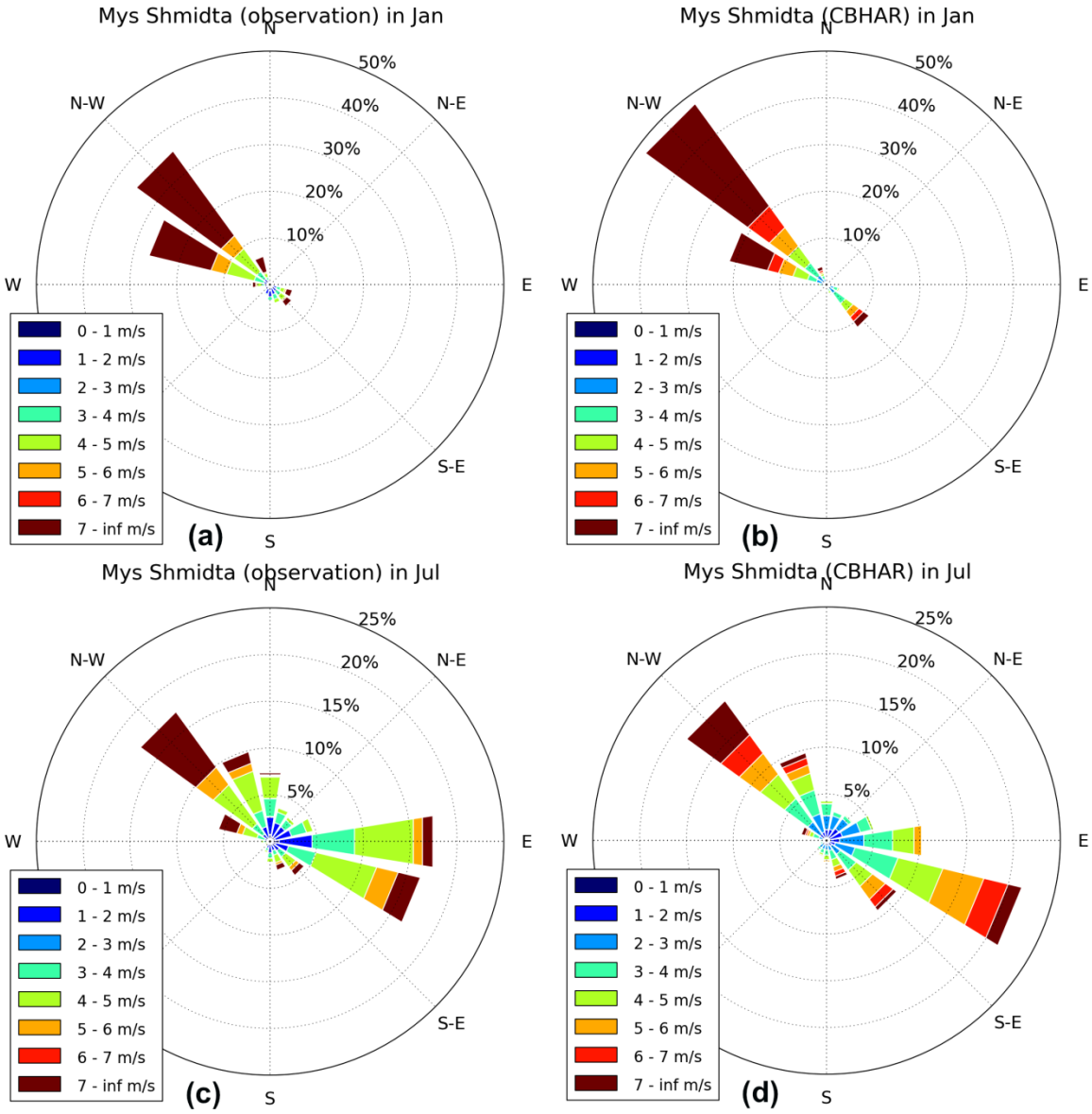

Figure 4.15. Wind rose comparisons at station Mys Shmidta between observatons (left) and CBHAR (right) for January (top) and July (bottom).

Over the north slope of the Brooks Range, the large-scale flow has only a weak component oriented perpendicular to the mountain range; thus, the climatological vertical wind distribution does not show the similar barrier jets (not shown), indicating the absence of the mountain barrier process and suggesting few impacts of mountain barrier effect on the surface wind field in the area in terms of long-term climatology. Despite this, the mountain barrier process may still occasionally occur at particular times under favorable synoptic conditions and have an impact on the surface winds.

4.7 Mesoscale Wind Field Variability

The Chukchi-Beaufort Sea region is currently undergoing significant environmental changes, including the fastest rate of decline and maximum observed interannual variance of sea ice anywhere in the Arctic (Stroeve et al. 2007; Comiso et al. 2008), as well as increased 10-m wind speeds over recent decades as the sea ice retreats (Stegall and Zhang 2012). As discussed in previous sections, both prevailing synoptic weather patterns and prominent underlying geographic features play roles in determining the surface wind climate (Schwerdtfeger 1974; Kozo 1980; Moor and Pickart 2012; Zhang et al. 2013). The dominant synoptic-scale weather patterns in the area provide background wind flow patterns, which are further modulated by local geographic features to produce mesoscale wind fields. It's thus possible that mesocale circulation such as sea breezes and mountain barrier effect are subject to variation and changes in response to adjustment of large-scale atmosphere circulation in our study domain.

4.7.1 Storm activity and sea breezes. In the Beaufort-Chukchi Seas region, storms are active during entire year. Storm activity plays important role in determining surface winds, transferring moisture and energy, and altering radiative energy budgets. The development of sea breezes is thus expected to be affected by storm activity through altering background flow and

surface thermal contrast. Therefore, the relation between storm activity and sea breezes is explored in this section. Since sea breezes in the study area are most active in July, this discussion focuses on July only.

The monthly storm activity is represented by an integrated parameter Cyclone Activity Index (CAI) defined by Zhang et al (2004). In order to represent the monthly mean strength of sea breeze circulation, a sea breeze index is designed for use in the storm-sea breeze relation study. Along the selected cross-section (P1 in Figure 4.3 is selected to avoid mountain impact), July averaged hourly wind profiles are calculated first, then the difference of cross-shore wind component at near surface between 1500 and 0600 profile local time is used to represent the strength of a well-developed sea breeze (Equation 1). The reason of choosing 1500 and 0600 profile local time is because these times represent the maximum and minimum strength of the breeze, as we discussed in previous sections. In order to filter the potential noises caused by some finer scale processes, when calculating the difference, the averaged value of cross-shore wind components over a shallow near surface layer (below 40 meters) is used.

$$I_{sea\ breeze} = \overline{V_{15:00}} - \overline{V_{06:00}}\ , \qquad (1)$$

where represents the cross-shore wind component; the subscript represents time in profile local time; overlines represents averaged wind in a given month July of a specific year.

The results show that sea breeze along profile P2 is negatively correlated with storm activity in July (Figure 4.16). The correlation coefficient between monthly sea breeze index in July and CAI is -0.38, passing 95% significance test. The relation implies that strong storm activity can inhibit the development of sea breezes in the study area. The temperature contrast between land and ocean plays deterministic role in generating the sea breeze circulation. The

temperature over land can be decreased by storm activity through reduced incoming solar radiation due to clouds accompanied with the storm. In addition, the strong winds associated with storms are able to reduce the stability of atmosphere at lower level and enhance horizontal advection, which can further weaken temperature contrast between land and ocean. A strong storm activity therefore results in weak sea breezes along the Beaufort coast.

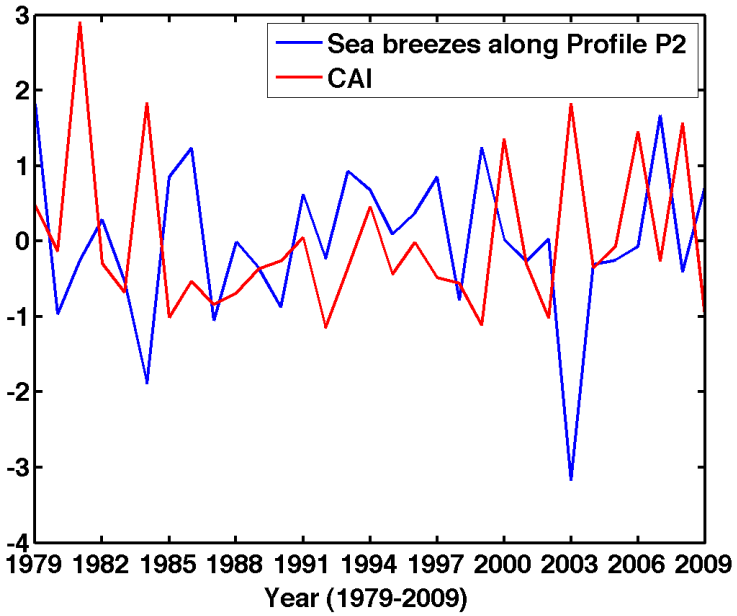

Figure 4.16. Normalized annual sea breeze index along profile P2 and storm CAI in July from 1979 to 2009.

4.7.2 Beaufort High and mountain barrier effect. In the Beaufort-Chukchi Seas region, the mountain barrier effect is most significant over the north slope of Chukotka Mountains in winter, where the large-scale northeasterly winds caused by the Beaufort High blow towards the mountain directly. The intense and location of the Beaufort High thus play roles in determining the intense of mountain barrier effect.

Composite analysis on sea level pressure (SLP) is conducted in order to study how the Beaufort High affects the mountain barrier jets along the north slope of Chukotka Mountains and in the Chukchi Sea for January when the barrier effect is relatively strong. The intense of mountain barrier effect is defined as the intensity of wind components along the mountain range over the north slope of Chukotka Mountains. In total, five years of strong mountain barrier effect are selected, including 1981, 1985, 1986, 1990, and 2001, as well as five years of weak mountain barrier effect, including 1979, 1988, 1996, 2004, and 2007. The composite SLP shows significant difference in years of strong/weak mountain barrier effects (Figure 4.17). In the years of weak mountain barrier effect, the Beaufort High is stronger in intense and moves towards south, resulting easterly winds toward the mountain slope. The change of wind direction contributes to less significance of mountain barrier effect. In the years of strong mountain barrier effect, the Beaufort High is located over the north Beaufort Sea. The northeasterly winds over the slope are enhanced by increased pressure gradient, which is mainly contributed by significantly reduced sea level pressure over the Chukchi Sea and the Beaufort Sea, as well as the interior of Alaska. The enhanced wind component toward mountain slope is also responsible for enhancement of mountain barrier effect.

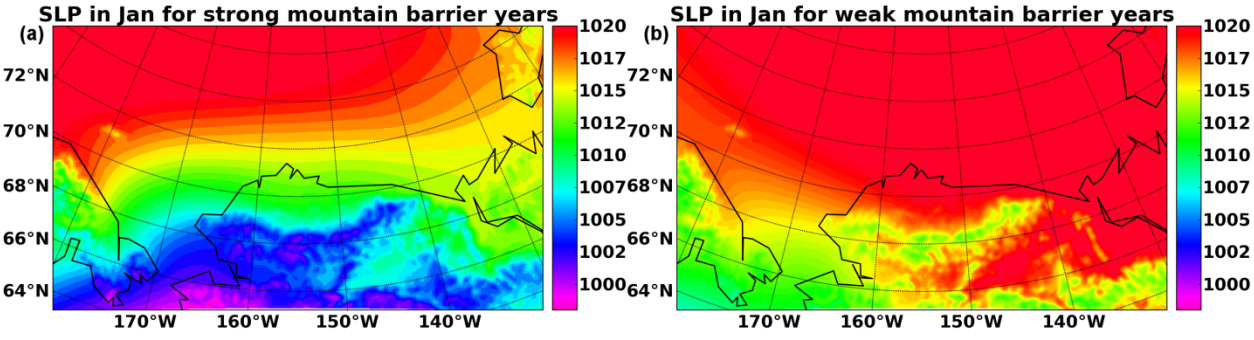

Figure 4.17. Composite analysis of sea level pressure associated with years of strong mountain barrier effect and weak mountain barrier effect in January over the Chukotka Mountains.

4.8 Summary

The CBHAR is utilized to detail mesoscale climatology and changes of surface wind field in the Chukchi-Beaufort Seas. In the data domain, a series of cross-shoreline/mountain profiles are chosen and the wind fields averaged across these profiles are analyzed for quantitatively understanding mesoscale climatology of surface winds, including sea breezes, up/downslope winds, mountain barrier effect, as well as mesoscale wind field variability.

The climatology of surface winds confirms that surface winds display strong seasonality in the study area, characterized by stronger surface wind speed in cold seasons than in warm seasons. It is mostly contributed by the seasonal variations of the location and intense of the Beaufort High and Aleutian Low. In summer, it is also noticed that the diurnal variations of surface winds mainly occur over the mountainous and coastal areas, revealing that sea breezes and up/downslope winds are the major contributors to the diurnal variation of surface winds in the area.

In order to quantitatively understand the vertical structure and diurnal variation of sea breezes, the climatology vertical wind profiles are calculated along three interested cross-sections that are located crossing the Chukotka Mountains, the western Beaufort Sea coast, and the eastern Beaufort Sea coast. The results show that onshore wind component of sea breezes displays a clear diurnal variation in June, July and August. The strongest onshore winds occur right at the shoreline and reach its maximum at afternoon around 1500 local time. The maximum onshore wind anomalies ~2 m s^{-1} are located at the shoreline, and the maximum returning flow anomalies 0.5~1 m s^{-1} are located about 1 km above ground. Terrains near the shoreline play important roles in affecting sea breeze circulation by enhancing the upward motion and moving the center of strong onshore winds and the entire circulation toward the slope. Over a relatively

flat surface without interacting with mountain slope, sea breeze circulation can extend ~100 km onshore and 50 km offshore. When interacting with mountain slope, the maximum extent of onshore winds can be reduced by 20–30 km. When the mountain slope is very steep, the offshore extent of onshore winds can also be reduced by about 20–30 km. There is also strong seasonal dependence of the sea breeze. In the study area, sea breezes emerge in June with a spatial extent out to 30–40 km offshore, and affect the most extensive areas in July with extent out to 30–50 km offshore. The affected offshore distance decreases to about 30 km in August and further to about 10 km in September.

Mountain can affect surface winds through both thermodynamic and mechanical mechanism. The impacts vary from month to month. During the cold months, drainage flow starts to build up at the mountain top in September, and gradually increases the intensity and extent downward to the slope as the surface temperatures continue to decrease. During the coldest months of the year in the area from November to February, the strongest drainage flow can occupy the entire slope; however, the flow can rarely go downward below about 300 meters due to the extremely strong inversion. During summer, diurnal variation of surface winds is dominated by the development of mountain-plains solenoidal circulation. The upslope winds near surface start to build up around 0900 local time, reaching the strongest strength around 1500 local time, and continuing until 2100 local time. The returning flow of MPS circulation is located about 1 km above the top of mountain. The mountain barrier effect plays roles over the north slope of Chukotka Mountains and the south slope of eastern Brooks Range from October to March, turning and enhancing the approaching flow and resulting in low level wind maximum over the slope.

Sea breezes and mountain barrier effect are also subject to variation and changes in response to adjustment of large-scale atmosphere circulation in our study domain. Out analysis shows that sea breeze along the western Beaufort Sea coast is negatively correlated with storm activity in July, implying that strong storm activity can inhibit the development of sea breezes, possibly due to clouds and strong winds associated with storms resulting decreased temperature over land and reduced stability of atmosphere. In winter, the intense and location of the Beaufort High play roles in determining the intense of mountain barrier effect by altering the approaching flow towards mountains.

CHAPTER 5

Conclusion and Discussion

Surface wind is a crucial parameter for assessing and predicting oil spill transport and dilution of air pollution. In the Chukchi-Beaufort Sea region along the northern Alaskan coast, the significant environmental changes in recent decades raise uncertainty on our understanding of temporal and spatial structure of surface wind. In this dissertation, a series of efforts are made step by step to improve representation of mesoscale wind climatology in the Chukchi-Beaufort Seas and Arctic Slope. High resolution regional reanalysis are first generated by optimizing WRF and WRFDA modeling system through a series of sensitivity experiments. The reanalysis data are then thoroughly analyzed in order to understand the characters of surface wind.

The WRF model and its variational data assimilation system WRFDA were applied to the study area to generate the long-term Chukchi-Beaufort High-Resolution Atmospheric Reanalysis (CBHAR). Following Zhang et al.'s (2013) previous work on optimizing the configuration of physical parameterizations, an optimized WRFDA was configured through a set of assimilation sensitivity experiments. The sensitivity of WRFDA to model background errors and the assimilation of various observational datasets were analyzed. In total, three BEs are evaluated, including the built-in global BE, and two customized BE estimated based on one year simulation of 2009 and one month simulation in July 2009, separately. The results suggest that the usage of the built-in global BE should be avoided in this study, for the significantly degraded simulations in both winter and summer, very likely due to its presumably inaccurate representation of errors for the regional model. The customized model BEs serve to improve the 10-m wind and 2-m temperature in coastal areas. The assimilated observations may also play roles differently. Therefore, several sources of observation are evaluated separately to investigate the possible

impacts. It is found that assimilating in situ surface observations and radiosonde measurements produces significant improvements for surface variables and upper-air variables. The simulation of sea-surface winds can be significantly improved by assimilating QuikSCAT data, which provide distinctive data coverage over open water. The evaluation on MODIS retrievals reveals that the profiles have to be carefully selected to be assimilated. The use of the entire dataset may make most examined variables worse. The assimilation of COSMIC profiles doesn't produce negative impact for both surface and upper-air variables. Synthesizing the results of optimizing the configuration of physical parameterizations (Zhang et al. 2013) and optimizing WRFDA, experiment reanalysis confirms that consistent improvements are achieved in the finalized model configuration that serves to generate CBHAR.

The surface wind climate is determined by both prevailing synoptic weather patterns and prominent underlying geographic features. The 10-km resolution reanalysis data CBHAR, covering the period from 1979 to 2009, enable the further study on surface winds caused by mesoscale processes related to local geography. The climatology of sea breezes, up/downslope winds and mountain barrier effect are thus studied.

In the study domain, sea breezes are most active in June, July and August and are less identifiable in the other months. The strongest onshore winds are developed at around 1500 local time with maximum onshore wind speed of ~2 m s^{-1} at the coastline. The returning flow is located at about 1km above ground. Terrains near the shoreline play important roles in affecting sea breeze circulation by enhancing the upward motion and moving the center of strong onshore winds and the entire circulation toward the slope. There is also strong seasonal dependence of the sea breeze. In the study area, sea breezes emerge in June with a spatial extent out to 30–40 km offshore, and affect the most extensive areas in July with extent out to 30–50 km offshore. The

affected offshore distance decreases to about 30 km in August and further to about 10 km in September.

Up/downslope winds are caused by thermodynamic processes of terrains. The density currents caused by adiabatic cooling are identified from September to April. In January, the strongest drainage flow can reach speed of 2 m s^{-1}. One significant feature of drainage flow in the study domain is that the downward motion is blocked by strong inversion in lower atmosphere; the downslope winds are thus restrained in the area above 300 meters. In summer, upslope winds are dominating surface winds over mountain slope. Mountain can also affect surface winds through mechanical mechanism. The mountain barrier effect plays roles over the north slope of Chukotka Mountains and the south slope of eastern Brooks Range from October to March, turning and enhancing the approaching flow and resulting in low level wind maximum over the slope.

Sea breezes and mountain barrier effect are also affected by the adjustment of large-scale atmosphere circulation in our study domain. In July, strong storm activity can inhibit the development of sea breezes, possibly due to clouds and strong winds associated with storms resulting decreased temperature over land and reduced stability of atmosphere. In winter, the intense and location of the Beaufort High play roles in determining the intense of mountain barrier effect by altering the approaching flow towards mountains.

References

Anthes, R. A., C. Rocken, and Y. Kuo, 2000: Applications of COSMIC to meteorology and climate. TAO, 11(1), 115-156.

Anthes, R. A., P. A. Bernhardt, Y. Chen, L. Cucurull, K. F. Dymond, D. Ector, S. B. Healy and Coauthors, 2008: The COSMIC/FORMOSAT-3 mission: Early results. B. Am. Meteor. Soc., 89, 313–333.

Antonelli, M., and R. Rotunno, 2007: Large-eddy simulation of the onset of the sea breeze. Journal of the Atmospheric Sciences, 64(12), 4445-4457.

Banta, R. M., 1990: The role of mountain flows in making clouds. Atmospheric Processes over Complex Terrain, Meteor. Monogr. 23, 45, 229-283.

Barker, D. M., W. Huang, Y-R. Guo, A. J. Bourgeois, and Q. N. Xiao, 2004: A three-dimensional variational data assimilation system for MM5: Implementation and initial results. Mon. Wea. Rev., 132, 897–914.

Barker, D. M. and Coauthors, 2012: The Weather Research and Forecasting Model's Community Variational/Ensemble Data Assimilation System: WRFDA. Bull. Amer. Meteor. Soc., 93, 831–843.

Bell, G. D. and L. F. Bosart, 1988: Appalachian cold-air damming. Mon. Wea. Rev., 116, 137-161.

Bromwich, D. H., 1989: An extraordinary katabatic wind regime at Terra Nova Bay, Antarctica. Mon. Wea. Rev., 117, 688–695.

Bromwich, D. H., K. M. Hines, and L.-S. Bai, 2009: Development and testing of Polar Weather Research and Forecasting model: 2. Arctic Ocean. *J. Geophys. Res.,* **114,** D08122, doi: 10.1029/2008JD010300.

Bromwich, D. H. and Coauthors, 2010: Arctic System Reanalysis: Call for community involvement. *Eos Trans. AGU,* ***91(2),*** 13–14, doi:10.1029/2010EO020001.

Bromwich, D. H., F. O. Otieno, K. M. Hines, K. W. Manning, and E. Shilo, 2013: Comprehensive evaluation of Polar Weather Research and Forecasting model performance in the Antarctic. *J. Geophys. Res*, **118**, 274–292.

Cassano, J. J., M. E. Higgins, and M. W. Seefeldt, 2011: Performance of the Weather Research and Forecasting (WRF) Model for month-long pan-Arctic simulations. *Mon. Wea. Rev.,* **139,** 3469–3488.

Chen, F. and J. Dudhia, 2001: Coupling an advanced land surface-hydrology model with the Penn State-NCAR MM5 modeling system. Part I: Model implementation and sensitivity. *Mon. Wea. Rev.,* **129,** 569–585.

Clark, T. L. and W. R. Peltier, 1984: Critical level reflection and the resonant growth of nonlinear mountain waves. *J. Atmos. Sci.*, **41**, 3122-3134.

Collins, W. D. et al., 2004: Description of the NCAR Community Atmosphere Model (CAM3.0). NCAR Technical Note, NCAR/TN-464+STR, 226 pp.

Comiso, J. 1999, updated 2012. Bootstrap Sea Ice Concentrations from Nimbus-7 SMMR and DMSP SSM/I-SSMIS. Boulder, Colorado USA: National Snow and Ice Data Center. Digital media.

Comiso, J. C., C. L. Parkinson, R. Gersten, and L. Stock, 2008: Accelerated decline in the Arctic sea ice cover. *Geophys. Res. Lett.,* **35,** L01703.

Crosby, D. S., L. C. Breaker, and W. H. Gemmill, 1993: A proposed definition for vector correlation in geophysics: theory and application. *J. Atmos. Oceanic Technol.*, **10**, 355-367.

Cucurull, L. and J. C. Derber, 2008: Operational implementation of COSMIC observations into NCEP's Global Data Assimilation System. *Weather and Forecasting*, **23(4)**, 702–711.

Dailey, P. S. and R. G. Fovell, 1999: Numerical simulation of the interaction between the sea-breeze front and horizontal convective rolls. Part I: Offshore ambient flow. *Mon. Wea. Rev.*, **127**, 858-878.

Dee, D. P. and Coauthors, 2011: The ERA-Interim reanalysis: configuration and performance of the data assimilation system. *Q. J. R. Meteor. Soc.,* **137,** 553–597.

Dickey, W. W., 1961: A study of a topographic effect on wind in the Arctic. *J. Atmos. Sci.*, **18,** 790–803.

Doney, S. C. and Coauthors, 2012: Climate change impacts on marine ecosystems. *Marine Science,* 4.

Fan, X. and J. S. Tilley, 2005: Dynamic assimilation of MODIS-retrieved humidity profiles within a regional model for high-latitude forecast applications. *Mon. Wea. Rev.*, **133(12)**, 3450–3480.

Ford, J. D. and T. Pearce, 2010: What we know, do not know, and need to know about climate change vulnerability in the western Canadian Arctic: A systematic literature review. *Environmental Res. Lett.,* **5(1),** 014008.

Grell, G. A. and D. Devenyi, 2002: A generalized approach to parameterizing convection combining ensemble and data assimilation techniques. *Geophys. Res. Lett.*, **29**, 1693, doi: 10.1029/2002GL015311.

Gundlach, E. R. and M. O. Hayes, 1978: Vulnerability of coastal environments to oil spill impacts. *Mar. Technol. Soc. J.*, **12**(4), 18–27.

Hines, K. M. and D. H. Bromwich, 2008: Development and testing of Polar Weather Research and Forecasting (WRF) Model. Part I: Greenland ice sheet meteorology. *Mon. Wea. Rev.*, **136**, 1971–1989.

Hines, K. M., D. H. Bromwich, L.-S. Bai, M. Barlage, and A. G. Slater, 2011: Development and testing of Polar WRF. Part III: Arctic land. *J. Climate*, **24**, 26–48.

Hong, S.-Y. and J.-O. J. Lim, 2006: The WRF Single-Moment 6-Class Microphysics Scheme (WSM6). *J. Korean Meteor. Soc.*, **42**, 129–151.

Hong, S.-Y., Y. Noh, and J. Dudhia, 2006: A new vertical diffusion package with an explicit treatment of entrainment processes. *Mon. Wea. Rev.*, **134,** 2318–2341.

Huang, C.-Y., Y.-H. Kuo, S.-H. Chen, and F. Vandenberghe, 2005: Improvements in typhoon forecasts with assimilated GPS occultation refractivity. *Weather and Forecasting*, **20(6)**, 931–953.

Huang, X. and Coauthors, 2009: Four-dimensional variational data assimilation for WRF: Formulation and preliminary results. *Mon. Wea. Rev.*, **137**, 299–314.

Iacono, M., J. Delamere, E. Mlawer, M. Shephard, S. Clough, and W. Collins, 2008: Radiative forcing by long-lived greenhouse gases: Calculations with the AER radiative transfer models. *J. Geophys. Res*, **113,** D13103.

Janjic, Z. I., 1994: The step-mountain Eta coordinate model: Further developments of the convection, viscous sublayer and turbulence closure schemes. *Mon. Wea. Rev.,* **122,** 927–945.

Janjic, Z. I., 1996: The Mellor-Yamada level 2.5 scheme in the NCEP Eta Model. *11th Conference on Numerical Weather Prediction*, Norfolk, VA, *Amer. Meteor.Soc.,* 333–334.

Janjic, Z. I., 2002: Nonsingular implementation of the Mellor–Yamada Level 2.5 Scheme in the NCEP Meso model. *NCEP Office Note,* No. 437, National Centers for Environmental Prediction, 61 pp.

Kain, J. S., 2004: The Kain-Fritsch convective parameterization: An update. *J. Appl. Meteoro.*, **43,** 170–181.

Kalnay, E. et al., 1996: The NCEP/NCAR 40-Year Reanalysis Project. *Bull. Amer. Meteor. Soc.*, **77**, 437–471.

Key, J. R., D. Santek, C. S. Velden, N. Bormann, J.-N. Thépaut, L. P. Riishojgaard, Y. Zhu, and W. P. Menzel, 2003: Cloud-drift and water vapor winds in the polar regions from MODIS. *IEEE Trans, Geosci. Remote Sens.*, **41**, 482–492.

King, M. D., W. P. Menzel, Y. J. Kaufman, D. Tanré, B. Gao, S. Platnick, S. A. Ackerman, L. A. Remer, R. Pincus, and P. A. Hubanks, 2003: Cloud and aerosol properties, percipitable water, and profiles of temperature and water vapor from MODIS. *Geoscience and Remote Sensing, IEEE Transactions on 41*, **2**, 442-458.

Kozo, T., 1979: Evidence for sea breezes on the Alaskan Beaufort Sea coast. *Geophys. Res. Lett.,* **6,** 849–852.

Kozo, T., 1980: Mountain barrier baroclinity effects on surface winds along the Alaskan coast. *Geophys. Res. Lett.,* **7,** 377–380.

Lin, Y.-L., 2007: Mesoscale Dynamics. Cambridge University Press, 630pp.

Liu, H., P. Q. Olsson, and K. Volz, 2008: SAR observation and modeling of gap winds in the Prince William Sound of Alaska. *Sensors*, **8(8)**, 4894–4914.

Liu, Z.-Q. and F. Rabier, 2002: The interaction between model resolution, observation resolution and observation density in data assimilation: A one-dimensional study. *Q. J. R. Meteor. Soc.*, **128,** 1367–1386.

Liu F., J. R. Krieger, and J. Zhang, 2013: Toward producing the Chukchi-Beaufort High-Resolution Atmospheric Reanalysis (CBHAR) via the WRFDA data assimilation system. *Mon. Wea. Rev.*, accepted.

Long DG, Mendel JM (1990) Model-based estimation of wind fields over the ocean from wind scatterometer measurements. I. Development of the wind field model. *IEEE Trans Geosci Remote Sens,* **28(3)**, 349–360.

Lynch, A. H., A. G. Slater, and M. Serreze, 2001: The Alaskan Arctic frontal zone: Forcing by orography, coastal contrast, and the boreal forest. *J. Climate*, **14(23),** 4351–4362.

Lynch, A. H., J. A. Curry, R. D. Brunner, and J. A. Maslanik, 2004: Toward an integrated assessment of the impacts of extreme winds events on Barrow, Alaska. *Bull. Amer. Meteor. Soc*., **85**, 209–221.

Lyons, W. A. and L. E. Olsson, 1972: The climatology and prediction of the Chicago lake breeze. *J. Appl. Meteor.*, **11**. 1254-1272.

Mellor, G. L. and T. Yamada, 1982: Development of a turbulence closure model for geophysical fluid problems. *Rev. Geophys. Space Phys.*, **20**, 851–875.

Mesinger, F. et al., 2006: North American Regional Reanalysis. *Bull. Amer. Meteor. Soc.*, **87**, 343–360.

Moore, G. W. K., 2012: Decadal variability and a recent amplification of the summer Beaufort Sea High. *Geophys. Res. Lett.,* **39,** L10807.

Moore, G. W. K. and R. S. Pickart, 2012: Northern Bering Sea tip jets. *Geophys. Res. Lett.,* **39,** L08807.

Morrison, H. C., G. Thompson, and V. Tatarskii, 2009: Impact of cloud microphysics on the development of trailing stratiform precipitation in a simulated squall line: Comparison of one- and two-moment schemes. *Mon. Wea. Rev.,* **137,** 991–1007.

Mölders, N., 2008: Suitability of the Weather Research and Forecasting (WRF) model to predict the June 2005 fire weather for Interior Alaska. *Weather Forecast.* **23,** 953–973.

Olsson, P. Q. and J. Y. Harrington, 2000: Dynamics and energetics of the cloudy boundary layer in simulations of off-ice flow in the marginal ice zone. *J. Geophys. Res.,* **105**, 11.

Onogi, K. et al., 2007: The JRA-25 Reanalysis. *J. Meteor. Soc. Japan*, **85**, 369–432.

Overland, J. E., 2009: Meteorology of the Beaufort Sea. *J. Geophys. Res*., **114**, C00A07.

Orville, H. D., 1964: On mountain upslope winds. *J.Atmos. Sci.*, **21**, 622-33.

Orville, H. D., 1968: Ambient wind effects on the initiation and development of cumulus clouds over mountains. *J. Atmos. Sci.*, **25**, 385-403.

Parish, T. R. and D. H. Bromwich, 1987: The surface windfield over the Antarctic ice sheets. *Nature*, **328**, 51–54.

Parish, T. R. and D. H. Bromwich, 1991: Continental-scale simulation of the Antarctic katabatic wind regime. *J. Climate*, **4**, 135–146.

Parish, T. R. and J. J. Cassano, 2003: The role of katabatic winds on the Antarctic surface wind regime. *Mon. Wea. Rev.*, **131**, 317–333.

Parrish, D. and J. Derber, 1992: The National Meteorological Center's spectral statistical-interpolation analysis system. *Mon. Wea. Rev.,* **120,** 1747–1763.

Picou, J. S. and Coauthors, 2009: Community impacts of the Exxon Valdez oil spill: A synthesis and elaboration of social science research. *Synthesis: Three Decades of Research on Socioeconmic Effects Related to Offshore Petroleum Development in Coastal Alaska,* S. R. Braund and J. Kruse, eds. Anchorage, Alaska: Steven R. Braund & Associates, 279–310.

Porter, D. F., J. J. Cassano, and M. C. Serreze, 2011: Analysis of the Arctic atmospheric energy budget in WRF: A comparison with reanalyses and satellite observations. *J. Geophys. Res.,* **116,** D22108.

Powers, J. G., 2007: Numerical Prediction of an Antarctic Severe Wind Event with the Weather Research and Forecasting (WRF) Model. *Mon. Wea. Rev.*, **135**, 3134–3157, doi: http://dx.doi.org/10.1175/MWR3459.1

Pu. Z., W.-K. Tao, S. Braun, J. Simpson, Y. Jia, J. Halverson, W. Olson, and A. Hou, 2002: The impact of TRMM data on mesoscale numerical simulation of supertyphoon Paka. *Mon. Wea. Rev.*, **130(10)**, 2448–2458.

Raymond, D. J., 1972: Calculation of airflow over an arbitrary ridge including diabatic heating and cooling. *J. Atmos. Sci.*, **29**, 837-843.

Reed, M., O. and Coauthors, 1999: Oil spill modeling towards the close of the 20th century: Overview of the state of the art. *Spill Science and Technology Bulletin*, **5(1),** 3–16.

Schwerdtfeger, W., 1974: Mountain barrier effect on the flow of stable air north of the Brooks Range. In Proc. 24th Alaskan Science Conf, 204–208.

Shulski, M. and G. Wendler, 2007: *Climate of Alaska*. University of Alaska Press, 216 pp.

Singh, R., C. M. Kishtawal, S. P. Ojha, and P. K. Pal, 2012: Impact of assimilation of Atmospheric InfraRed Sounder (AIRS) radiances and retrievals in the WRF 3D-Var assimilation system. *J. Geophys. Res.,* **117,** D11.

Skamarock, W. C. and Coauthors, 2008: A Description of the Advanced Research WRF Version 3. NCAR Tech Note, NCAR/TN–475+STR, 113 pp.

Smith, R. B., 1985: On severe downslope winds. *J. Atmos. Sci.*, **42**, 2597-2603.

Smith, R. B., and Y.-L. Lin, 1982: The addition of heat to stratified airstream with application to the dynamics of orographic rain. *Quart. J. Roy. Meteor. Soc.*, **108**, 353-378.

Stegall, S. T. and J. Zhang, 2012: Wind field climatology, changes, and extremes in the Chukchi–Beaufort Seas and Alaska North Slope during 1979–2009. *J. Climate,* **25,** 8075–8089.

Stroeve, J., M. M. Holland, W. Meier, T. Scambos, and M. Serreze, 2007: Arctic sea ice decline: Faster than forecast. *Geophys. Res. Lett.,* **34,** L09501.

Webler, T. and F. Lord, 2010: Planning for the human dimensions of oil spills and spill response. *Environmental Management,* **45,** 723–738.

Thorpe, A. J. , M. J. Miller, and M. W. Moncrieff, 1980: Dynamical models of two-dimensional downdraughts. *Quart. J. Roy. Meteor. Soc.*, **106**, 463-484.

Tijm ABC, Van Delden AJ, Holtslag AAM, 1999: The inland penetration of sea breezes. *Contrib Atmos Phys*., **72**, 317-328.

Tripoli, G. J., and W. R. Cotton, 1989: Numerical study of an observed mesoscale convective system. Part I: Simulated genesis and comparison with observations. *Mon. Wea. Rev.*, **117**, 273-304.

Uppala, S. M. et al., 2005: The ERA-40 re-analysis. *Q. J. R. Meteorol. Soc.*, **131**, 2961– 3012.

Webler, T. and F. Lord, 2010: Planning for the human dimensions of oil spills and spill response. *Environ. Manage.*, **45**, 723–738.

Wilson, A. B., D. H. Bromwich, and K. M. Hines, 2011: Evaluation of Polar WRF forecasts on the Arctic System Reanalysis domain: Surface and upper air analysis. *J. Geophys. Res.,* **116,** D11112.

Wilson, A. B., D. H. Bromwich, and K. M. Hines, 2012: Evaluation of Polar WRF forecasts on the Arctic System Reanalysis domain: 2. Atmospheric hydrologic cycle. *J. Geophys. Res.*, **117**, D04107.

Wolyn, P. G. and T. B. McKee, 1994: The mountain-plains circulation east of a 2-km-high north-south barrier. *Mon. Wea. Rev.*, **112**, 1490-14508.

Xavier, A.C., B.F.T. Rudroff, L.M.S. Berka, M.A. Moreira, 2006: Multi-temporal analysis of MODIS data to classify sugarcane crop. *Int. J. of Remote. Sens.*, **27(4)**, 755-768.

Xu, Q., S. Gao, and B. H. Fiedler, 1996: A therotical study of cold air damming with upstream cold air flow. *J. Atmos. Sci.*, **53**, 312-326.

You, J., M. Shulski, and K. G. Hubbard, 2011: Quality control of high intensity climate data in Alaska. *Amer. Geophys. Union*, Fall Meeting 2011, abstract #A33A-0173.

Zhang, X. and J. Zhang, 2001: Heat and freshwater budgets and pathways in the Arctic Mediterranean in a coupled ocean/sea-ice model. *J. Oceanogr.*, **57**, 207–237.

Zhang, X., J. E. Walsh, J. Zhang, U. S. Bhatt, and M. Ikeda, 2004: Climatology and interannual variability of arctic cyclone activity: 1948–2002. *J. Climate*, **17**, 2300–2317.

Zhang, X., Q. Xiao, and P. J. Fitzpatrick, 2007: The impact of multisatellite data on the initialization and simulation of Hurricane Lili's (2002) rapid weakening phase. *Mon. Wea. Rev.*, **135**(2), 526–548.

Zhang, X. and Coauthors, 2013: Final project report for the Beaufort and Chukchi Seas Mesoscale Meteorology Modeling Study. Bureau of Ocean Energy Management, BOEM 2013-0119.

Appendix

I. Idealized Simulation of Sea Breezes

1. Improved Idealized Model

The simulation of sea breezes is conducted with an improved idealized numerical model through a series of sensitivity experiments for better understanding the characters of sea breezes at high latitude. The idealized numerical model is based on Weather Research and Forecasting Model (WRF) version 3.2, which has a 2-dimensional idealized sea breeze package. The package enables us to conduct idealized case study using full-physics, including longwave and shortwave radiation, land surface model, and planetary boundary layer scheme that are supported by WRF3.2. However, some limitations of the package prohibit our further application for the study; for example, the surface skin temperature can increase over 5 degrees in simulation of 2 weeks, the surface pressure drops to 800 mb in several days of simulation. Thus, the source codes of WRF3.2 have to be modified to satisfy our requirement.

The numerical model starts from initialization, which defines the domain, the physical configurations, and runtime parameters. Basically, all of the improvements are focused on this stage. The latitude, determining the solar radiation, is modified directly in the code, while the Coriolis parameters could be determined by the latitude or directly modified in order to test the effects of Coriolis force solely. The surface temperature, humidity, land-use type, soil parameters, and vegetation category are based on the observed values in our research area.

The model uses periodic lateral boundary condition, which could introduce unrealistic results from the other side of domain (Figure A.1), due to the limited domain size. However, switching to open boundary condition causes other problem; the surface pressure drops sharply from about 1000mb to 800mb in a week. Thus, several damping terms are required to keep the

model variables stable for the open boundary condition we used, in order to conduct relatively long-term (~15 days) simulation which is expected to eliminate the influence of initialization and let the model develops its own circulations driven by thermal contrast. The damping terms will damp the surface pressure (Equation 1), surface temperature (Equation 4) to their initial values, in order to satisfy the constraint of the mass continuity and the conservation of energy. Also, the wind speed perturbation will be damped to 0 m s^{-1} near the lateral boundary (Equation 2,3) since we assume it's far away from the coastal area and would be controlled by other weather system rather than sea breezes.

$$\frac{\partial \mu}{\partial t} = -\frac{\partial(\mu u)}{\partial x} - \frac{\partial(\mu v)}{\partial y} - \frac{\partial(\mu \dot{\eta})}{\partial \eta} + K_R(\mu_0 - \mu) \quad (1)$$

$$\frac{\partial(\mu u)}{\partial t} = \bullet\bullet\bullet + W \cdot K_B \mu(u_0 - u) \quad (3)$$

$$\frac{\partial(\mu v)}{\partial t} = \bullet\bullet\bullet + W \cdot K_B \mu(v_0 - v) \quad (3)$$

$$\frac{\partial(\mu \theta)}{\partial t} = \bullet\bullet\bullet + K_R \mu(\theta_0 - \theta) \quad (4)$$

$$\mu = P_{surface} - P_{top} \quad (5)$$

In addition, special care should be taken on the land surface model, where soil moisture and soil temperature should keep stable. In the model, since no prescriptive lower boundary condition presents to provide soil moisture information, the soil tends to get drier and drier, causing the surface skin temperature increases by over 5 degrees in two weeks (Figure A.2). In order to eliminate this effect and keep the model stable, the soil moisture is set as constant value at any given soil layers according the climatology soil moisture along the Northern Coast of

Alaska. The results are improved significantly with more stable surface skin temperature (Figure A.2).

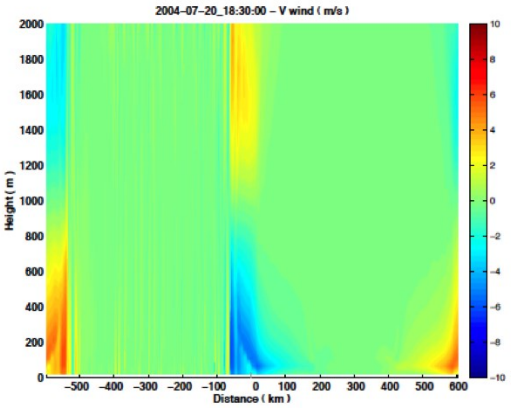

Figure A.1. The vertical profile of offshore wind component across the domain when using periodic lateral boundary condition. The negative values represent air flow from right to left, and positive values from left to right.

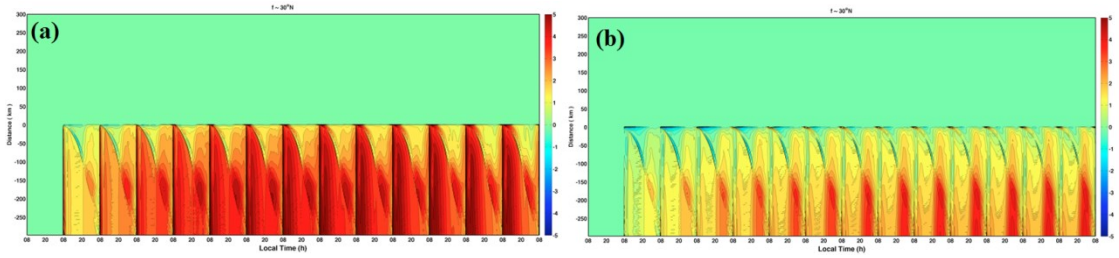

Figure A.2. The abnormally surface skin temperature against the values on the first day when using variable soil moisture (a) and fixed soil moisture (b).

The Coriolis parameter, which should be controlled by the latitude, is fixed as zero in the WRF model. In our study, we are interested at how greater Coriolis force in the area can affect the inland penetration of sea breezes. Thus, the impact of latitude has to be included. In addition,

in the model, the solar radiation is also controlled by latitude, which allows us to investigate the impact of polar day on the sea breeze circulation.

2. Impacts of the Coriolis force

The aforementioned improvements of the WRF3.2 idealized modeling system enable us to conduct a series of experiments, in order to quantitatively understand the impact of Coriolis force. The model's domain was configured to cover horizontal range of 1200 km by 600 grids with grid spacing of 2 km. The coastline was located at the center of domain. The domain has 46 vertical levels with the top at 25 mb. The model physics included CAM longwave and shortwave radiation, MM5 similarity surface layer, Noah land surface model and Yonsei University boundary layer.

The Coriolis force mainly affects the latter stages of sea breezes lifecycle (Tijm et al. 1999; Antonelli and Rotunno 2007), introducing the sea breezes rotate into a plane parallel to the coast. With the diurnal heating 30° latitude poleward, the Coriolis force can reduce the inland penetration of sea breezes. At high latitude, Coriolis force might be responsible for the occurrence of land breezes, rather than the reversing pressure gradient. In our domain, the data analysis shows that the land breezes can be rarely developed during night. The reason needs to be further investigated.

Four experiments were designed to study how the Coriolis force affects sea breezes. In the experiments, the Coriolis parameters are given by $F = 2*\Omega*\sin(\Phi)$, where Ω is the angular velocity of earth rotation, and Φ is the latitude. The values of Coriolis force are set to be equivalent as at 0°, 30°N, 45°N, and 70°N, separately. The other configurations are kept same. The surface skin temperature was set to be 285 K over land, and 275 K over ocean, based on the observations along the Beaufort Sea coast in July. The background winds were initialized as zero

from surface to top of the domain. The vertical temperature profile was provided as initial temperature distribution based on climatology at Barrow in July, as shown in Figure A.3. At the lower layer of atmosphere, an inversion was introduced below about 200 meters where temperature is warmer than surface by about 7.5 K. The incoming solar radiation was set to be equivalent to be at 70°N in July.

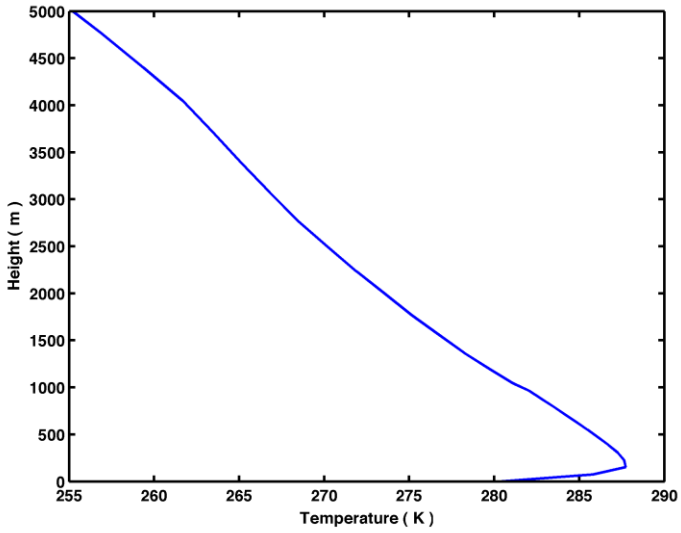

Figure A.3. The initial temperature profile.

The comparisons between the idealized simulations (Figure A.4) show a significant decrease in the extent of the sea breeze inland penetration as the Coriolis force increases. When the Coriolis is zero, the sea breeze tends to push toward inland by about 20 km per hour. The process lasts to the early morning on the next day, resulting more than 250 km horizontal penetration of sea breeze. At the coastline, sea breezes are most active from noon to late afternoon. The horizontal extent of sea breezes significantly reduces when the Coriolis force increases. In the other three experiments when the Coriolis force increases to be equivalent with latitude 30°N, 45°N and 70°N, the final distances of penetration are about 140 km, 110 km, and

80 km, separately. According to the diurnal variation of surface winds (Figure A.4), the onshore winds are turned to right as the air flows toward inland. In the evening, the air flow is turned completely to be parallel with the coastline, which terminates the process of inland penetration. As the Coriolis force increases, the air flow is turned more effectively, resulting less extents of sea breezes.

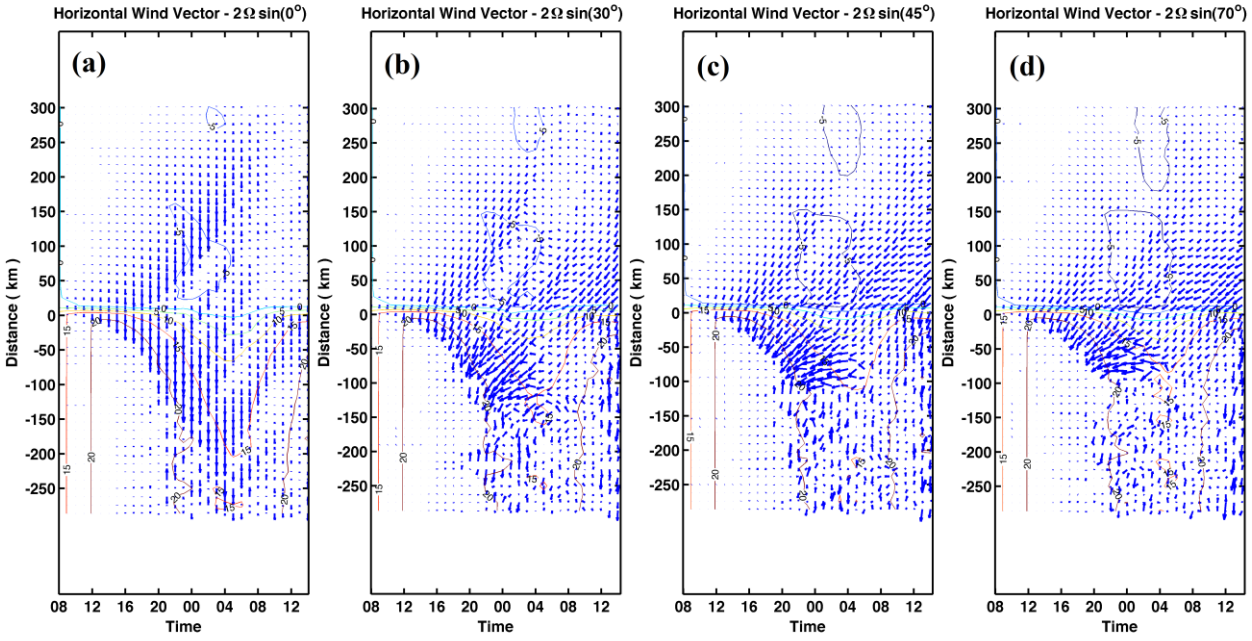

Figure A.4. The diurnal variation of surface wind vectors when the Coriolis force was set to be equivalent with latitude 0° (a), 30°N (b), 45°N (c), 70°N (d). The coastline is located at distance 0, while negative distance represents land and positive distance represents ocean.

Along the coastline, the Coriolis force tends to introduce a constant alongshore wind component. This is very likely due to the continuous incoming solar radiation, resulting warmer land surface in a daily cycle and therefore continuous sea breezes. The onshore winds are turned to right by the Coriolis force and to be parallel to the shoreline. At high latitude of 70°N, the alongshore wind are even stronger than onshore wind.